



# VCU

Virginia Commonwealth University  
VCU Scholars Compass

---

Theses and Dissertations

Graduate School


---

2019

## Mechanochemical Regulation of Epithelial Tissue Remodeling: A Multiscale Computational Model of the Epithelial-Mesenchymal Transition Program

Lewis Scott  
*Virginia Commonwealth University*

Follow this and additional works at: <https://scholarscompass.vcu.edu/etd>

 Part of the [Biomechanics and Biotransport Commons](#), [Computational Engineering Commons](#), and the [Molecular, Cellular, and Tissue Engineering Commons](#)

© Lewis E. Scott

---

Downloaded from

<https://scholarscompass.vcu.edu/etd/6032>

This Dissertation is brought to you for free and open access by the Graduate School at VCU Scholars Compass. It has been accepted for inclusion in Theses and Dissertations by an authorized administrator of VCU Scholars Compass. For more information, please contact [libcompass@vcu.edu](mailto:libcompass@vcu.edu).

**Mechanochemical Regulation of Epithelial Tissue  
Remodeling: A Multiscale Computational Model of  
the Epithelial-Mesenchymal Transition Program**

A dissertation presented

by

Lewis E. Scott

to

The Department of Biomedical Engineering

in partial fulfillment of the requirements

for the degree of

Doctor of Philosophy

in the subject of

Computational Biology

Virginia Commonwealth University

Richmond, Virginia

August 2019

© 2019 — Lewis E. Scott

All rights reserved.

Dissertation Advisors: Christopher A. Lemmon, Ph.D. & Seth H. Weinberg, Ph.D.  
Lewis E. Scott

## **Mechanochemical Regulation of Epithelial Tissue Remodeling: A Multiscale Computational Model of the Epithelial-Mesenchymal Transition Program**

### **Abstract**

Epithelial-mesenchymal transition (EMT) regulates the cellular processes of migration, growth, and proliferation - as well as the collective cellular process of tissue remodeling - in response to mechanical and chemical stimuli in the cellular microenvironment. Cells of the epithelium form cell-cell junctions with adjacent cells to function as a barrier between the body and its environment. By distributing localized stress throughout the tissue, this mechanical coupling between cells maintains tensional homeostasis in epithelial tissue structures and provides positional information for regulating cellular processes. Whereas *in vitro* and *in vivo* models fail to capture the complex interconnectedness of EMT-associated signaling networks, previous computational models have succinctly reproduced components of the EMT program. In this work, we have developed a computational framework to evaluate the mechanochemical signaling dynamics of EMT at the molecular, cellular, and tissue scale. First, we established a model of cell-matrix and cell-cell feedback for predicting mechanical force distributions within an epithelial monolayer. These findings suggest that tensional homeostasis is the result of cytoskeletal stress distribution across cell-cell junctions, which organizes otherwise migratory cells into a stable epithelial monolayer. However, differences in phenotype-specific cell characteristics led to discrepancies in the experimental and computational observations. To better understand the role of mechanical cell-cell feedback in regulating EMT-dependent cellular processes, we introduce an EMT gene regulatory network of key epithelial and mesenchymal markers, E-cadherin and N-cadherin, coupled to a mechanically-sensitive intracellular signaling cascade. Together these signaling networks integrate mechanical cell-cell feedback with EMT-associated gene regulation. Using this approach, we demonstrate that the phenotype-specific properties collectively account for discrepancies in the computational and experimental observations. Additionally, mechanical cell-cell feedback suppresses the EMT program, which is reflected in the gene expression of the heterogeneous cell population. Together, these findings advance our understanding of the complex interplay in cell-cell and cell-matrix feedback during EMT of both normal physiological processes as well as disease progression.

# Contents

|   |             |
|---|-------------|
| <b>Abstract</b>   | <b>iii</b>  |
| <b>List of Figures</b>  | <b>viii</b> |
| <b>List of Tables</b>   | <b>x</b>    |
| <b>Glossary</b>   | <b>xi</b>   |
| <b>Dedication</b>   | <b>xii</b>  |
| <b>1 Introduction</b>   | <b>1</b>    |
| <b>2 Literature Review</b>  | <b>3</b>    |
| 2.1 Introduction . . . . .  | 3           |
| 2.2 Epithelial-mesenchymal transition . . . . .                                       | 5           |
| 2.2.1 Epithelium . . . . .  | 5           |
| 2.2.2 Mesenchyme . . . . .  | 7           |
| 2.3 Mechanochemical signaling networks in epithelial-mesenchymal transition . . . . . | 9           |
| 2.3.1 Molecular signaling cascades . . . . .  | 9           |
| 2.3.2 EMT-associated gene regulatory network . . . . .                                | 11          |
| 2.3.3 Mechanotransduction . . . . .   | 12          |
| 2.3.4 Cell-matrix and cell-cell adhesion . . . . .                                    | 12          |
| 2.3.5 Mechanotransduction of cell-cell junctions . . . . .                            | 13          |

## CONTENTS

|          |   |           |
|----------|---|-----------|
| 2.3.6    | Mechanotransduction in disease . . . . .  | 14        |
| 2.4      | Cell-matrix mechanochemical feedback . . . . .                                      | 15        |
| 2.4.1    | Basal lamina and epithelial-mesenchymal transition . . . . .                        | 15        |
| 2.4.2    | Fibrous matrix and epithelial-mesenchymal transition . . . . .                      | 17        |
| 2.4.3    | Connective tissue and growth factor tethering. . . . .                              | 18        |
| 2.4.4    | Tissue remodeling and epithelial-mesenchymal transition . . . . .                   | 19        |
| 2.4.5    | Cell-matrix mechanical feedback and epithelial-mesenchymal tran-<br>sition. . . . . | 21        |
| 2.5      | Computational models of molecular, cellular, and tissue scale phenomena .           | 23        |
| 2.5.1    | Cellular Potts model . . . . .  | 23        |
| 2.5.2    | Cellular Potts model and extracellular matrix remodeling . . . . .                  | 24        |
| 2.5.3    | Epithelial-mesenchymal transition gene regulatory network . . . . .                 | 24        |
| 2.5.4    | Mechanotransduction at the adherens junction . . . . .                              | 25        |
| 2.6      | Summary . . . . .   | 26        |
| <b>3</b> | <b>Mechanical cell-cell feedback of the epithelial monolayer</b>                    | <b>29</b> |
| 3.1      | Introduction . . . . .  | 29        |
| 3.2      | Methods . . . . .   | 31        |
| 3.2.1    | Cellular Potts model . . . . .  | 31        |
| 3.2.2    | Finite element analysis . . . . .   | 34        |
| 3.2.3    | Traction forces . . . . .   | 35        |
| 3.2.4    | Intercellular tension . . . . .   | 36        |
| 3.2.5    | Cell division . . . . .   | 38        |
| 3.2.6    | Numerical simulations . . . . .   | 39        |
| 3.2.7    | Cells and reagents . . . . .  | 40        |
| 3.2.8    | Microcontact printing . . . . .   | 41        |
| 3.2.9    | Immunofluorescence microscopy . . . . .   | 42        |

## CONTENTS

|          |  |           |
|----------|--|-----------|
| 3.2.10   | Cell area and cell number quantification . . . . .   | 42        |
| 3.2.11   | FRET analysis . . . . .  | 43        |
| 3.2.12   | Statistical analysis . . . . .   | 44        |
| 3.3      | Results . . . . .  | 44        |
| 3.3.1    | Multicellular traction forces drive formation of epithelial monolayers                             | 44        |
| 3.3.2    | Spatiotemporal dynamics of monolayer confluence . . . . .  | 46        |
| 3.3.3    | Altered interfacial energies mimic changes in contact inhibition . . .                             | 48        |
| 3.3.4    | Decreasing contact inhibition increases cell size and decreases cell<br>number . . . . .           | 50        |
| 3.3.5    | Cell-cell junction force maintains mechanical equilibrium of multi-<br>cellular clusters . . . . . | 51        |
| 3.3.6    | Individual cell geometry spatial patterns . . . . .  | 54        |
| <b>4</b> | <b>Gene regulation of the epithelial-mesenchymal program</b>                                       | <b>60</b> |
| 4.1      | Introduction . . . . .   | 60        |
| 4.2      | Methods . . . . .  | 62        |
| 4.2.1    | Gene regulatory Network . . . . .  | 63        |
| 4.2.2    | $\beta$ -catenin signaling . . . . .   | 67        |
| 4.2.3    | Cell-cell binding and unbinding . . . . .  | 70        |
| 4.2.4    | Mechanotransduction . . . . .  | 71        |
| 4.2.5    | Signaling network coupling . . . . .   | 74        |
| 4.2.6    | Phenotype characterization . . . . .   | 75        |
| 4.2.7    | Numerical simulations . . . . .  | 75        |
| 4.3      | Results . . . . .  | 77        |
| 4.3.1    | Rate analysis . . . . .  | 77        |
| 4.3.2    | EMT-associated gene expression . . . . .   | 77        |
| 4.3.3    | $\beta$ -catenin signaling . . . . .   | 80        |
| 4.3.4    | Phenotype properties . . . . .   | 82        |

*CONTENTS*

|                                 |            |
|---------------------------------|------------|
| <b>5 Discussion</b>             | <b>85</b>  |
| <b>6 Supporting Information</b> | <b>95</b>  |
| <b>References</b>               | <b>100</b> |



# List of Figures

|     |  |     |
|-----|--|-----|
| 2.1 | Mechanochemical signaling framework. . . . .             | 27  |
| 2.2 | Multiscale computational framework. . . . .              | 28  |
| 3.1 | Comparison of the single and multicellular FMA. . . . .  | 45  |
| 3.2 | Spatiotemporal dynamics of CPM. . . . .                  | 47  |
| 3.3 | Parameter analysis of interaction energies. . . . .      | 49  |
| 3.4 | Epithelial morphological characterization. . . . .       | 51  |
| 3.5 | Junction force in EMT. . . . .                           | 52  |
| 3.6 | Spatial patterns of cell morphology. . . . .             | 55  |
| 3.7 | One-dimensional junction force model. . . . .            | 57  |
| 4.1 | EMT-GRN schematic. . . . .                               | 64  |
| 4.2 | EMT-GRN bistable switch. . . . .                         | 65  |
| 4.3 | Temporal dynamics of the EMT-GRN. . . . .                | 68  |
| 4.4 | Von Neumann neighborhood of two simulated cells. . . . . | 72  |
| 4.5 | GRN Rate analysis. . . . .                               | 78  |
| 4.6 | GRN time series. . . . .                                 | 79  |
| 4.7 | $\beta$ -catenin signaling dynamics. . . . .             | 81  |
| 4.8 | Phenotype-specific properties. . . . .                   | 83  |
| S1  | Multicellular cluster connectivity. . . . .              | 118 |

*LIST OF FIGURES*

|    |                                    |     |
|----|------------------------------------|-----|
| S2 | Substrate strain heatmaps. . . . . | 119 |
| S3 | Stochastic EMT-GRN. . . . .        | 120 |

# List of Tables

- 4.1 EMT-associated gene regulatory network state variables. . . . . 67
- 4.2  $\beta$ -catenin signaling system parameters. . . . . 70
- 4.3 Phenotype-specific properties of simulated cells. . . . . 76
  
- S1 CPM and FEM parameters. . . . . 121
- S2 EMT-GRN parameters and rates. . . . . 122

## Glossary

| Name                                 | Abbreviation | Description  |
|--------------------------------------|--------------|--|
| Epithelial-mesenchymal transition    | EMT          | A reversible transition from the epithelial to mesenchymal phenotype indicated by a loss of cell-cell junctions and apicobasal polarity with a corresponding gain of front-back polarity and migratory properties. |
| Transforming growth factor $\beta 1$ | TGF- $\beta$ | A multifunctional growth factor that potently induces epithelial-mesenchymal transition in an autocrine and paracrine fashion.   |
| Cellular Potts model                 | CPM          | A lattice-based statistical model used to predict cellular patterning by reducing cellular behavior to its effective energy contribution.  |
| Epithelial cadherin                  | E-cadherin   | A calcium-dependent transmembrane protein that forms the adherens junctions in cell-cell adhesion of epithelial cells.   |
| Neural cadherin                      | N-cadherin   | A calcium-dependent cellular adhesion transmembrane protein expressed in mesenchymal cells undergoing EMT.   |
| Gene regulatory network              | GRN          | A signaling scheme including mRNA, miRNA, and transcription factors which suppress or induce gene transcription.   |
| Extracellular matrix                 | ECM          | The noncellular component of tissue which provides mechanical and chemical cues to guide cellular processes.   |

*To Lani and Ipo, for their unyielding love and support*

# Chapter 1

## Introduction

Epithelial-mesenchymal transition (EMT) is a fundamental physiological process which underlies a range of morphogenic processes in development, wound healing, fibrosis, and cancer progression. Although the features and the molecular pathways of EMT have been well documented, the underlying coordination between the extracellular and intracellular signaling pathways that drive the EMT program and destabilize tissue homeostasis remains unclear. This is largely due to the difficulty of experimentally capturing the mechanical as well as chemical sequence of events that results in the spatial and temporal progression of EMT.

The goal of this work is to elucidate the interplay of mechanical and chemical signaling pathways in regulating the EMT program. In vitro and in vivo models, though they characterize the molecular pathways involved in EMT, struggle to pin down the interconnectedness of mechanical and chemical stimuli as a spatiotemporally evolving program. EMT is a complex process that variably reacts to the heterogeneous signals of the cellular microenvironment. Computational analysis provides distinct advantages

## *CHAPTER 1. INTRODUCTION*

for examining the EMT program and identifying the sequence of events which produce intermediate phenotypes. Though to definitively reproduce EMT in a computational model, a multiscale approach is needed to capture the intracellular, intercellular, and extracellular dynamics.

In Chapter 2, we provide an overview of EMT and the relevant mechanochemical signaling networks that regulate it, emphasizing the role of feedback between the cell-matrix and cell-cell junctions. In particular, we discuss the epithelial and mesenchymal phenotypes of the EMT program, its key signaling networks, and the role of the extracellular matrix composition. Chapter 2 concludes with a discussion of the relevant computational models. Chapter 3 presents the computational framework of cellular migration, with predictions of forces in an epithelial monolayer. We integrate this computational framework with an intracellular signaling network in Chapter 4 that captures gene expression throughout EMT. In Chapter 5, we discuss the relevance of these findings as well as limitations and future directions.

# Chapter 2

## Literature Review

*Sections of this dissertation chapter originally appeared in the literature*

*as*

Scott LE, Lemmon CA, Weinberg SH. Mechanochemical signaling of the extracellular matrix in epithelial-mesenchymal transition. *Frontiers* 2019.

doi: 10.3389/fcell.2019.00135

### **2.1 Introduction**

EMT is a program of phenotype regulation in which epithelial cells undergo transdifferentiation into mesenchymal cells. This is an essential process for cellular organization and tissue morphogenesis during embryonic development, and it has also been implicated in a wide array of pathological states. The phenotype states of EMT emphasize a switch in motility machinery, reflected in the downregulation of adhesion



## *CHAPTER 2. LITERATURE REVIEW*

between neighboring epithelial cells (cell-cell) and upregulation of adhesion to the underlying extracellular matrix (cell-matrix).

The epithelium is characterized by polarized sheets of cells that form by self-organization and reside in a mechanical equilibrium. Cells generate cytoskeletal tension via actomyosin contractility, which is transferred to the underlying matrix by cell-matrix attachments and to adjacent cells across cell-cell junctions. This tensional homeostasis results in a cohesive tissue structure, and is essential to maintaining barrier and signaling functions of the epithelial sheet.

This mechanical equilibrium relies on coordinated tissue scale dynamics extending beyond local cell-cell and cell-matrix adhesions. Local perturbations to the equilibrium state produce in localized stress in the monolayer and a disruption to the tensional homeostasis. The constitutive mechanical interactions between the cell and its environment are coupled to molecular signaling networks that regulate gene expression, known as EMT-activating transcription factors (EMT-TFs). In turn, EMT drives changes in the mechanics and composition of the ECM, creating a feedback loop that is tightly regulated in healthy tissues, but is often dysregulated in disease. As such, spatial patterning of mechanical stress can facilitate phenotypic regulation and is crucial to both maintenance and disruption of tissue homeostasis.

## 2.2 Epithelial-mesenchymal transition

In general, transdifferentiation from the epithelial to the mesenchymal phenotype involves disruption of cell-cell junctions, loss of apicobasal polarity which gives the epithelium its characteristic cobblestone morphology, and induction of cell migration. Hallmarks of the mesenchymal phenotype include front-back polarity, independent migration, and an elongated cell shape. The loss of epithelial characteristics often corresponds with a gain of mesenchymal characteristics such that the transdifferentiation process is both continuous and conserved. The EMT program, and its reverse process mesenchymal-epithelial transition, underlies tissue morphogenesis of both physiological processes from embryogenesis (type I) to wound healing (type II), and pathophysiological processes such as fibrosis and metastasis (type III) (1). In Sections 2.2.1 and 2.2.2, we provide further detail of the epithelial and mesenchymal phenotype, emphasizing their interactions with the microenvironment.

### 2.2.1 Epithelium

The epithelium is the first to form during embryonic development, and from it the mesenchyme develops to give rise to organ tissue structure (reviewed in (2)). The epithelium is characterized by a polarized sheet-like structure with an apical and basolateral domain that directs attachment to the basal lamina and adjacent cells. Unique to metazoa is the presence of an extracellular matrix (ECM) to which the epithelium and mesenchyme adhere. An adherent inner network of sheet-like matrices known as the basal lamina, together with an outer fibrillar matrix known as the connective tissue, stabilize the epithelial tissue architecture (further described in

## CHAPTER 2. LITERATURE REVIEW

Section 2.4). The ECM provides both mechanical and chemical cues that mediate the epithelial polarity program. Epithelial attachment to the basal lamina defines the basal membrane, whereas the apical surface is freely exposed to the luminal space, giving epithelium its apicobasal polarity (3; 4). Complete epithelial differentiation requires assembly of the basal lamina and the cell adhesion receptors that link the extracellular environment to intracellular signaling pathways (5).

Polarity complexes partition the cell-cell adhesion into an apical and basolateral. Tight junctions at the apical cuticle and focal contacts at the basal membrane organize the cytoskeleton into a subcortical belt, thereby stabilizing the cytoskeletal structure. Structural filaments anchored at focal contacts between adjacent cells mechanically couple the epithelium and stabilize the epithelial tissue architecture as a whole. The apicobasal polarity also aligns polarized tubular structures, microtubules, for transport to the apical and basolateral domains as well as proliferation along the planar axis (6).

The characteristic epithelial sheet-like structure stems from calcium-dependent homophilic bonds between adherens ectodomains, ultimately forming cell-cell junctions (7), which consist of adherens junctions, tight junctions, gap junctions, and desmosomes. The adherens ectodomains stabilize lateral epithelial contacts through trans-cis biphasic dimerization in which trans bonds initiate single pair attachments and cis bonds stabilize multi-pair adhesions (8). The cytoplasmic domain of the adherens junction consists of catenin complexes which couple cadherins to the cortical actin cytoskeleton (discussed in Section 2.3.4), forming a belt-like structure. Through these cell-cell attachments, the epithelium distributes biomechanical forces about the tissue to maintain a static equilibrium.

## 2.2.2 Mesenchyme

The mesenchyme derives from the epithelium by suppression of epithelial differentiation. Transcriptional regulation of the EMT targets cell adhesion molecules of epithelial genes, chiefly epithelial cadherin (E-cadherin) (9). Of particular importance is the disruption of the apical membrane through destabilization of tight junctions (10). Redistribution of polarity complexes away from the apical membrane disrupts the subcortical actin belt and promotes cell-matrix attachment (11).

Transdifferentiation between the epithelial and mesenchymal phenotypes is context dependent, requiring transduction of microenvironment cues by cell-cell and cell-matrix adhesions into intracellular signaling cascades. Downstream targets of these pathways, in turn, regulate cellular adhesions, polarity, cytoskeletal architecture, survival, and proliferation. Microenvironment signals such as growth factor signaling (12), and mechanical force (13) suppress epithelial differentiation by disrupting cell-cell adhesion, cytoskeletal reorganization, and remodel the extracellular matrix (14). These same pathways are characteristic of fibrosis, tumorigenesis, and metastasis (15; 16; 17; 18; 19). In particular, aberrant extracellular matrix remodeling, which underlies the characteristic tissue stiffening of fibrosis and cancer (20; 21), promotes cell-matrix adhesion and further stimulates EMT (22; 23; 24).

In comparison to epithelial cells, mesenchymal cells favor front-back polarity, cell-substrate adhesion, and a spindle-like morphology (25). Consequently, mesenchymal cells exhibit migratory behavior and rapid ECM turnover to form tissue conducive to migration. In the earliest occurrence of EMT during embryo development, the epiblast epithelium recedes posteriorly to form the mesodermal primitive streak, which later gives

## *CHAPTER 2. LITERATURE REVIEW*

rise to the neural crest as well as each distinct adult tissue (26). Hence, the earliest function of EMT produces a mesenchymal phenotype capable of migrating away from the epithelium while remaining loosely adhered to adjacent cells. Subsequent cycles of EMT revert mesenchymal cells to epithelial cells for tissue maturation, which implies reversibility of EMT (27).

## 2.3 Mechanochemical signaling networks in epithelial-mesenchymal transition

Interacting mechanical and chemical feedback loops form a signaling network for regulation of the EMT program. At the cell-cell and cell-matrix interfaces, mechanically-sensitive receptors, referred to as mechanoreceptors, transduce forces from cellular interface adhesions to intracellular signaling pathways in a process known as mechanotransduction (28). Typically, mechanical stimulation from these two sources are inversely related such that a decrease in cell-cell adhesion corresponds to an increase in cell-substrate adhesion (29). This is consistent with transcriptional regulation corresponding to a downregulation in E-cadherin and upregulation of neural cadherin (N-cadherin) observed in EMT. Both the mechanical forces at the cellular interfaces and molecular signaling cascades, known together as mechanochemical stimuli, regulate the EMT program, though the underlying coordination between the two remains unclear (30; 31; 32; 33; 34). Elucidating the role of these complex, coordinated signaling pathways in driving the EMT program is necessary for our understanding of morphogenic processes, physiological and pathophysiological alike.

### 2.3.1 Molecular signaling cascades

An EMT-associated gene regulatory network (EMT-GRN) tightly regulates EMT through molecular signaling cascades consisting of EMT-TFs and miRNAs (35; 36; 37), which maintain tissue homeostasis of an epithelial monolayer by epigenetic control of

## CHAPTER 2. LITERATURE REVIEW

epithelial and mesenchymal genes (38; 39; 40; 41). The result is a change in cellular adhesions accompanied by ECM remodeling.

Micro RNAs (miRNA), 22 base pair nucleotides of non-coding RNA, repress translation of target EMT-TFs mRNAs by binding to target genes at miRNA recognition elements. Together, miRNAs and EMT-TFs form a network of negative feedback loops that cooperatively control the switch between epithelial and mesenchymal phenotypes (9). This transcriptional regulation scheme permits biphasic mobility states with potential for phenotype reversion (42).

Signaling molecules, commonly Wnt and transforming growth factor  $\beta$  1 (TGF- $\beta$ ), and ECM proteins activate EMT-TFs, primarily the zinc finger protein SNAIL1 and basic helix loop helix zinc finger E-box-binding homeobox (ZEB), that bind E-box promoters of cell adhesion molecules, particularly the E-cadherin gene cadherin-1 (CDH1) (41), and polarity proteins to repress transcription (43; 44; 45; 46).

TGF- $\beta$  is a potent inducer of EMT by two signaling mechanisms: the canonical SMAD pathway and the non-canonical phosphatidylinositol 3-kinase (PI3K)/Akt signaling pathway (47). Both pathways favor cell migration by transcriptional suppression of E-cadherin thereby reducing cell-cell adhesion, increasing cell-substrate adhesion, and upregulating N-cadherin (48; 49; 50). In addition to repressing cell-cell adhesion, TGF- $\beta$  also induces expression of proteins associated with ECM remodeling (51) as well as cell contractility through the Rho-ROCK pathway, which is necessary for migration and ECM assembly.

Wnt targets transcriptional regulation of the epithelial phenotype by preventing ubiquitination of  $\beta$ -catenin by GSK3 $\beta$  for proteasomal degradation (52). As a result,

stabilized  $\beta$ -catenin accumulates in the cytoplasm, colocalizes with transcription factors TCF/LEF, and translocates to the nucleus where it recruits co-activators for gene transcription (53). The N-terminal domain of  $\beta$ -catenin also interacts with SNAIL1 as a transcriptional co-regulator of EMT, though the mechanism of transcription requires further investigation (54). Aberrant Wnt/ $\beta$ -catenin signaling has been identified for its role in tumorigenic and metastatic potential in the garden-variety of cancers (55; 56). The canonical Wnt/ $\beta$  pathway stabilizes nuclear localization of EMT-TFs SNAIL1 and SNAIL2 to initiate EMT. (57).

Which signaling scheme takes precedence in driving EMT is uncertain. Disruption of cell-cell junctions releases  $\beta$ -catenin for nuclear localization, although GSK3 $\beta$  phosphorylates  $\beta$ -catenin for degradation in the absence of one of the EMT-associated signaling pathways (44). Alternatively, cell-matrix mechanical feedback stimulates secretion of TGF- $\beta$ , which are sequestered into the ECM and concentrated at the cell surface to act as an EMT feedforward loop for adjacent cells (58). In fact, inhibiting ECM assembly potentially blockades EMT progression altogether (59; 60). Hence, EMT is in need of further elucidation to unravel the interplay between biochemical and biomechanical signaling.

### 2.3.2 EMT-associated gene regulatory network

Disruption of the E-cadherin junctions, nuclear translocation of  $\beta$ -catenin, and repression of the CDH1 gene by the key transcription factors SNAIL1, TWIST, and ZEB are all initiating events of EMT. EMT homeostasis is achieved by negative feedback loops between CDH1 repressors, SNAIL1 and ZEB, and CDH1 protectors, miR-200 and



miR-34 (36; 37). By upregulating mRNA SNAIL1, exogenous TGF- $\beta$ , acting through the canonical SMAD signaling pathway, destabilizes the GRN in favor of the mesenchymal phenotype(30; 31).

### 2.3.3 Mechanotransduction

Mechanical feedback between the cell and its environment is coupled to molecular signaling pathways that regulate gene expression. The epithelial cell-cell junctions mechanically couple adjacent cells and redistribute anisotropic stress throughout the monolayer (32). As a result, the epithelium acts as a cohesive structure, which allows for coordinated dynamics at the tissue scale. However, mesenchymal cells downregulate the proteins associated with cell-cell adhesion in favor of cell-matrix attachments and migration.

Integrin receptors primarily facilitate cytoskeletal coupling and downstream signaling for cell-matrix attachments. Crosstalk between the downstream cell-cell and cell-matrix adhesion signaling pathways further amplifies transcriptional regulation of the EMT program (34), discussed further in Section 2.3.4.

### 2.3.4 Cell-matrix and cell-cell adhesion

Integrin receptors not only relay mechanical feedback by transcriptional regulation but also through crosstalk with mechanoreceptors at the cell-cell interface (61). Integrin binding destabilizes the adherens junction through focal adhesion kinase (FAK)/Src signaling and actomyosin contractility, resulting in E-cadherin endocytosis (62; 63; 64).

The E-cadherin ectodomain forms trans and cis homodimeric bonds with E-cadherin on both the same cell and adjacent cell (65), and the cytoplasmic domain colocalizes with a catenin complex -  $\beta$ -catenin,  $\alpha$ -catenin, and p120 - to bind to the actin cytoskeleton (66). The nascent cell-cell junctions are punctate attachments consisting of the scaffolding protein nectin, an immunoglobulin-like calcium independent cell-cell adhesion protein. Through Rho GTPase-mediated cytoskeletal rearrangement and E-cadherin recruitment, nectin facilitates maturation of nascent punctate adhesions into a compacted adherens junction, which provides a scaffold for the assembly of a subcortical actomyosin contractile belt (67). Subsequent Rho/ROCK stimulates apical membrane contraction, compacting the punctate E-cadherin dimers into a mature adherens junction (68). This compaction process additionally recruits Rac for downstream PI3K activation of Akt, which in turn recruits paxillin to the E-cadherin junctions by an mTor/PKC $\alpha$ /RhoA signaling cascade and stabilizes the cytoskeleton-to-adherens junction (69).

### 2.3.5 Mechanotransduction of cell-cell junctions

Disruption of the adherens junction during EMT releases components of the cadherin complex to translocate to the nucleus and further downregulate E-cadherin expression (66; 70). In particular,  $\beta$ -catenin cooperatively acts with transcriptional factors ZEB, TWIST, and SNAIL1 to repress the E-cadherin gene, CDH1. Furthermore, cytoskeletal stress, which is no longer distributed across the adherens junction to neighboring cells, transfers to cell-matrix attachments (71). In response, the epithelial and mesenchymal genes orchestrate transdifferentiation through a spectrum of partial EMT phenotypes, each having a distinct propensity for cell-cell and cell-matrix adhesion. The end result

of the mesenchymal phenotype is a cadherin-type switch from E- to N-cadherin, which promotes cellular migration through lamellipodial and filopodial outgrowth (72; 73; 74). Yet, the extent to which disruption of cell-cell junctions drives the EMT program is unclear.

### **2.3.6 Mechanotransduction in disease**

Healthy adult tissue has an optimal stiffness sensed by cell adhesion molecules that transduce mechanical feedback from the microenvironment to intracellular signaling pathways (75). These cell adhesion molecules that transduce mechanical feedback also stimulate cytoskeletal reorganization through associated mechanosensing cytoskeletal-linked proteins such as vinculin and talin (76). Tissue stiffness has been identified as a marker for a number of diseases (77). In particular, identification of tissue stiffening as a marker of cancer progression and a precursor to metastasis (78) illustrates the importance of the mechanical mechanisms underlying EMT as potential targets for novel therapies (79).

## 2.4 Cell-matrix mechanochemical feedback

A downstream effect of EMT is ECM remodeling from an epithelial ECM to a fibrous ECM. Epithelial tissue, consisting of a thin, dense specialized ECM known as the basement membrane, provides a structural scaffolding at the basal membrane for epithelium attachment (80). Feedback at these cell-matrix attachments establishes the apicobasal axis and stabilizes the monolayer (81). Typically, the epithelium exhibits normal physiological function when in contact with the basement membrane, but not when exposed to fibrillar matrix components.

Unlike the basement membrane, mesenchymal ECM is fibrous and crudely aligned. Although connective tissue lacks inherent organization, cell traction forces pull the fibers into alignment parallel to the direction of applied force. This is of particular interest when exploring mechanical response of the extracellular matrix, and the reciprocal mechanical regulation of cellular processes.

### 2.4.1 Basal lamina and epithelial-mesenchymal transition

Nidogen and perlecan bridge the innermost cell-adherent layers of the basement membrane, the laminin-rich lamina lucida and collagen IV-rich lamina densa, to form a supramolecular, reticular structure known as the basal lamina (82). Cytoskeletal recruitment, stimulated by cell adhesion to the basal lamina, strengthens focal contacts and reinforces the epithelial tissue architecture. Developmental studies indicate that laminin not only maintains epithelial differentiation but is also the progenitor of the basement membrane and epithelial polarization during gastrulation (reviewed in (83)),

## CHAPTER 2. LITERATURE REVIEW

suggesting laminin contributes to epithelial differentiation rather than mesenchymal suppression (84; 85).

Laminins self-assemble into a sheet-like matrix at the cell surface and mediate cell attachment to integrin, dystroglycan, sulfated glycolipids, and heparan sulfate chains (86). The laminin-specific integrin receptor  $\alpha_3\beta_1$  localizes to the cytoplasmic plaque of cell-cell junctions, where it forms a complex with  $\alpha$ -actinin and links the subcortical actin network to the catenin complex of cell-cell junctions (87), contributing to the integrity of the epithelium by reinforcing cell-cell junctions. Integrin  $\alpha_6\beta_4$  is localized to a multiprotein complex known as the hemidesmosome, which anchors the cytoskeleton to the basal lamina, provides attachment for intermediate filaments, and further stabilizes the epithelium (88).

Despite its role in maintaining epithelial differentiation, elements of the basal lamina can also promote EMT. For example, laminin receptors  $\alpha_3\beta_1$  and  $\alpha_6\beta_4$  have been implicated in EMT and cancer progression in which integrin ligation was sufficient for tumor formation (89). Integrin-linked downstream signaling pathways were shown to activate EMT-associated FAK, Rac1, MAPK, and JNK pathways(90).

Studies of alveolar epithelium(91; 92) and hepatocellular carcinoma(93) demonstrate cooperative activity between  $\alpha_3\beta_1$  and transforming growth factor  $\beta_1$  (TGF- $\beta$ ) to suppress the epithelial phenotype. Colocalization and endocytosis of  $\alpha_3\beta_1$  with the TGF- $\beta$  receptor type I (TGF $\beta$ RI) receptor led to formation of a pSmad2- $\beta$ -catenin transcription complex, though it is unclear how this complex suppresses the epithelial phenotype. A separate study in immortalized mouse keratinocytes demonstrated that  $\alpha_3\beta_1$ -TGF- $\beta$  cooperativity induces tissue remodeling of the basal lamina (94; 95) and induces epithelial EMT-TFs,

SNAIL1 and SNAIL2 (64). Hepatocellular carcinomas overexpressing  $\alpha_6\beta_4$  exhibit aberrant cell proliferation and invasion associated with downregulation of the epithelial phenotype by PI3K/Akt signaling dependent upregulation of SNAIL2 (96).

## 2.4.2 Fibrous matrix and epithelial-mesenchymal transition

Assembly of fibrillar matrix on the basement membrane plays a significant role in repressing the epithelial phenotype and inducing EMT. Fibronectin, a 230-270 kDa fibrous glycoprotein that provides a scaffold for cell attachment (97), is secreted as a soluble dimer and requires integrin attachment and cell contractility for polymerization into an insoluble fibrillar matrix (98; 99). Integrin binding facilitates fibronectin stretch, which exposes additional binding sites for ECM deposition and growth factor binding (100). Primarily integrins  $\alpha_5\beta_1$  and  $\alpha_v\beta_3$  dynamically bind to the fibronectin matrix to extend pseudopodia and form contractile filaments via small GTPases (101).

Dysregulation of fibrillar matrix is widely implicated in fibrosis(102) and cancer progression (103; 104; 105), owing to the suppression of epithelial differentiation (106). As a downstream target of Wnt (107) and TGF- $\beta$ (108) signaling, fibronectin is a marker of mesenchymal differentiation (109). Fibronectin accumulation at cleft-forming sites during salivary gland and lung branching morphogenesis induces SNAIL2 to suppress the epithelial phenotype (110).

Fibrillar collagens, acting through canonical  $\beta_1$  integrin/FAK/Src signaling, suppress epithelial differentiation at the transcriptional level and disrupt the cadherin complex to enhance cell mobility (reviewed in (111)). In ovarian and prostate cancer cells, collagen- $\beta_1$  binding alters E-cadherin expression through both PI3K- (112) and Src-dependent

## CHAPTER 2. LITERATURE REVIEW

mechanisms (113). Collagen I promotes Snail and LEF1 through ILK-dependent activation of NF- $\kappa$ B and inhibition of GSK3 $\beta$ , which drives transcriptional activation of SNAIL1 (114). In a separate study of pancreatic carcinoma cells, DDR1 and  $\beta$  integrin concomitant activation converges on JNK signaling to increase expression of N-cadherin, a mesenchymal marker of EMT (115).

Given its role in maintaining adherens junctions, collagen-DDR signaling may indicate a switch from cell-cell to cell-matrix adhesion. Switching from epithelial-associated to mesenchymal-associated DDR drives mesenchymal differentiation by activating and stabilizing EMT transcription factors SNAIL1 and ZEB, and by inducing gelatinases to promote invasion (reviewed in (116)). Collagen I-DDR2 ligation induces invasion of metastatic mammary epithelium in vivo and in vitro by activating Src/ERK signaling to induce SNAIL1 (117). Similarly, TGF- $\beta$ -induced DDR2 expression in human renal proximal tube epithelial cells suppresses the epithelial phenotype via NF- $\kappa$ B and LEF-1 activation (118). These studies indicate that fibrillar collagens, and also other collagenous ECM (119; 120; 121; 122), are active EMT through downstream transcriptional suppression of the epithelial phenotype as well as disruption of cell-cell junctions.

### 2.4.3 Connective tissue and growth factor tethering.

Just as in the basal lamina, proteoglycans of connective tissue sequester soluble factors as a means to regulate bioavailability or to spatially confine activation. Neighboring the primary cell attachment domain of fibronectin, a growth factor binding domain localizes growth factor signaling near the cell attachment for simultaneous activation of signaling

## CHAPTER 2. LITERATURE REVIEW

pathways that promote survival and migration(123). One example of this in EMT is the latent TGF- $\beta$ -binding protein (LTBP), which binds to fibronectin at the type III<sub>12-14</sub> repeat and sequesters TGF- $\beta$  in a conformationally latent form until mechanically or proteolytically activated (124; 125). Confining TGF- $\beta$  to the ECM in this latent form allows for spatial and temporal control over TGF- $\beta$  activation (126). In the ECM-bound latent form, TGF- $\beta$  is activated through cell contractility or proteolytic cleavage. The  $\alpha_v$  integrins, namely  $\alpha_v\beta_6$  and  $\alpha_v\beta_8$ , bind to the RGD sequences in fibronectin and latent TGF- $\beta$  complex LAP to conformationally alter LAP and activate TGF- $\beta$  (127).

Taken together, conventional integrin signaling and growth factor availability regulation represent two distinct but interacting mechanisms by which fibrillar ECM regulates EMT (128). Previous studies of mammary breast epithelium suggest fibronectin, but not laminin, is necessary for TGF- $\beta$ -induced EMT, likely due to binding the fibronectin receptor  $\alpha_5\beta_1$  integrin and latent TGF- $\beta$  localization (59; 60). Fibronectin receptor  $\alpha_v\beta_3$  integrin has also been shown to phosphorylate TGF $\beta$ RII at Y284 to activate p38/MAPK signaling, separately from canonical Smad signaling, and promote tumor invasion (129).

### 2.4.4 Tissue remodeling and epithelial-mesenchymal transition

Tissue remodeling in development (130) and tissue repair (131; 132) requires fine spatiotemporal control over ECM degradation, which is often dysregulated in fibrosis (133; 134; 135) and cancer progression (136; 137; 138; 139). Through proteolysis of the ECM and its sequestered latent signals, MMPs modify the molecular and mechanical



## CHAPTER 2. LITERATURE REVIEW

characteristics of the extracellular microenvironment to facilitate cellular migration (140).

Beyond the structural effects on ECM, MMP proteolytic processing of the basal lamina produces bioactive fragments (141), many of which regulate angiogenesis (142) and migration (143) in a paracrine fashion. For example, collagen IV fragment  $\alpha_5$  binds collagen receptor DDR1, preventing distribution to cell-cell junctions, and activates ERK (144), a downstream signal of TGF- $\beta$ -induced EMT (49; 145), and a laminin-111  $\beta$ -chain fragment competitively binds  $\alpha_3\beta_1$  integrin to upregulate mesenchymal markers and switch gelatinase A (MMP2) production in the inner lamina lucida to gelatinase B (MMP9) in the outer lamina densa and reticular lamina.

Additionally, MMPs dock with cell adhesion receptors, facilitating proteolytic activation of latent signaling molecules sequestered within the ECM and inducing survival and migratory signaling pathways (146; 147; 148). Gelatinases (149), stromelysin (MMP3) (150), and membrane type (MT)-MMPs (151) each proteolytically activate latent form of TGF- $\beta$ , which subsequently upregulates gelatinases thereby creating a self-sustaining loop of matrix remodeling (152).

One last mechanism by which tissue remodeling drives EMT is by MMP-mediated receptor shedding. MT-MMP (153), MMP3 (154), MMP9, and matrilysin (MMP7) (155) localize at the adherens junctions to shed the E-cadherin ectodomain, producing a soluble fragment frequently increased in the serum of cancer patients (156). The 80 kDa ectodomain fragment acts as a paracrine/autocrine signal that reduces cell aggregation by competitive homophilic binding with E-cadherin (157) and promotes MMP production

via EGFR (158). MMP3 additionally cleaves E-cadherin, which specifically activates Rac1 splice variant Rac1b that in turn activates the EMT-TF SNAIL (159).

### **2.4.5 Cell-matrix mechanical feedback and epithelial-mesenchymal transition.**

In addition to the compositional aspects of ECM-EMT regulation, mechanical feedback at cell-matrix interfaces is an important regulator of EMT (160). Mechanical coupling between a cell and its environment allows for rapid signal transduction and propagation across the tissue. The cell adhesion receptors and focal adhesion proteins which transduce ECM feedback to intracellular signaling cascades, reorient the cytoskeleton to mitigate anisotropic tension (161). Prior studies have demonstrated that induction of EMT is dependent on the mechanical properties of the underlying tissue; *in vitro*, TGF- $\beta$  induces EMT on surfaces with a high elastic modulus yet induces apoptosis on surfaces with a lower elastic modulus (23). Inherent tension within a tissue also induces EMT; areas of higher stress within a colony of epithelial cells correlates with EMT, while areas of lower stress maintain the epithelial phenotype (162).

Deposition and organization of the ECM is sensitive to substrate stiffness (163) such as in the case of fibronectin assembly (164). A proposed mechanism suggests that stretch of fibronectin type III repeats exposes additional growth factor and ECM binding sites that promotes further ECM deposition (99). This interplay between substrate stiffness and ECM remodeling facilitates excessive matrix deposition and further stiffening of the ECM (165).

## CHAPTER 2. LITERATURE REVIEW

In addition to matrix deposition, the effects of matrix stiffening may enhance signaling of tethered growth factors. In alveolar epithelial cells, fibronectin facilitates stiffness-dependent EMT induced by TGF- $\beta$ . The requirement for integrin  $\alpha_v$  that binds both fibronectin and the TGF- $\beta$  complex suggests cell contractility mediates the substrate stiffness response to TGF- $\beta$ -induced EMT (166). The  $\alpha_v$  integrin activates latent TGF- $\beta$ , which in turn induces LOX-mediated ECM crosslinking of collagen and ECM stiffening (167; 168). In NMuMG cells, matrix rigidity regulates the switch from TGF- $\beta$ -induced apoptosis and to EMT via a FAK/PI3K/Akt signaling cascade (23). These studies indicate integrin receptors mediate the activation of fibronectin-TGF- $\beta$ -induced EMT in a contractility-dependent manner.

Although mechanical feedback drives rearrangement of cytoskeletal components to induce EMT (reviewed in (169)), it also facilitates actin recruitment to reinforce adherens junctions on stiff substrates (170). Tensile forces unfolds  $\alpha$ -catenin to reveal cryptic vinculin-binding sites, which nucleate polymerization of actin microfilaments (171). The exact sequence of events regulating this switch are unclear.

## 2.5 Computational models of molecular, cellular, and tissue scale phenomena

### 2.5.1 Cellular Potts model

The CPM, deriving from the statistical mechanics large- $q$  Potts model, is a two-dimensional square lattice model, which applies thermodynamic constraints as a general basis for cell sorting and is often useful for predicting cell migration (172; 173). These thermodynamic constraints are described by an energy function, the Hamiltonian, that summarizes cellular phenomena as a contributor to probabilistic behavior. The Hamiltonian is expressed as a function of contact costs between neighboring lattice sites. By delineating the energy contribution of cellular phenomena to the net energy of the cell, both simple and complex cellular processes are therefore translated into succinct thermodynamic terms for simulation.

Van Oers and colleagues, in particular, apply the CPM to predict formation of vascular structures resulting from cell-matrix mechanical feedback (174). To simulate cell-matrix feedback the CPM cells additionally occupy a finite element mesh, which simulated cell traction forces deflect to produce substrate strain. Resulting substrate strains reduce the net energy cost of cellular extension, which emulate filopodial and lamellipodial extensions, into neighboring lattice domains. Similar studies have applied the CPM to describe the role of cell-cell and cell-matrix feedback in regulating EMT (175) and cardiac cushion morphogenesis (176).

## 2.5.2 Cellular Potts model and extracellular matrix remodeling

Daub & Merks (177) also have applied the CPM to determine the relative effects of chemotaxis, haptotaxis, and ECM remodeling on endothelial sprouting. However, in comparison to the van Oers approach, the lattice sites not occupied by cells contain dense ECM, which restricts cell movement at the migratory front. Membrane-bound matrix metalloproteinases (MMP), a group of enzymes that break down ECM, locally digest the ECM and cells consequently migrate towards favorable regions of ECM density, i.e. haptotaxis.

## 2.5.3 Epithelial-mesenchymal transition gene regulatory network

Previous *in vitro* work has identified a TGF- $\beta$ -sensitive gene regulatory network of EMT through master transcriptional regulators SNAIL1 and ZEB with miR-34 and miR-200 counterparts (178; 179; 180). Tian and colleagues proposed a dynamical system of cascading bistable switches (CBS), which consists of two double negative feedback loops that regulate this EMT-GRN (181) (further described in Chapter 4). The CBS model predicts the stability of phenotype states - i.e. epithelial, intermediate, and mesenchymal - during EMT when exposed to exogenous TGF- $\beta$ . This study reveals a latent partial mesenchymal phenotype capable of reversion to the epithelial phenotype, which is consistent with *in vitro* observations (27; 182; 183; 184). Zhang et al. (42) subsequently validated these predictions *in vitro* and revise the CBS model to account for additional configurations of mRNA-miRNA complexes.

## 2.5.4 Mechanotransduction at the adherens junction

For mechanotransduction at cell-cell junctions,  $\beta$ -catenin provides a reasonable approximation to the cell bound/unbound state as it is either localized at the cell-cell junctions or in the nucleus. Ramis-Conde and colleagues (185) developed a dynamical system of  $\beta$ -catenin localization within the cell dependent on the cell bound/unbound state. This model predicts the mobility of cells within a monolayer from  $\beta$ -catenin concentration, and suggests  $\beta$ -catenin nuclear translocation is a sufficient perturbation to cell-cell adhesion for EMT-like events to occur.

## 2.6 Summary

Our understanding of the EMT program has advanced from its first description as two distinct phenotype states to a spectrum of partial phenotypes sensitive to mechanical and chemical cues. Together, the mechanochemical signaling pathways form a coordinated regulatory network converging on a small number of epithelial and mesenchymal genes. Figure 2.1 shows an overview of the relevant mechanochemical signaling pathways considered for this work. First, E-cadherin junctions form the main adhesion between adjacent cells and distribute the junction force across cell-cell contacts (Step 1). E-cadherin further regulates  $\beta$ -catenin signaling, which is either localized at the cell-cell adhesion, destroyed by the proteasome, or localized in the nucleus (Step 2). As a transcriptional regulator,  $\beta$ -catenin suppresses CDH1 and reduces available E-cadherin as a result (Step 3). The EMT-GRN is also regulated by TGF- $\beta$  signaling (Step 4), which additionally suppresses E-cadherin and upregulates ECM production and remodeling (Step 5).

In this work, we develop a multiscale computational framework of the mechanochemical regulation of the EMT program (Fig. 2.2). In Chapter 3, we begin with the CPM-FEM to evaluate the effect of cell-matrix mechanical feedback on general cell organization and predict traction and junction forces within an epithelial monolayer (Fig. 2.2, blue blocks). We introduce cell proliferation and determine the connectivity of adjacent cells, which is then used for evaluating the traction forces of the multicellular cluster from the FMA model. The junction force predictions are then implemented in Chapter 4 to determine the bound/unbound state of adjacent cells for mechanical regulation of the EMT-GRN (Fig. 2.2, red block). The gene expression is tracked for

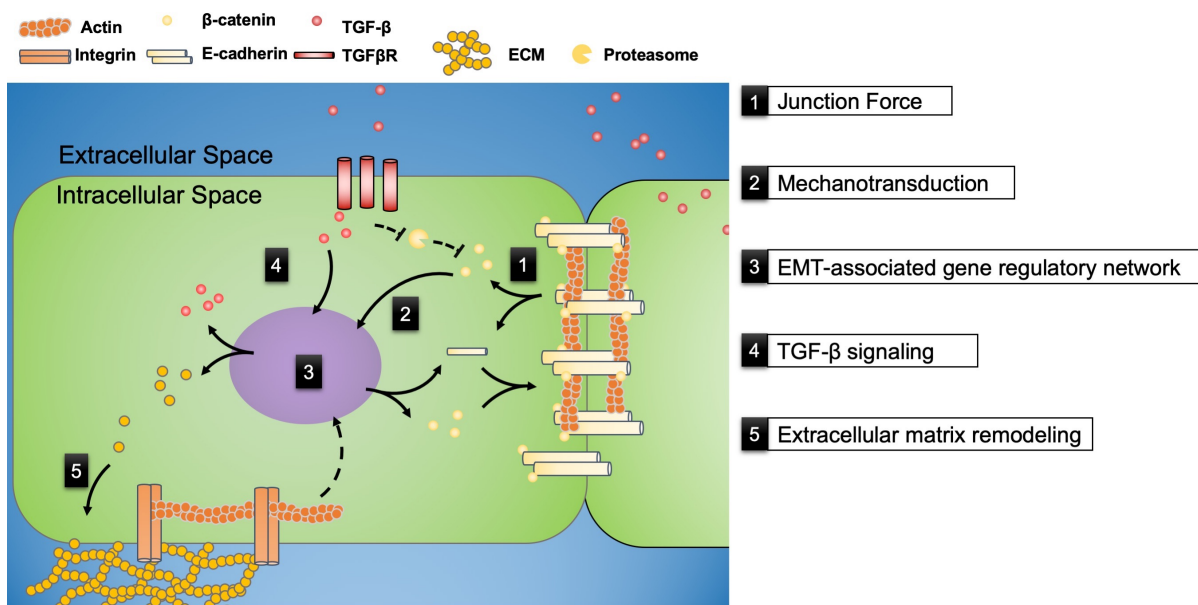


**Figure 2.1.** Overview of the mechanochemical signaling framework discussed in this work.

each cell throughout the simulation, from which we estimate the phenotype of each cell. A comprehensive parameter analysis additionally identified particular combinations of contact energies for approximating TGF- $\beta$ -dependent effects on cell mobility for implementation in Chapter 4, Section 4.3.4. The phenotype then sets CPM cell properties defined for a continuum of EMT states, from epithelial to mesenchymal.

An additional output of the EMT-GRN is the mesenchymal marker, fibronectin. Cell traction forces assemble fibronectin fibrils while fibronectin fibrils facilitate cell-matrix attachment (164). Using the traction forces predicted by the FMA model together with production of ECM, we can predict ECM remodeling downstream of the EMT program (Fig. 2.2, yellow block). The traction forces subsequently assemble fibronectin fibrils which facilitate cell-matrix attachment, reflected in the force-distance scaling factor used in the FMA (Chapter 3, Section 3.2.3). In turn, this ECM remodeling alters the



mechanical properties of the finite element mesh and cell-matrix contact penalty as described by Daub & Merks (177). We anticipate that fibronectin fibrillogenesis, together with TGF- $\beta$  stimulation, will drive a spatially localized positive feedback loop sufficient to induce EMT. We leave the EMT-dependent regulation of the ECM for future work.

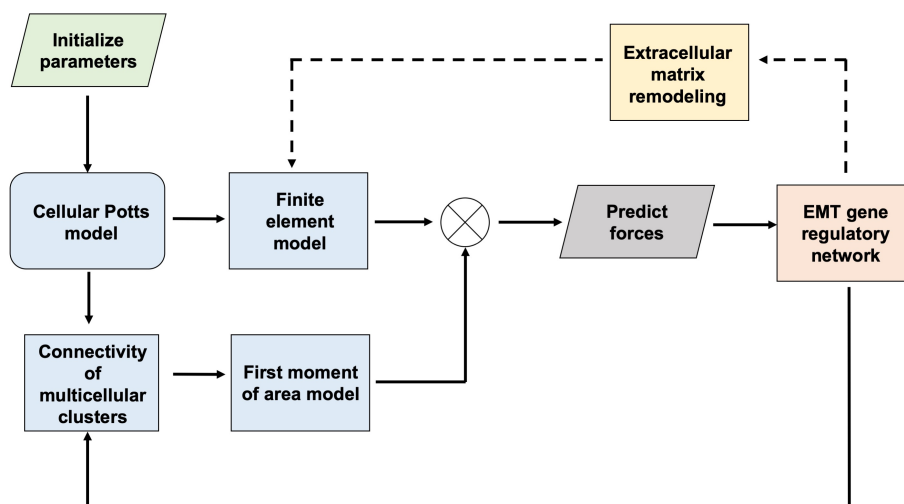


**Figure 2.2.** The computational framework described in this work consists of subsystems intended to predict the dynamics at the molecular, cellular, and organ scale.

# Chapter 3

## Mechanical cell-cell feedback of the epithelial monolayer

*This chapter is currently available in preprint as*

Scott LE, Griggs LA, Narayanan V, Conway DE, Lemmon CA, Weinberg SH. A Predictive Model of Intercellular Tension and Cell-Matrix Mechanical Interactions in a Multicellular Geometry. *bioRxiv*. 2019. doi: 10.1101/701037

### 3.1 Introduction

In Chapter 3, we explore the role of cellular adhesion in maintaining tensional homeostasis of epithelial monolayers. Previously, van Oers and colleagues developed a CPM coupled with a finite element model (FEM) to examine the role of mechanical feedback of the extracellular matrix in guiding cellular migration and alignment (174). To simulate epithelial monolayers, we extend the CPM-FEM capabilities of simulating

### CHAPTER 3. CPM

individual cellular traction forces to predict junctional forces in a multicellular cluster. Traction forces are determined from the first moment of area (FMA) about the single cell geometry, as previously modeled and validated by Lemmon & Romer (186). The FMA model approximates cellular traction forces at discrete points within the individual cell geometry with magnitude proportional to the distance from and direction oriented towards the cell centroid. These traction forces generate substrate strains which, in addition to cell-cell and cell-matrix interactions, impose a thermodynamic constraint and govern the dynamics of individual cells in the CPM.

First, we incorporate the formation of cell-cell adhesion between neighboring cells to accurately represent the biology of epithelial cells. Next, we extend the FMA model to multicellular clusters, and model traction forces based on the multicellular geometry rather than the single cell geometry. As a result, individual cell traction forces are proportional in magnitude to the distance from the centroid of the multicellular cluster, rather than the single cell centroid. We also explore the collective cell dynamics of the CPM-FEM to an *in vitro* model of epithelial monolayer dynamics, using the relative monolayer characteristics to approximate the CPM timescale for use in Chapter 4. The findings presented here are further generalized to a one-dimensional model of force distribution within a monolayer, which provides a simple method for approximating junctional force distribution *in vitro* using the multicellular geometry. We then apply these junctional force and cell-cell adhesion predictions in Chapter 4 to model the mechanotransduction signaling pathway.

## 3.2 Methods

In this study, we apply the CPM to simulate epithelial monolayer dynamics (172). The cell-occupied lattice is superimposed on a finite element lattice to determine substrate strains from simulated traction forces. In particular, we extend the FMA prediction of single cell traction forces to predict the traction forces of a multicellular cluster based on its geometry. Lastly, we predict cell-cell junction forces by requiring that 1) cells in contact are mechanically coupled through cell-cell junctions, 2) the forces at these junctions balance net traction forces for each cell, and 3) the junction force is equal and opposite across a cell-cell adhesion.

### 3.2.1 Cellular Potts model

The domain of the CPM lattice  $\Omega \subset \mathbb{Z}^2$  contains interconnected sites  $\vec{x} \in \Omega$  with spins  $\sigma_{\vec{x}} \in \mathbb{Z}_{\geq 0}$  to identify the configuration of the domain. Each distinct cell-occupied site is defined by  $\sigma_{\vec{x}} \in \mathbb{N}$ , and an unoccupied site, i.e. extracellular matrix, is defined by  $\sigma_{\vec{x}} = 0$ . The CPM approximates the effective energy for a system configuration using a Hamiltonian term, where each term reflects a characteristic of biological cells and together summarize the configuration energy of the system. Here, the Hamiltonian is given by the sum of three terms

$$H = H_{area} + H_{contact} + H_{durotaxis}, \quad (3.1)$$

and Boltzmann statistics determine the probability of a possible lattice configuration

$$P(H) = e^{-H/T}, \quad (3.2)$$

where  $H$  is the Hamiltonian defined in 3.1,  $k$  is the Boltzmann constant, and  $T > 0$  is a temperature term that captures intrinsic cell motility.

The area term  $H_{area}$  approximates the cell area constraint as a deviation of the cell area relative to the target area such that

$$H_{area} = \sum_{\sigma} \lambda_{area} \left( \frac{a(\sigma_{\vec{x}}) - A_0}{A_0} \right)^2, \quad (3.3)$$

where  $a(\sigma_{\vec{x}})$  is the area of a given cell determined by number of lattice sites occupied by that cell,  $A_0 = 312.50 \mu\text{m}^2$  is the target area for all cells, and  $\lambda_{area} = 500$  is an elasticity coefficient that maps deviations from the target area to a magnitude of energy.

The contact term  $H_{contact}$  represents costs due to contact between neighboring pixels, with different energies associated with cell-cell and cell-matrix interfaces:

$$H_{contact} = \sum_{(\vec{x}, \vec{x}')} J(\sigma_{\vec{x}}, \sigma'_{\vec{x}}) (1 - \delta(\sigma_{\vec{x}}, \sigma'_{\vec{x}})), \quad (3.4)$$

where  $J(\sigma_{\vec{x}}, \sigma'_{\vec{x}})$  defines the interaction energy between adjacent lattice sites  $(x, x')$  and  $\delta(\sigma_{\vec{x}}, \sigma'_{\vec{x}})$  is the Kronecker delta function defined as 1 if  $\sigma_{\vec{x}} = \sigma'_{\vec{x}}$  and 0 otherwise. We specify the cell-cell interface energy  $J(\sigma_{\vec{x}}, \sigma'_{\vec{x}})$  as  $J_{cc}$  and cell-matrix interface energy  $J(\sigma'_{\vec{x}}, 0)$  as  $J_{cm}$ .

CHAPTER 3. CPM

Lastly, the durotaxis term  $H_{durotaxis}$  introduced in van Oers (174) mimics the tendency for cell migration along gradients of mechanical strain. In particular, this term captures preferential cellular extension into lattice sites of higher strain

$$H_{durotaxis} = -g(\vec{x}, \vec{x}') \lambda_{durotaxis} \left( h(E(\varepsilon_1)) (\vec{v}_1 \cdot \vec{v}_m)^2 + h(E(\varepsilon_2)) (\vec{v}_2 \cdot \vec{v}_m)^2 \right). \quad (3.5)$$

The  $\lambda_{durotaxis} = 1$  term determines cell sensitivity to durotaxis;  $g(\vec{x}, \vec{x}')$  is 1 if a cell extends into a target site  $\vec{x}'$  and -1 if a cell retracts; and  $v \cdot v_m$  ensures extension and retraction are greatest parallel to the major and minor principal strain axes,  $v_1$  and  $v_2$  respectively, and negligible perpendicular to it. The sigmoid function  $h(E)$  captures the preference for stiffer substrates

$$h(E(\varepsilon)) = \frac{\alpha}{1 + e^{-\beta(E(\varepsilon) - E_\theta)}}, \quad (3.6)$$

which assumes this preference has a minimal stiffness for spreading and reaches a maximum  $\alpha = 10$  at rate  $\beta = 5 \times 10^{-4} \text{ kPa}^{-1}$  and the half-max stiffness as  $E_\theta = 15 \times 10^3 \text{ kPa}$ .  $E(\varepsilon)$  is the cell perception of substrate strain stiffening

$$E(\varepsilon) = E_0 \left( 1 + \frac{\varepsilon}{\varepsilon_{st}} \right), \quad (3.7)$$

where  $\varepsilon_{st} = 0.1$  determines the rate of strain-stiffening,  $\varepsilon$  is the substrate strain, and  $E_0 = 10 \text{ kPa}$  is the Young's modulus of the substrate. The strain-stiffening only affects cell perception of strain-stiffening, not the stiffening of the finite element mesh itself (Section 3.2.2).

### 3.2.2 Finite element analysis

To describe the substrate strain that governs durotaxis, we assume that a uniform, isotropic, and linearly elastic two-dimensional substrate deforms to cellular traction forces projected from the CPM. The CPM lattice is mapped to the finite element lattice by relating each CPM lattice element to a finite element node such that  $(x, y) = (x \pm 1, y \pm 1)$ . By applying the preconditioned conjugate gradient method, we iteratively solve the linear system

$$\underline{\underline{K}}u = \underline{\underline{f}}, \quad (3.8)$$

for the displacement  $u$  at each node, where  $K$  is the global stiffness matrix assembled from the stiffness matrix of each element, and  $f$  is the applied traction forces with constraint  $u = 0$  at the CPM lattice boundary. In maintaining constant material properties during deformation, the element stiffness matrices  $\underline{\underline{K}}_e$  are given by

$$\underline{\underline{K}}_e = \int_{\Omega_e} \underline{\underline{B}}^T \underline{\underline{D}} \underline{\underline{B}} d\Omega_e \quad (3.9)$$

where  $B$  is the conventional strain-displacement matrix and  $D$  is the material property matrix under plane stress conditions

$$\underline{\underline{D}} = \frac{E}{1 - \nu^2} \begin{bmatrix} 1 & \nu & 0 \\ \nu & 1 & 0 \\ 0 & 0 & \frac{1}{2}(1 - \nu) \end{bmatrix}. \quad (3.10)$$

relating the Young's modulus,  $E = 10 \text{ kPa}$ , and Poisson's ratio,  $\nu = 0.45$ , assuming planar stress. Lastly,  $B$  relates the local node displacements to the local strains by

$$\underline{\varepsilon} = \underline{B}u_n \quad (3.11)$$

in which  $\underline{\varepsilon}$  is a vector of the strain tensor  $\underline{\underline{\varepsilon}}$ .

### 3.2.3 Traction forces

Prior work of van Oers and colleagues (174) assume that individual cell geometry relates to traction forces in the CPM by the FMA. Application of the FMA model to single cell geometries is previously described by one of the senior authors of this work (186). In brief, the single cell FMA model assumes that each node  $i$  in a CPM cell  $\sigma$  exerts a force on all other nodes  $j$  in the same cell that is proportional to the distance between those nodes  $\vec{d}_{i,j}$ ,

$$\vec{F}_i = \mu \sum_j \vec{d}_{i,j}, \quad (3.12)$$

where  $\mu$  is a scaling factor that relates cell geometry to traction forces. For simplicity, we assume  $\mu = 1 \text{ nN } \mu\text{m}^{-1}$  and report forces as relative arbitrary units (a.u.). As shown in Lemmon and Romer (186), the resulting traction force at each CPM node is directed towards the cell centroid with magnitude proportional to the distance from the node to the centroid.

Here, we extend these previous works of the FMA model to describe the magnitude and direction of traction forces acting about a point in a multicellular geometry. For



the multicellular FMA model, we assume that the boundary of two cells constitutes a cell-cell adhesion such that two or more adjacent cells behave as a single structural unit or cluster. We define an adjacency matrix  $A$ , where  $A$  is a  $N_{cell} \times N_{cell}$  matrix, such that  $A_{\sigma,\sigma'} = 1$  if cells  $\sigma$  and  $\sigma'$  are in contact, and 0 otherwise. By definition,  $A$  is symmetric. A cluster is defined as the connected components of the undirected graph defined by  $A$ .

Thus, the multicellular FMA model defines the traction force at each node in each CPM cell as directed towards the centroid of the associated multicellular cluster, with magnitude proportional to the distance from the node to the cluster centroid. Consistent with this hypothesis, recent experimental evidence supports an increase in traction forces with increasing multicellular cluster size (187; 188) For the case of a cluster comprised of a single cell, i.e., a cell lacking cell-cell adhesion, the multicellular FMA and single cell FMA model are equivalent.

### 3.2.4 Intercellular tension

By construction, the single cell FMA model dictates that the sum of traction forces of an individual cell, i.e., the net traction forces  $\vec{T}_\sigma = \sum_{i \in \sigma} \vec{F}_i$  for cell  $\sigma$ , is equal to 0. In contrast, using the multicellular FMA model, the net traction forces of an individual cell  $T_\sigma$  within a cluster may not be equal to 0. Adapting a recent approach by Ng and colleagues (189), we hypothesize that junction forces are a reaction force, balancing the net traction force to maintain static equilibrium of each cell in a multicellular cluster. The multicellular FMA model is applied to calculate  $T_\sigma$  for each cell, and then we impose mechanical equilibrium on the multicellular clusters by relating the traction force to force across the cell-cell adhesion, such that for all cells  $\sigma$ ,

$$\sum_{\sigma' \in n_\sigma} \vec{J}_{\sigma, \sigma'} + \vec{T}_\sigma = 0, \text{ for } \sigma \in (1, \dots, N_{cell}), \quad (3.13)$$

where  $n_\sigma$  defines the set of “neighbors” of cell  $\sigma$ , i.e.,  $A_{\sigma, \sigma'} = 1$ , and  $J_{\sigma, \sigma'}$  is the junction force from cell  $\sigma'$  to cell  $\sigma$  (see S1 Figure). Eq. 3.13 defines  $N_{cell}$  linear equations, with  $N_{cell}^2$  unknown  $J_{\sigma, \sigma'}$  terms. We further constrain the junction force calculations by assuming that junction force pairs are equal in magnitude and opposite in direction, i.e.,

$$\vec{J}_{\sigma, \sigma'} + \vec{J}_{\sigma', \sigma} = 0, \quad (3.14)$$

for all  $(\sigma, \sigma')$  such that  $A(\sigma, \sigma') = 1$ .

Combining Eqs. 3.13 and 3.14, we arrive at a linear system with a set of  $N_{cell} + N_{junc}$  equations and  $N_{cell}^2$  unknowns (see S1 Figure), where  $N_{junc}$  is the number of intercellular junctions, which can be determined by the sum of the terms above (or below) the main diagonal of  $A$ , with a maximum value of  $N_{cell}(N_{cell} - 1)/2$ . In practice, linear systems for Eqs. 3.13 and 3.14 are determined separately to both the  $x$ - and  $y$ -components of the traction and junction forces.

For nearly all cluster arrangements, the resulting linear system is overdetermined. Analogous to the CPM thermodynamic energy minimization, we assume that the solution to be the minimization of junction force for each cell pair in the cluster, such that  $J_{\sigma, \sigma'}$  terms are calculated as the minimum norm least-squares solution to the linear system (using the MATLAB `lsqminnorm` function).

### 3.2.5 Cell division

We incorporate cell division into the CPM model to reproduce epithelial cell capacity to proliferate and form a confluent monolayer. For simplicity, we assume that if an individual cell area exceeds a minimum area threshold, which we define as  $\frac{2}{3}A_0$ , then individual cells divide with random probability  $q_{divide} = 0.005$ , unless otherwise stated. For cell division, following the prior approach of Daub and Merks, we compute the line of division for each CPM cell as the line following the minor axis, such that each daughter cell is of approximately equally area (177).

Briefly, the cellular inertia tensor approximates the minor and major axis of the cell (Eq. 3.15).

$$I(\sigma) = \begin{pmatrix} \sum_{x \in C(\sigma)} (y - \bar{C}_y(\sigma))^2 & -\sum_{x \in C(\sigma)} (x - \bar{C}_x(\sigma))(y - \bar{C}_y(\sigma)) \\ -\sum_{x \in C(\sigma)} (x - \bar{C}_x(\sigma))(y - \bar{C}_y(\sigma)) & \sum_{x \in C(\sigma)} (x - \bar{C}_x(\sigma))^2 \end{pmatrix}. \quad (3.15)$$

The dividing cell,  $\sigma$ , has lattice points defined by  $C(i) = \{\vec{x} \in \mathbb{Z}^2\}$  and center of mass

$$\bar{C}(i) = \frac{1}{|C(i)|} \sum_{\vec{x} \in C(i)} \vec{x}. \quad (3.16)$$

The division line is therefore the minor axis such that

$$\vec{d} = \bar{C}_y + b(\sigma_{\vec{x}} - \bar{C}_x), \quad (3.17)$$

where  $\bar{C}_y$  and  $\bar{C}_x$  are the  $x$  and  $y$  center of mass, respectively, for dividing cell  $\sigma_{\vec{x}}$ , and  $b$  is the slope of  $\vec{d}$

$$b = \frac{\lambda_b - I_{xx}}{I_{xy}}, \quad (3.18)$$

in which  $\lambda_b = \max |\lambda_I|$ . The lattice sites  $\vec{x}$  of the proliferating cell are then sorted relative to the division line, with half of the cell area assigned to the parent cell  $\sigma$  and half to the daughter cell  $\sigma'$ . The daughter cell inherits the gene expression and phenotype of the parent cell for the purposes of Chapter 4 and is assigned the index  $\sigma' = N_{cell} + 1$ , in which  $N_{cell}$  is the number of cells.

### 3.2.6 Numerical simulations

The CPM map is initialized as uniformly distributed pixels of size 100 x 100, for which each pixel corresponds with a size of 2.5  $\mu\text{m}$ . Initial seeding is dispersed on the cell map excluding the outermost boundary with random probability,  $p = 1/(4A_0)$ . An unloaded finite element mesh of size 101 x 101 forms the nodes of attachment for cells of the CPM map, in which each cell-occupied pixel occupies four nodes such that  $x_{i,j} \rightarrow (x_{i-1,j-1}, x_{i,j-1}, x_{i-1,j}, x_{i,j})$ . To calculate forces from the CPM map, pixels are first mapped to the finite element substrate by identifying the corresponding nodes. At a given instant, the single cell or multicellular geometry is sufficient to define cellular traction forces at each node, using the single or multicellular FMA model, as described above, respectively. The resulting traction forces govern the displacement at each node and determines the strain in the finite element mesh, which in turn is used in evaluating  $H_{durotaxis}$ .

Cell movement consists of copy attempts of randomly selected pixel at each Monte Carlo step (MCS). For each pixel to have equal probability of selection, each MCS has

## CHAPTER 3. CPM

a total of  $10^4$  copy attempts. For each copy attempt, a voxel is selected and randomly perturbed; the sum of interaction energies with each pixel in the Moore neighborhood,  $\sum J(\sigma_{x,x'})$ , determines the  $H_{contact}$  term. Lastly, the cell area before and after the copy attempt provides the  $H_{area}$  term. Together, the net change in the Hamiltonian associated with that copy attempt, i.e.  $\Delta H(\sigma_{x,x'}) = \sum H$ , provides the local energy for the cell before and after the copy attempt. The copy attempt is accepted ( $\sigma_x \rightarrow \sigma'_x$ ) with probability determined by the partition function (Eq. 3.2) for  $\Delta H > 0$  and probability 1 for  $\Delta H < 0$ .

For parameter analysis, the parameter set consisted of each combination of cell-cell interaction energies and cell-matrix interaction energies,  $J_{cc}$  and  $J_{cm}$ , respectively, each repeated with a uniquely seeded random number. The interaction energies were grouped by cell-matrix interaction energy, averaged across each simulation, compared for each ratio of cell-cell to cell-matrix contact inhibition. The confluence is determined by the ratio of total cell occupied pixels to the total grid area. The cell area is number of pixels occupied by each unique cell state, and the cell count is the number of unique states.

### 3.2.7 Cells and reagents

All cells were cultured in a humidified atmosphere at 37 °C with 5% CO<sub>2</sub>. Human MCF10A mammary epithelial cells were obtained from the National Cancer Institute Physical Sciences in Oncology Bioresource Core Facility, in conjunction with American Type Culture Collection (Manassas, VA). MDCK II cells were a gift of Rob Tombes (VCU). MCF10As were maintained under standard culture conditions in DMEM/F-12 HEPES (Life Technologies, Carlsbad, CA), supplemented with 5% horse serum, 0.05%

### CHAPTER 3. CPM

hydrocortisone, 0.01% cholera toxin, 0.1% insulin, 0.02% EGF and 1% antibiotics. MDCK II cells were maintained under standard culture conditions in DMEM (Life Technologies, Carlsbad, CA) supplemented with 10% fetal bovine serum and 1% antibiotics. Purified recombinant active TGF- $\beta$ 1 was purchased from Sigma Aldrich (St. Louis, MO). Immunofluorescence imaging was conducted using the following primary antibodies: Ms anti-Hu E-cadherin (HECD-1, Abcam, Cambridge, United Kingdom), Ms anti-Ms N-cadherin (BD Biosciences, San Jose, CA), Rb anti-Hu FN (Abcam, Cambridge, United Kingdom), Ms anti-Hu LTBP-1 (RD Systems, Minneapolis, MN), Rb anti-Hu Smad2 (86F7, Cell Signaling Technology, Danvers, MA), Dapi (Thermo Fisher Scientific, Waltham, MA). F-actin images were acquired by labeling cells with AlexaFluor555 Phalloidin (Life Technologies, Carlsbad, CA).

#### 3.2.8 Microcontact printing

Microcontact printed square islands were generated as previously described [Tan et al., 2004]. Briefly, 250  $\mu\text{m}$  x 250  $\mu\text{m}$  squares were constructed by generating a negative mold template on a silicon wafer made from an epoxy-type, near-UV photoresist (SU-8; Microchem) using traditional photolithographic techniques. A replica-mold of poly(dimethylsiloxane) (PDMS; Sylgard 184, Fisher Scientific, Hampton, NH) raised patterns were be coated with 100  $\mu\text{g}/\text{ml}$  laminin (Sigma Aldrich, St. Louis, MO) for 2 hours at 37 degree C. Stamps were then rinsed in dH<sub>2</sub>O and dried with nitrogen gas. The laminin square islands were then stamped onto a thin layer of UV-treated PDMS on top of a glass coverslip. 2% Pluronic F-127 in phosphate-buffered saline (PBS) was used to prevent cells from adhering outside of the laminin-stamped areas. Coverslips

were rinsed in PBS prior to cell seeding. Efficiency of protein transfer was confirmed by Immunofluorescence labeling of the ECM protein.

### 3.2.9 Immunofluorescence microscopy

MCF10A and MDCKII cells were plated on microcontact-printed laminin islands at cell densities that resulted in near-confluent monolayers. After 6 hours, samples were rinsed in culture medium to remove non-adherent cells. Cells were cultured for 18 hr and were then transferred to EGF- and serum-free culture conditions for 2 hr to induce an epithelial phenotype. Cells were then incubated with or without TGF- $\beta$ 1 for an additional 48 hours. Cells were permeabilized with 0.5% Triton in 4% paraformaldehyde for 2 minutes, then incubated in 4% paraformaldehyde for 20 minutes. Several PBS-rinses were performed, followed by blocking in 0.1% BSA and labeling with primary antibody for 30 minutes at 37 degree C. Cells were then blocked again in 0.1% BSA and incubated with the appropriate secondary antibody for 30 minutes. Images were acquired on a Zeiss AxioObserver Z1 fluorescence microscope using ZEN2011 software.

### 3.2.10 Cell area and cell number quantification

Cell area and cell number were determined by analyzing immunofluorescence images of F-actin and nuclei via an author-written image processing algorithm in MATLAB. Binary masks of nuclei were generated by thresholding grayscale nucleus images; objects in the binary mask were counted to determine total cell number. To determine cell size, the centroid of each object in the binary mask was determined using the regionprops function. Nuclei centroids were used to generate a Voronoi diagram, which consists of a

series of polygons that have edges that are equidistant from neighboring nuclei. Previous studies have demonstrated that Voronoi diagrams reasonably predict cell boundaries in an epithelial monolayer, and provide a more consistent quantification of cellular size as opposed to quantification of protein markers in the cell-cell junction, whose expression and localization changes as TGF-*beta* dose increases [REF]. Cell area was calculated for each cell by summing the pixels in each Voronoi polygon, and were averaged across the 250  $\mu\text{m}$  x 250  $\mu\text{m}$  colony. Spatial localization of cell number and cell area were determined by binning nucleus centroids into a 5 x 5 grid. Cell counts in each bin were totaled, and cell areas for each bin were averaged if the nuclei centroid was contained within the bin. Spatial localization data was further combined into either corner bins, edge bins, or interior bins, such that there were no overlap between the three regions (i.e., corner bins were not included in the edge region).

### 3.2.11 FRET analysis

To measure force on cell-cell junctions, Fluorescence Resonance Energy Transfer (FRET)-based, full-length E-cadherin tension biosensors were stably transfected into MDCK II cells. Epithelial square islands were cultured as stated above, and images were acquired on a Zeiss LSM 710 laser scanning microscope using ZEN2011 software. Briefly, mTFP (donor) and mEYFP (acceptor) fluorophores were imaged utilizing spectral unmixing at 458 nm excitation. The acquired intensity images were manually masked through ImageJ. Background subtraction and removal of saturated pixels was then performed via an image processing algorithm in Python as previously described (190). FRET ratio was determined by obtaining the acceptor/donor ratio and multiplying with



a binary mask of the junctions. This allowed for inspection of FRET pixels of interest within outlined cell-cell junctions.

### 3.2.12 Statistical analysis

Simulated data was exported to Prism 8 (GraphPad Software Inc) for analysis. Statistical significance, indicated by a p-value less than 0.05, was determined by one-way ANOVA across each TGF- $\beta$  dosage, ratio of interaction energies, and spatial localization.

## 3.3 Results

### 3.3.1 Multicellular traction forces drive formation of epithelial monolayers

Prior studies from van Oers, et al demonstrated that a hybrid CPM-FEM model can predict cellular spreading and organization based on cell-generated traction forces, resulting strains in the substrate, and duratactic driven migration in the CPM. To expand this model to adherent cell monolayers, we incorporated several advancements: first, cellular traction forces were predicted from the FMA model (186) based on a cell cluster geometry, not on individual cells. As such, cells in contact with neighboring cells “adhere” and begin to generate traction forces as a cohesive unit. Second, we assume that each cell in a multicellular cluster still maintains a static equilibrium, as has been suggested previously (191). As such, we require the force acting on cell-cell junctions to

counter the net traction force for each cell, as illustrated in a simple two cell example (Fig. 3.1 C, left).

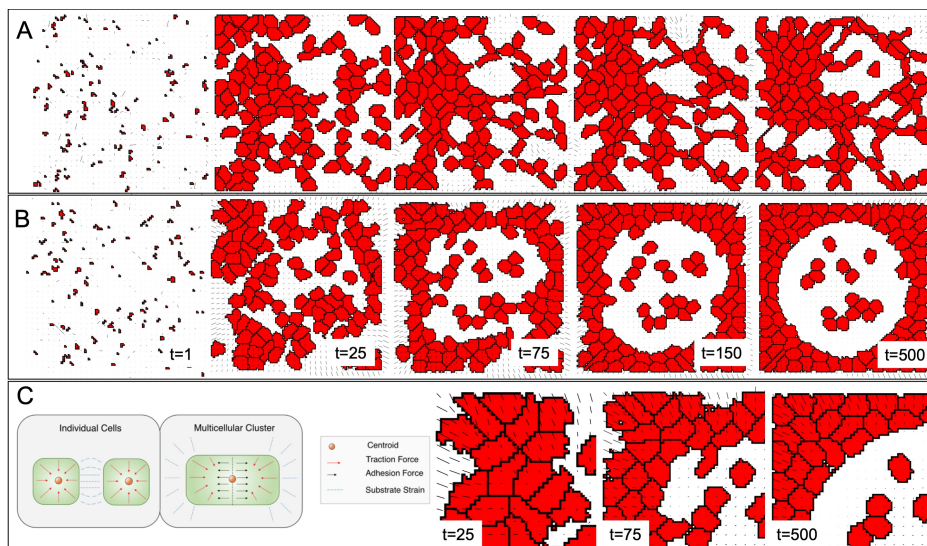


**Figure 3.1.** Simulated cells (red pixels) migrate on a finite element substrate that responds to cell-generated traction forces. Traction forces are calculated based on either (A) individual cell geometries or (B) multicellular clusters. (C, left) Representation of traction forces with resulting strain for multicellular geometries, and (C, right) inset of time points from panel B.

Figure 3.1 depicts simulated cells (red pixels) with corresponding scaled substrate strains (black vectors) for two scenarios. In the first, traction force is calculated from the FMA about the single cell geometry and each cell is in static equilibrium. As a result, the net imbalance for each cell is zero and no force is transferred across the cell-cell junction (Fig. 3.1 A). In the second scenario, traction force is calculated from FMA about the multicellular geometry and each *cluster* is in static equilibrium (Fig. 3.1 B). The net force imbalance for each cell is balanced by the intercellular tension, which transfers the traction force to neighboring cells. Without redistribution of cytoskeletal

stress to neighboring cells across cell-cell junctions, cellular alignment is localized and multicellular structures behave as partially cooperative networks with discordant substrate strains (Fig. 3.1 A, S1 Video), as demonstrated by van Oers et al (174). In contrast, traction force distribution across cell-cell junctions to neighboring cells results in highly cooperative networks with a uniform spatial gradient of substrate strains. The formation of these cohesive multicellular clusters resembles an epithelial monolayer with preferential localization towards the boundary (Fig. 3.1B, S2 Video). In the resulting multicellular clusters, net traction forces have a magnitude and direction at any given point proportional to the FMA about that point in the cluster, resulting in a linear gradient of substrate strain oriented radially towards the cluster centroid (Fig. 3.1C, S2 Figure).

### 3.3.2 Spatiotemporal dynamics of monolayer confluence

Preliminary simulations demonstrated the formation of a subconfluent monolayer-like sheet, which alters the spatial distribution of monolayer stress. To better predict the spatiotemporal dynamics of an *in vitro* epithelial monolayer, we incorporated cellular proliferation into the CPM to account for cell division dynamics, and then compared the spatiotemporal dynamics with cultured epithelial cells (Fig. 3.2, S2 Figure; see Methods for a more in-depth discussion). Mammary breast epithelial cells (MCF10A) were seeded onto microfabricated PDMS substrates with a  $250\ \mu\text{m} \times 250\ \mu\text{m}$  microcontact-printed area of laminin (Fig. 3.2A). Epithelial monolayers reached confluence over approximately 24 hours. Simulated cells exhibit similar patterning representative of MCF10A confluence dynamics (Fig. 3.2B). To estimate the rate of proliferation in the simulations,

immunofluorescence images were analyzed at 0, 6, 12, 18, and 24 hours and quantified for confluence as a function of time (Fig. 3.2C, S3 Video). The half maximal confluence for simulations and experiments indicate that 75 Monte Carlo steps (MCS) corresponds to 6 hours of experimental time (Fig. 3.2B, C). This was used to estimate a simulated division probability of 0.5% per time step. These results demonstrate that simulated spatiotemporal dynamics approximate cellular dynamics observed *in vitro* and agree with previous studies (192).

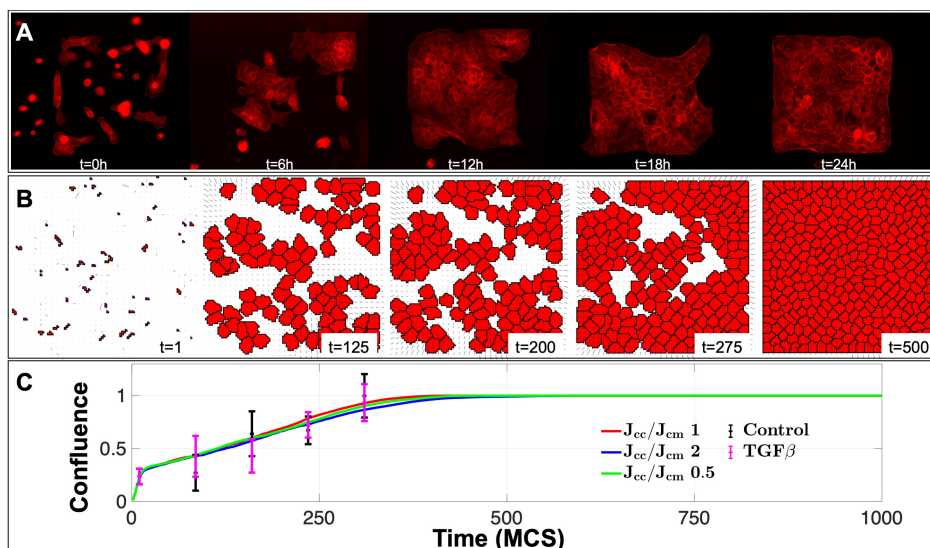


**Figure 3.2.** Spatiotemporal dynamics of simulated and *in vitro* tissue patterning. Visual comparison of time points from initial seeding to confluence illustrates parallels between (A) *in vitro* and (B) simulated spatial patterns. (C) Confluence, the fraction of total cell area to total substrate area, is shown as a function of time or Monte Carlo Steps (MCS), for *in vitro* and *in silico* experiments, for different conditions. Other parameters: Time scale: 4.8 min/1 MCS,  $J_{cm} = 2.5$ .

### 3.3.3 Altered interfacial energies mimic changes in contact inhibition

With the key addition that traction forces are governed by the FMA model about the cluster geometry rather than the single cell geometry, the previous results illustrate distinct spatial patterning representative of epithelial monolayers. We next utilized our model to simulate epithelial monolayer and associated EMT-like dynamics. One key aspect of the epithelial phenotype is contact inhibition: that is, the propensity of a cell to stop migration and proliferation when a neighboring cell is encountered (193; 194). As epithelial cells undergo EMT and become more mesenchymal, contact inhibition is reduced (195). To mimic the effects of EMT in epithelial monolayers in our multicellular FMA model, we varied the relative interaction energies between neighboring cells in the CPM, which simulates changes in contact inhibition. We varied the ratio of interaction energies at the cell-cell and cell-matrix interfaces,  $J_{cc}$  and  $J_{cm}$ , respectively (see Materials and Methods, Eq 3.4), for the single cell (Fig. 3.3A–D) and multicellular (Fig. 3.3E–H) FMA models. The magnitude of the respective energies represents a prohibitive interaction, i.e., a higher  $J_{cc}/J_{cm}$  ratio reflects increased contact inhibition between adjacent cells. For each simulation, we measured the steady-state monolayer confluence, average cell area, total cell count, and relative net cellular traction forces, averaged over 5 simulations with distinct random cell seeding, and plotted these measures as a function of the  $J_{cc}/J_{cm}$  ratio. These simulations were then repeated for 3 distinct values of cell-matrix interaction energies,  $J_{cm}$ .

Results indicate similar trends between the single cell and multicellular FMA models, with the exception of net cellular traction force, which must be zero for a

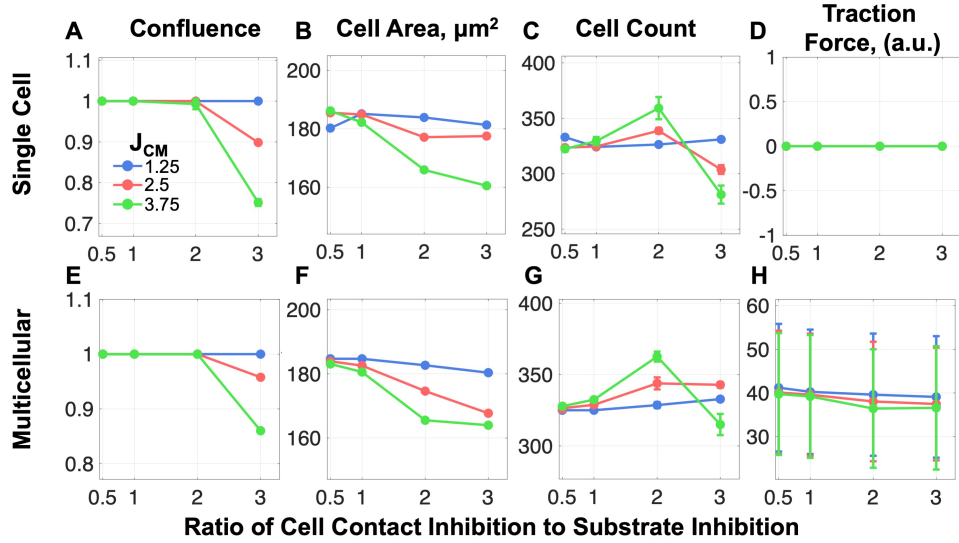


**Figure 3.3.** Parameter sweep of interaction energies. (A-D) Single cell FMA and (E-H) multicellular FMA simulated confluence, cell area, cell count, and traction force, shown as a function of the ratio of cell-cell contact inhibition to cell-matrix inhibition ( $J_{cc}/J_{cm}$ ), varying  $J_{cm}$  values.

cell in static equilibrium in the single cell FMA model (Fig. 3.3D). Beyond a critical point ( $J_{cc}/J_{cm} = 2$ ), high cell contact inhibition precludes the formation of confluent monolayers (Fig. 3.3A, E). Further, we find that the time course of monolayer confluence only weakly depends on cell contact inhibition below this critical point, i.e. for conditions that form confluent monolayers (Fig. 3.2C). Similarly, increasing cell contact inhibition results in smaller cell area (Fig. 3.3B, F) and higher cell count (Fig. 3.3C, G). In the multicellular FMA model, net traction force per cell decreases as the  $J_{cc}/J_{cm}$  ratio increases. We find that higher substrate inhibition, i.e., increased  $J_{cm}$ , tends to increase the sensitivity to the  $J_{cc}/J_{cm}$  ratio for all measures. Thus, these data indicate that a loss of contact inhibition leads to larger cells, lower cell count, and in extreme cases, loss of confluence.

### 3.3.4 Decreasing contact inhibition increases cell size and decreases cell number

The above results suggest that cells in the multicellular FMA model resemble the archetypal phenotype of epithelial cells undergoing EMT. With decreased cell-cell contact inhibition (i.e., smaller  $J_{cc}/J_{cm}$  ratio), simulated cells exhibit the characteristic increased spreading and decreased proliferation of the mesenchymal phenotype, while at increased cell-cell contact inhibition (i.e., larger  $J_{cc}/J_{cm}$  ratio), simulated cells exhibit decreased spreading and increased proliferation characteristic of the epithelial phenotype. Together, these results indicate that this parameter may serve as a suitable comparison to *in vitro* models of growth factor induced EMT. We thus compared these results to experiments in which EMT was induced by the soluble growth factor TGF- $\beta$ , as has previously been detailed (44). Representative immunofluorescence images of MCF10A cells treated with increasing dosages of TGF- $\beta$  illustrate a phenotypic switch from cortical actin, which is typically observed in epithelial cells, to pronounced actin stress fibers associated with the mesenchymal phenotype (Fig. 3.4A). In these confluent monolayers, MCF10A average cell count decreases and average cell area increases for increase TGF- $\beta$  doses (Fig. 3.4B, D). As in Fig. 3.3, we observe similar trends in simulations for decreasing cell contact inhibition, although with a weaker dependence than observed *in vitro* (Fig. 3.4C, E). Thus, we find that cell contact inhibition similarly regulates the cellular geometry averaged over the confluent monolayer in both simulation and experiment.

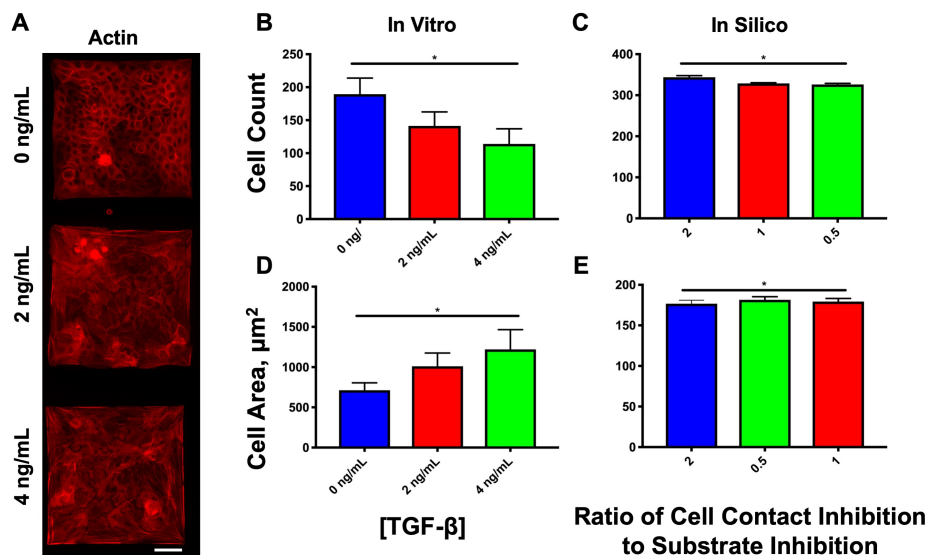


**Figure 3.4.** Morphological characterization of the epithelial phenotype with TGF- $\beta$ -induced EMT. (A) Representative immunofluorescent images of experimental illustrate a confluent MCF10A monolayer bounded to the  $250 \times 250 \mu\text{m}$  microfabricated square; scale bar =  $50 \mu\text{m}$ . *In vitro* (B, D) and simulated (C, E) average cell count and cell area for the confined geometry are shown for each TGF- $\beta$  dosage and ratio of contact interaction energies, respectively. Sample size  $n=3$  for *in vitro* experiments. \* with line denotes significance between each TGF- $\beta$  dosage or each contact energy ratio.

### 3.3.5 Cell-cell junction force maintains mechanical equilibrium of multicellular clusters

A key advance of the multicellular FMA model is the prediction of forces acting on cell-cell junctions. By assuming static equilibrium and applying a force-balance principle, cell-cell junction force was predicted as a reaction force that balances traction forces of the monolayer (described in detail in Methods). Cell-cell junction force magnitudes are shown on the boundaries between neighboring cells in simulated monolayers (Fig. 3.5D). To examine spatial trends, we segmented the simulation domain into a  $5 \times 5$  grid of



bins, and calculated the mean junction force magnitude within each bin (Fig. 3.5E). The spatial distribution of junction forces is pronounced, with the largest forces in the interior and smallest in the corners (Fig. 3.5F). However, interestingly, we find minimal variation in the spatial trends between low, medium, and high contact inhibition ratios.

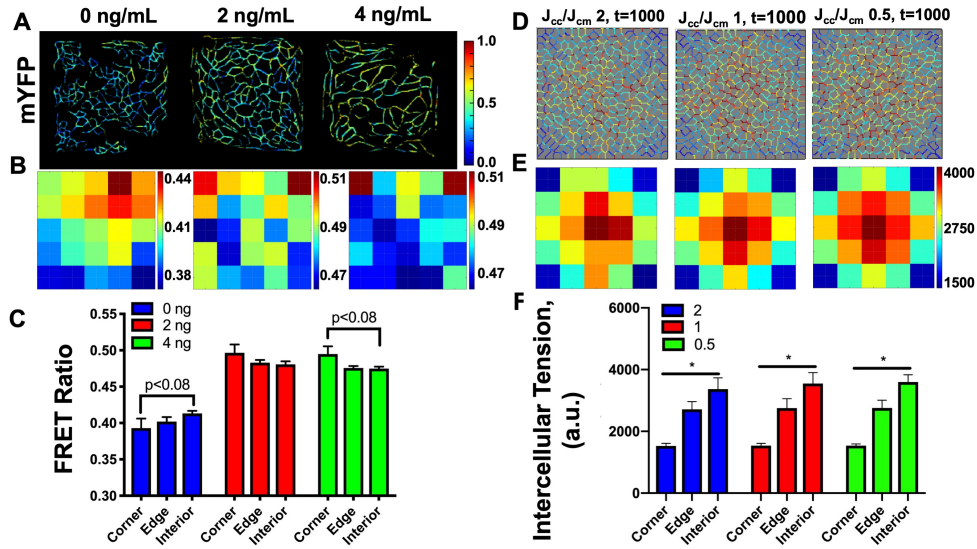


**Figure 3.5.** Intercellular interaction energy reflects TGF- $\beta$  effects *in vitro*. (A) *In vitro* FRET intensities in MDCK II cells. (B) Corresponding heatmaps for average FRET intensities are binned into a 5 x 5 grid, and (C) their associated bar graphs averaged at the corners, edges, and interior for 0, 2, and 4 ng/mL TGF- $\beta$  dosages;  $n=3$ . (D) Simulated intercellular tension is depicted as the net magnitude for high, medium, and low interaction energy ratios. (E) Intercellular tension magnitudes are shown as a 5 x 5 grid with (F) their associated bar graphs averaged at the corners, edges, and interior;  $n=5$ , \* with line denotes significance between each location.

We next sought to compare these with experimentally-measured junction forces. To measure cell-cell junction forces experimentally, Madin-Darby Canine Kidney Cells (MDCKII) cells were stably transfected with a full-length E-cadherin force sensor, as

previously described (196). Briefly, the force sensor consists of two fluorophores coupled by a polypeptide that exhibits elasticity. The two fluorophores are designed such that, when in close proximity, the pair exhibits Forster Resonance Energy Transfer (FRET): that is, emission light from the first fluorophore is absorbed by the second fluorophore, which emits light. As the sensor is stretched and the fluorophore pair moves apart, the excitation of the second fluorophore by the first fluorophore decays, resulting in a loss of FRET excitation relative to excitation of the first fluorophore. This force sensor was inserted into E-Cadherin, which comprises the homophilic binding event in cell-cell junctions known as adherens junctions. Validation and functionality of this sensor has been previously demonstrated (197; 198). EMT was again induced by increasing dosage of (TGF- $\beta$ ) (Fig. 3.5A). FRET ratio reflects the energy transfer between the two fluorophores, in which FRET ratio is inversely proportional to tension on the FRET force sensor: high FRET ratio indicates low tension and low FRET ratio indicates high tension. Representative pseudocolored images of the processed FRET ratio are shown in Fig. 3.5A. We next investigated if spatial patterns of junction forces were established in these confluent monolayers. We again segmented images of the the local net FRET ratios into a 5 x 5 grid. In the absence of TGF- $\beta$ , colonies illustrated a nearly spatially uniform low FRET ratio, indicating high cell-cell tension throughout the monolayer (Fig. 3.5B). TGF- $\beta$  treatment increased FRET ratio, indicating a drop in overall tension. Additionally, a small spatial gradient was established, with higher FRET ratios (lower cell-cell tension) in the corner and edges and lower FRET ratios (higher cell-cell tension) in the interior of the monolayer, consistent with a spatial gradient of larger junction forces in the center and decreasing towards the edges and corners (Fig. 3.5C).

Together, these data indicate that simulated spatial gradients of cell-cell junction force are best suited for comparison to experimental measures of TGF- $\beta$ -treated colonies. Furthermore, simulated cell-cell junction forces predict a spatial trend of decaying cell-cell tension from interior to periphery.

### 3.3.6 Individual cell geometry spatial patterns

Summarizing our results presented thus far, we found that the multicellular FMA model reproduces contact inhibition-dependent trends for average cellular geometry (i.e., cell size and count), but underestimates this dependence compared with experimental observations. Further, our model qualitatively predicts trends for spatial patterns of cell-cell junction forces in TGF- $\beta$ -treated monolayers, but overestimates the magnitude of the spatial gradient, in comparison with experiments. We hypothesize that these discrepancies arise from an underestimation of cell size distribution throughout the monolayer in response to changes in contact inhibition. That is, individual cell size changes in response to TGF- $\beta$  treatment due not only to loss of cell contact inhibition, but also to additional signaling not currently present in our model. To investigate this, we again segmented immunofluorescence images of MCF10A cells and binned cell area as before into a 5 x 5 grid (Fig. 3.6 A). Consistent with overall monolayer averages, cell area increased with increasing TGF- $\beta$  dose. Evaluating the average cell area in the corner, edge, and interior of the monolayer reveals an overall increase in cell area at the periphery of the square, with the largest cell area localized to the corners in both low and high TGF- $\beta$  dosages (Fig. 3.6 A). Reduced contact inhibition by treatment with TGF- $\beta$  accentuates this trend, resulting in a large spatial gradient in cell area (Fig. 3.6 B). In

contrast, simulated cell area exhibited substantially reduced spatial variation compared to experimental cell area (Fig. 3.6 C). Furthermore, the effects of contact inhibition had a relatively minimal effect on spatial variation of cell area, resulting in slightly increased cell area at the monolayer interior (Fig. 3.6 D). Thus, the lack of accounting for heterogeneous cellular properties, specifically cell area, is a key limitation of our model. Since cells undergo profound phenotypic changes throughout EMT, it would be reasonable that these changes lead to parameter changes within the CPM for each individual cell; incorporating these changes in cell phenotype into the CPM component is a primary future goal for the model development.

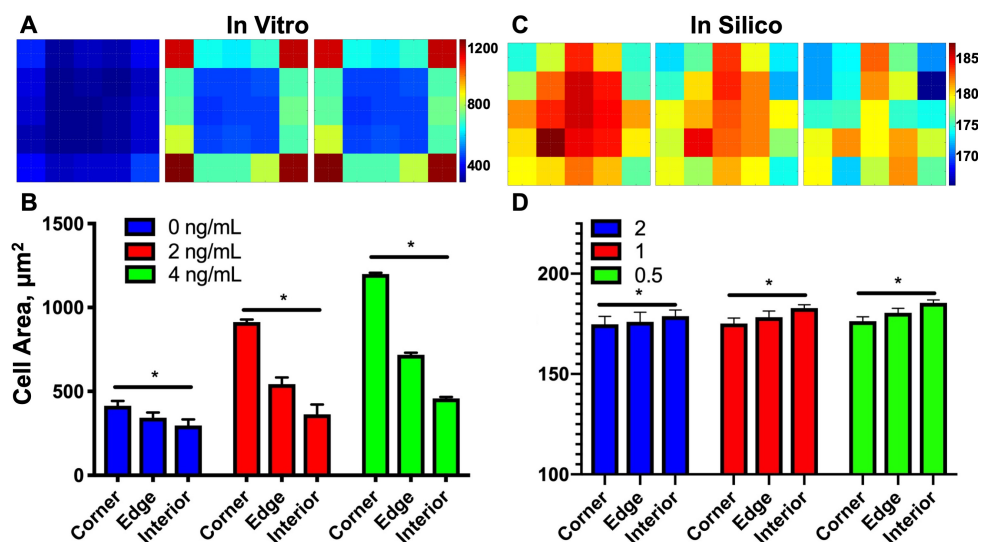


**Figure 3.6.** Individual cell geometry spatial patterns (A) *In vitro* heatmaps for binned cell area treated with 0, 2, and 4 ng/mL TGF- $\beta$  and (B) their associated bar graphs for average corner, edge, and interior;  $n=3$ . (C) Simulated heatmaps for binned cell area at high, medium, and low contact inhibition and (D) their associated bar graphs;  $n=5$ .

**One-dimensional model of junction force distribution**

It is instructive to consider junction forces in a simple one-dimensional geometry, to both illustrate our approach and explain the perhaps counterintuitive prediction that larger traction forces at the periphery result in larger junction forces at the center. For this simple geometry, the traction and junction force magnitudes can be solved analytically, and further, these analytical results provide an explanation for some of the discrepancies between experiments and simulations noted above.

Consider a linear array of  $2n$  cells of length  $L$  that are arranged and coupled in a line, such that the cell junctions are located at positions  $(-nL, 0), (-(n+1)L, 0), \dots, (0, 0), \dots, ((n-1)L, 0), (nL, 0)$  where  $T = nL$  is the length of half of the monolayer or tissue (Fig. 3.7C). Note that the  $y$  position is insignificant, since all forces are oriented in the  $x$ -direction. The centroid of the tissue aligns with the origin,  $(0, 0)$ , which is the junction on the left edge of cell 1, and thus the net traction force in each cell will be pointed towards this position. Further, we assume that each cell has  $f$  focal adhesions, uniformly spaced along the length of the cell  $L$ , and that traction forces are generated only at the focal adhesion positions. In the illustrated example,  $f = 4$ .

Traction forces generated at each focal adhesion are thus proportional to distance from the origin, and the net traction force for a given cell is the sum of all traction forces over all focal adhesions. We can show that for cell  $k$ , with left edge at position  $((k-1)L, 0)$  and right edge at position  $(kL, 0)$ , the net traction force is given by  $\vec{T}_k = (-\mu L f (k - \frac{1}{2}), 0)$ , where  $\mu$  is the appropriate scaling factor. For the rightmost cell, cell  $n$ ,  $\vec{T}_n = (-\mu L f (n - \frac{1}{2}), 0)$ . For mechanical equilibrium at cell  $n$ , this traction force must be balanced by the junction force from cell  $n-1$  to cell  $n$ , such that

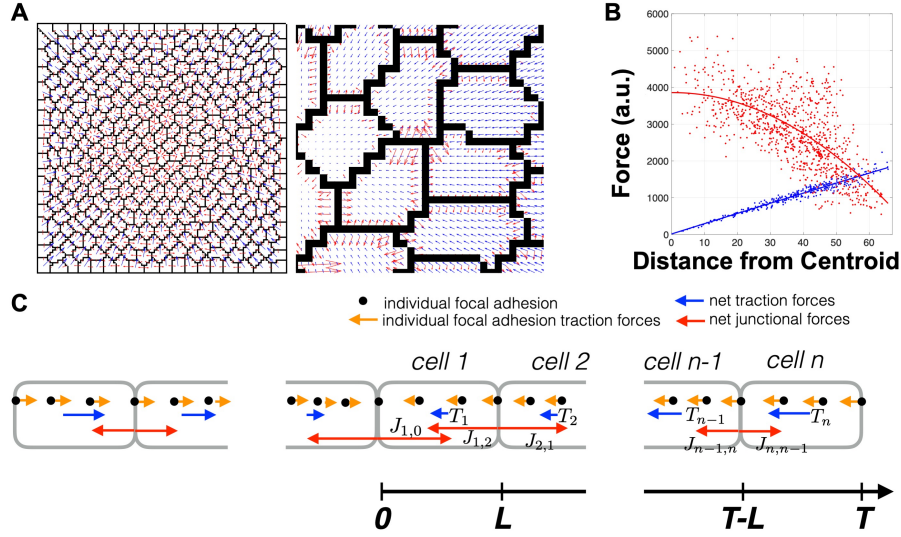


**Figure 3.7.** One-dimensional generalization for multicellular forces at mechanical equilibrium. (A) Representative snapshot of the traction and junction forces in the multicellular CPM model. (B) Plots of the traction and junction forces from the CPM simulations shows that traction force scales linearly with distance from monolayer centroid (blue line) and intercellular tension drops off quadratically from the centroid (red line).

$\vec{J}_{n,n-1} = (\mu L f(n - \frac{1}{2}), 0)$ . By assumption, net forces at the cell-cell junction are also in equilibrium, such that junction force pairs are symmetric, i.e., equal in magnitude and opposite in direction, such that  $\vec{J}_{n-1,n} = (-\mu L f(n - \frac{1}{2}), 0)$ .

Next considering forces on cell  $n - 1$ , the junction force from cell  $n - 2$  to cell  $n - 1$  must balance both the net traction force  $\vec{T}_{n-1} = (-\mu L f((n - 1) - \frac{1}{2}), 0)$  and junction force  $\vec{J}_{n-1,n}$ , such that  $\vec{J}_{n-1,n-2} = (\mu L f(2n - 2), 0)$ . Similarly, junction force from cell  $n - 3$  to cell  $n - 2$ ,  $\vec{J}_{n-2,n-3} = (\mu L f(3n - \frac{9}{2}), 0)$ . In general, we can show that the intercellular tension from cell  $k$  to  $k + 1$ ,

$$\vec{J}_{k+1,k} = \left( \frac{1}{2}(n^2 - k^2)\mu Lf, 0 \right) = \left( \frac{1}{2}\mu f \left( \frac{T^2}{L} - Lk^2 \right), 0 \right). \quad (3.19)$$

Thus, the junction force at the center onto the left edge of cell 1,  $\vec{J}_{1,0} = (\mu L n^2 f / 2, 0) = (\mu T^2 f / (2L), 0)$ . This simple geometry arrangement predicts larger magnitude junction forces in the center, and further illustrates a quadratic drop-off (due to the  $-k^2$  term in the magnitude of  $\vec{J}_{k+1,k}$ ) that is predicted as junction position  $k$  increases towards the periphery. A representative example of the CPM model illustrates the distribution of traction forces (blue) and junction forces (red) in a confluent monolayer (Fig. 3.7B) and both the linear increase in traction force magnitude from the monolayer centroid and the quadratic drop-off in junction force magnitude (Fig. 3.7B).

Thus, for a monolayer of a given size, i.e., fixed  $T$ , Eq 3.19 predicts that for a smaller cell size (decreased  $L$  and thus increased  $n$ ), the magnitude of junction forces are larger throughout the monolayer, which is consistent with experimental measurements of lower FRET ratios (i.e., higher tension) in non-treated epithelial monolayers (Fig. 3.5C). Further, in TGF- $\beta$ -treated monolayers, more mesenchymal-like larger cells at the monolayer periphery would be expected to have more focal adhesions per cell, in contrast with epithelial-like smaller cells in the interior. Additionally, while larger cells at the periphery will reduce junction forces locally, due to the cumulative nature of junction forces required to maintain mechanical equilibrium originating at the periphery, this local reduction in junction forces would be expected to have a greater influence on interior junction forces. All of these considerations would be predicted to reduce the magnitude of the spatial gradient, consistent with smaller spatial gradients observed experimentally.

### CHAPTER 3. CPM

We can further generalize this example and consider the continuous limit in the spatial dimension, in which the traction forces in the  $x$ -direction at position  $x$  are given

$$T(x) = -\mu f(x)x, \quad (3.20)$$

where  $f(x)$  is the spatial distribution of focal adhesions per unit length. Junction forces at position  $x$  are then by definition the *second moment of area*, evaluated from the cluster periphery to position  $x$ , where again  $x = 0$  corresponds with the cluster center,

$$J(x) = -\mu \int_T^x f(x')x'dx'. \quad (3.21)$$

For uniform focal adhesion distribution,  $f(x) = f/L$ , we can integrate Eq 3.20, and using  $x = kL$ , the result is equivalent to Eq 3.19.

Although the CPM predictions of force spatial distributions generally agree with previous findings, characteristics of the monolayer do not fully capture monolayer dynamics observed *in vitro*. In particular, trends in cell area and count are not well represented in variations of contact penalties for the CPM. While TGF- $\beta$  is known to increase cell spreading, the CPM uniformly constrains cell area to a target area. By varying the target area in future iterations, the CPM would better capture capture the effects of EMT on cell area and resulting spatial patterning.



# Chapter 4

## Gene regulation of the epithelial-mesenchymal program

### 4.1 Introduction

A prevalent EMT regulatory network involves a group of master transcription factors with micro-RNA counterparts that facilitate a switch between cell-cell and cell-substrate adhesion (178; 179; 180; 183; 184). Previous experimental and computational work has developed and characterized an EMT-associated signaling network capable of regulating key epithelial and mesenchymal adhesion molecules (42; 181). Consisting of the EMT-TFs SNAIL1 and ZEB1 and microRNAs miR-34 and miR-200, the network regulates the epithelial marker, E-cadherin, and mesenchymal marker, N-cadherin (Fig. 4.1). Characterizing the gene regulatory function of the EMT-TFs in the context of EMT-associated features will improve our understanding of phenotype states in

the EMT spectrum, as well as present opportunities for therapeutics targeted at EMT-TFs (182; 183; 184).

The Tian model, also referred to as the cascading bistable switch (CBS) model, provides an intracellular signaling framework appropriate for the application of phenotype tracking in a heterogeneous cell population. This EMT-GRN has a temporal and dosage-dependent response to exogenous TGF- $\beta$ , which produces a latent intermediate mesenchymal phenotype capable of reversion to an epithelial phenotype Fig. 4.2. Firstly, introduction of TGF- $\beta$  at particular thresholds drives the EMT-GRN in favor of the mesenchymal phenotype. Secondly, we may substitute a separate perturbation, which stems from cell-cell junctions, as an input to the intracellular regulatory network with similar dynamics to TGF- $\beta$ .

Loss of force across E-cadherin junctions transitions epithelial cells to a reversible intermediate mesenchymal phenotype. Destabilizing the regulatory network with exogenous perturbations sufficiently drives EMT to an irreversible mesenchymal phenotype. In Chapter 4, we propose that the GRN is susceptible to mechanical perturbation from intercellular tension, and introduce transduction of junctional forces to intracellular signaling cascades as a mechanism for inducing EMT.

To address the discrepancies in experimental and computational observations described in Chapter 3 we defined phenotype cellular properties which are regulated by an EMT-associated gene regulatory network. First, we integrated the computational framework established in Chapter 3 with an intracellular signaling network that regulates well-characterized epithelial and mesenchymal genes. Next, we coupled mechanical feedback at cell-cell junctions to a molecular signaling pathway, i.e.  $\beta$ -catenin, associated

with loss or gain of cell-cell junctions to further understand how the intracellular signaling network generates EMT-associated features (199; 200). Key findings will provide feedback to the larger computational framework by predicting phenotype heterogeneity due to complementary dynamics at the molecular and cellular scale throughout the EMT program. A particularly interesting application of this multiscale approach is tracking of the spatiotemporal progression of phenotypic states in an epithelial monolayer.

## 4.2 Methods

Phenotype-specific properties associated with EMT reflect a switch in cellular motility. Morphological changes arising from EMT necessarily change the thermodynamic behavior of a cell: mesenchymal cells have larger volumes, decreased cell-cell adhesion, and larger traction forces (201). Hence, the Hamiltonian terms of Eq. 3.1 are unique to each phenotype. For this reason, the phenotypic state of each cell must be known prior to calculating the Hamiltonian term.

To understand how the cadherin GRN contributes to EMT, we coupled mechanical feedback at cell-cell junctions to molecular signaling known to be linked with loss or gain of cell-cell junctions. Gene expression was tracked for each cell cell and will be useful in later studies to predict localized regions of EMT. In doing so, we were able to assign phenotype associated behavior on a cell-by-cell basis. Additionally, these findings will be useful in simulating secretion of EMT biomarkers that contribute to aberrant EMT in an autocrine and paracrine fashion.

### 4.2.1 Gene regulatory Network

The EMT-GRN of the CBS model consists of two double negative feedback loops, comprised of transcription factors and miRNA, which act on the epithelial gene for E-cadherin and mesenchymal gene for N-cadherin (Fig. 4.1). TGF- $\beta$  initiates EMT through upregulation of mRNA for transcription factor SNAIL1 (*snail1*). However, miR-34 represses translation of mRNA *snail1* to SNAIL1, which in turn inhibits miR-34 in a negative feedback loop. The second negative feedback loop reflects the first, but comprised of mRNA *zeb* producing transcription factor ZEB and inhibition by miR-200. Both feedback loops downregulate the epithelial gene and upregulated the mesenchymal gene.

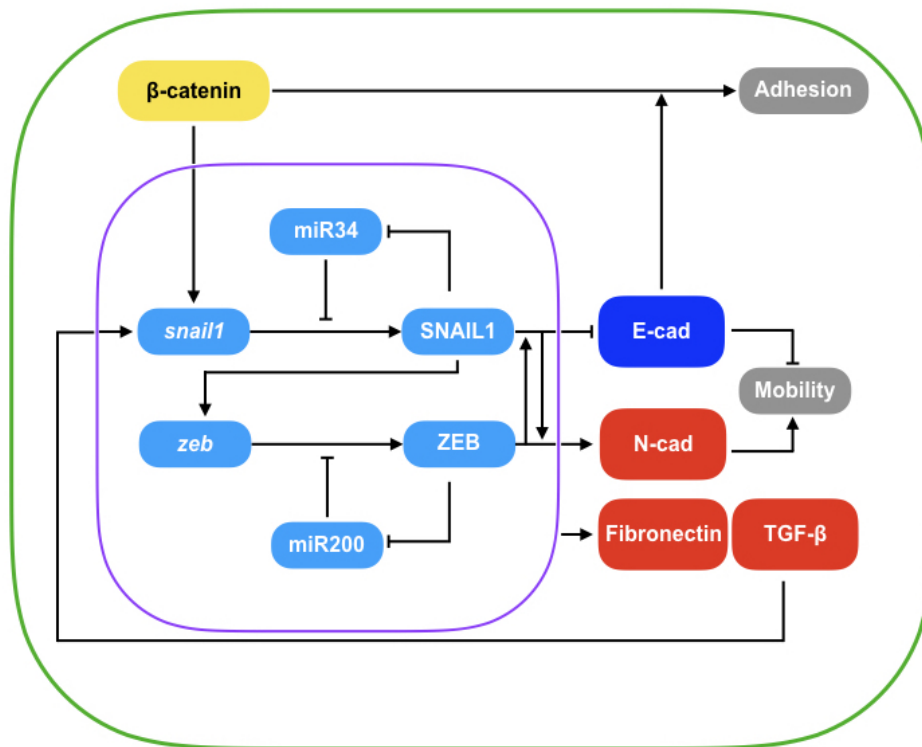


**Figure 4.1.** Schematic of the EMT gene regulatory network dynamics. Exogenous TGF- $\beta$  initiates the gene regulatory network to downregulate E-cadherin and upregulate N-cadherin. TGF- $\beta$  is also an output of the network, which acts in a positive feedback loop.

The sensitivity to exogenous TGF- $\beta$  stimulates a partial mesenchymal phenotype at intermittent exposure and mid-range concentrations (Fig. 4.2). Endogenous production of TGF- $\beta$  can form a self-sustaining feedback loop if exogenous TGF- $\beta$  is either persistently applied or the concentration is sufficiently large surpasses, resulting in an irreversible mesenchymal phenotype.

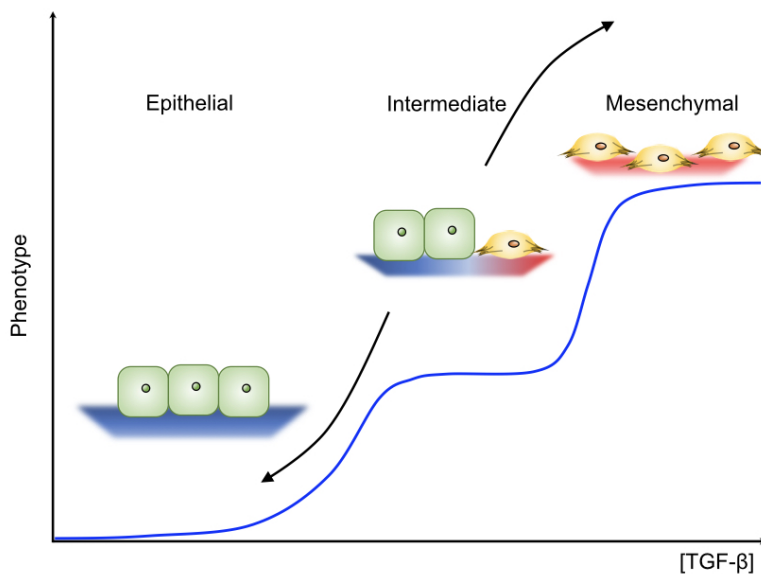


**Figure 4.2.** Representation of the phenotype bistable switch predicted by the Tian model. Epithelial cells (shown in green) exist upstream of the first switch, saddle node 1 (SN1), wherein exogenous TGF- $\beta$  dose and exposure time are minimal. The reversible intermediate mesenchymal phenotype (shown in yellow) is located between SN1 and SN2. Lastly, the irreversible mesenchymal phenotype is shown downstream of SN2 where exogenous TGF- $\beta$  concentrations are maintained for sustained periods, whether through repeated exposure or high dosage.

The EMT-GRN represented schematically in Fig. 4.1 was described using a system of ordinary differential equations (ODEs) with each variable having Hill function-like dynamics. All terms are for endogenous concentrations, and exogenous TGF- $\beta$  was simulated at a constant value of 3 nM.

$$\frac{d[T]}{dt} = k0_T + k_T \frac{1}{1 + \frac{[R2]^n}{J_T r_2}} - kd_T[T], \quad (4.1)$$

$$\frac{d[s]}{dt} = k0_s + k_s \frac{\frac{[T]+TGF_0^{nt}}{J_s}}{1 + \frac{[T]+TGF_0^{nt}}{J_s}} - kd_s[s], \quad (4.2)$$

$$\frac{d[S]}{dt} = k_s[s] \frac{1}{1 + \frac{[R3]^{nr_3}}{J_S}} - kd_S[S], \quad (4.3)$$

$$\frac{d[z]}{dt} = k0_z + k_z \frac{\frac{[S]^{n_s}}{J_z}}{1 + \frac{[S]^{n_s}}{J_z}} - kd_z[z], \quad (4.4)$$

$$\frac{d[Z]}{dt} = k_Z[z] \frac{1}{1 + \frac{[R2]^{nr_2}}{J_Z}} - kd_Z[Z], \quad (4.5)$$

$$\frac{d[R2]}{dt} = k0_2 + k_2 \frac{1}{1 + \frac{[S]^{n_s}}{J_{1_2}} + \frac{[Z]^{n_z}}{J_{2_2}}} - kd_2[R2], \quad (4.6)$$

$$\frac{d[R3]}{dt} = k0_3 + k_3 \frac{1}{1 + \frac{[S]^{n_s}}{J_{1_3}} + \frac{[Z]^{n_z}}{J_{2_3}}} - kd_3[R3], \quad (4.7)$$

$$\frac{d[E]}{dt} = k_{e1} \frac{1}{\frac{[S]^{n_s}}{J_{1_e}} + 1} + k_{e2} \frac{1}{\frac{[Z]^{n_z}}{J_{2_e}} + 1} - kd_e[E], \quad (4.8)$$

$$\frac{d[N]}{dt} = k_{n1} \frac{\frac{[S]^{n_s}}{J_{1_n}}}{\frac{[S]^{n_s}}{J_{1_n}} + 1} + k_{n2} \frac{\frac{[Z]^{n_z}}{J_{2_n}}}{\frac{[Z]^{n_z}}{J_{2_n}} + 1} - kd_n[N], \quad (4.9)$$

where [T], [s], [S], [z], [Z], [R2], [R3], [E], and [N] denote endogenous TGF-beta, *snail*, SNAIL, *zeb*, ZEB, *miR-200*, *miR-34*, E-cadherin, and N-cadherin, respectively.

| Parameter          | Symbol | Value |
|--------------------|--------|-------|
| TGF- $\beta$       | [T]    | 0.16  |
| <i>snail1</i> mRNA | [s]    | 0.01  |
| SNAIL1             | [S]    | 0.01  |
| miR-34             | [R3]   | 0.38  |
| <i>zeb</i> mRNA    | [z]    | 0.03  |
| ZEB                | [Z]    | 0.01  |
| miR-200            | [R2]   | 0.35  |
| E-cadherin         | [E]    | 3.20  |
| N-cadherin         | [N]    | 0     |

**Table 4.1.:** State variables are shown for the system described in Eq. 4.1–4.9.

The output for the EMT-associated gene regulatory network is shown Fig. 4.3. A constant input of exogenous TGF- $\beta$  was applied and gene expression was tracked for a simulated time of 18.75 days. The deterministic solution reveals two stable states with an intermediate state, indicated by partial expression of the epithelial gene and mesenchymal gene. Low expression of endogenous TGF- $\beta$  corresponds to an intermediate phenotype in which the epithelial marker is partially downregulated and the mesenchymal marker is partially upregulated. An increase in endogenous TGF- $\beta$  after persistent stimulation by exogenous TGF- $\beta$  drives the phenotype towards an irreversible mesenchymal phenotype.

### 4.2.2 $\beta$ -catenin signaling

Mechanical induction of the EMT-TFs occurs during destabilization of cell-cell adhesions: the cytoplasmic domain of E-cadherin is cleaved, releasing  $\beta$ -catenin for either degradation or nuclear translocation to activate EMT-TFs SNAIL1 and ZEB (44; 202). Therefore, the  $\beta$ -catenin signaling cascade provides a mechanotransduction pathway for coupling junction force at the E-cadherin complex to the EMT-GRN.



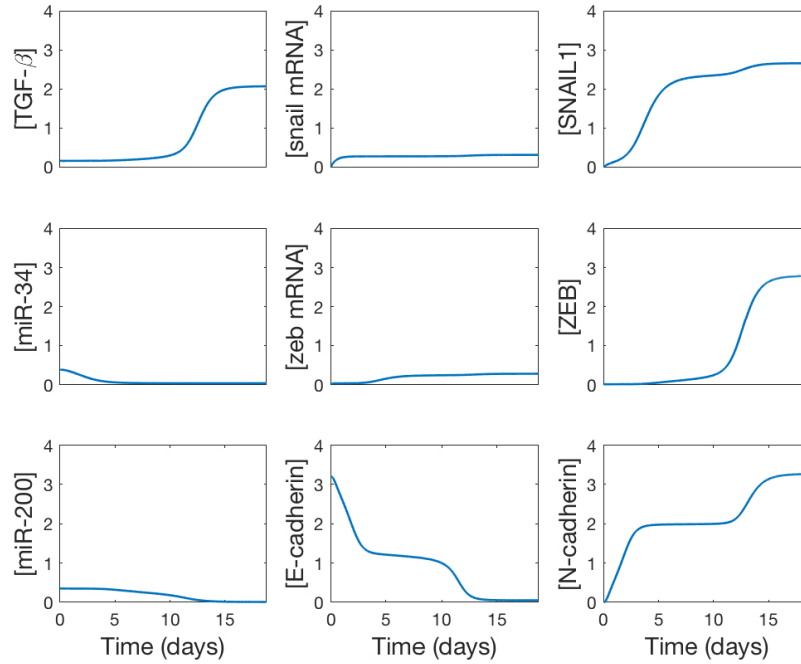


**Figure 4.3.** The endogenous  $\text{TGF-}\beta$  expression creates a self-sustaining positive feedback loop resulting in the irreversible mesenchymal phenotype state.

Formation of E-cadherin junctions requires both intracellular and extracellular events. Importantly,  $\beta$ -catenin is a primary regulatory protein in the intracellular formation of cell-cell junctions. When  $\beta$ -catenin is located at E-cadherin junctions, epithelial cells maintain the epithelial phenotype (199). However, when  $\beta$ -catenin translocates to the nucleus, whether by mechanical or chemical E-cadherin disruption, epithelial cells switch to a mesenchymal phenotype (200). This provides a mechanotransduction signaling pathway for affecting the phenotype of each cell in the CPM by acting on the EMT-associated gene regulatory network.

The three states of  $\beta$ -catenin are cytoplasmic, E-cadherin bound, and proteasome bound. Cytoplasmic  $\beta$ -catenin freely binds with either E-cadherin for junction formation or the destruction complex for proteasomal degradation (Eq. 4.12). Proteasomal

degradation of  $\beta$ -catenin (Eq. 4.13) occurs when Wnt signaling is deactivated, which is assumed to be the default state for this model (203). E-cadherin and  $\beta$ -catenin form a cytoplasmic complex before localizing to the cytoplasmic membrane (Eq. 4.11), which prevents both nuclear translocation as well as proteasomal degradation (70).

$$\frac{d[E_c]}{dt} = -a_i(t)[E_c] + d_i(t)[E/\beta], \quad (4.10)$$

$$\frac{d[E/\beta]}{dt} = \nu(E_T - [E_c] - [E/\beta])[\beta] - d_i(t)[E/\beta], \quad (4.11)$$

$$\frac{d[\beta]}{dt} = \underbrace{-\nu(E_T - [E_c] - [E/\beta])[\beta] + d_i(t)[E/\beta]}_{\text{E-cadherin-}\beta\text{-catenin complex}} - \underbrace{k_f[\beta](P_T - [C]) + k_r[C]}_{\text{Proteasomal complex}} + k_m, \quad (4.12)$$

$$\frac{d[C]}{dt} = k_f[\beta](P_T - [C]) - k_r[C] - k_2[C]. \quad (4.13)$$

Rates for the  $\beta$ -catenin system (Eq. 4.10–4.13) are listed in Table 4.2. The total proteasomal concentration in Eq. 4.12 and 4.13 is constant ( $P_T=0.33514$  nM), existing only as either bound or unbound to  $\beta$ -catenin. Cytoplasmic E-cadherin,  $E_c$ , either localizes to the membrane during cell-cell attachment,  $a_i(t)$ , or is freed from the E-cadherin- $\beta$ -catenin complex,  $[E/\beta]$ , during cell-cell detachment,  $d_i(t)$ .

| Parameter                                      | Symbol   | Value                     |
|--|----------|---------------------------|
| Total E-cadherin concentration                 | $E_T$    | 100 nM                    |
| Total proteasome concentration                 | $P_T$    | 0.33514 nM                |
| E-cadherin- $\beta$ production rate            | $\nu$    | 100 min <sup>-1</sup>     |
| E-cadherin- $\beta$ -catenin dissociation rate | $\alpha$ | 2 min <sup>-1</sup>       |
| $\beta$ -catenin proteasome binding rate       | $k_f$    | 100 min <sup>-1</sup>     |
| $\beta$ -catenin proteasome dissociation rate  | $k_r$    | 100 min <sup>-1</sup>     |
| $\beta$ -catenin degradation rate              | $k_2$    | 0.03 min <sup>-1</sup>    |
| $\beta$ -catenin production rate               | $k_m$    | 0.01 nM min <sup>-1</sup> |
| E-cadherin membrane translocation rate         | $\rho$   | 200 min <sup>-1</sup>     |

**Table 4.2.:** Parameters and rates are shown for the  $\beta$ -catenin signaling system.

### 4.2.3 Cell-cell binding and unbinding

The attachment and detachment of cells with neighboring cells are defined by the functions Eq. 4.14 and Eq. 4.15, respectively, where  $\rho$  is the E-cadherin membrane translocation rate.

$$a_i(t) = \sum_{\vec{x} \in \sigma} c_{a,t} \rho \quad (4.14)$$

$$d_i(t) = \sum_{\vec{x} \in \sigma} c_{d,t} \rho \quad (4.15)$$

The coupling functions,  $c_{a,t}$  and  $c_{d,t}$  give the difference in attachments and detachments between a cell,  $\sigma$ , and its neighboring cells,  $\sigma'$ , in units of E-cadherin molecules per min.

The general form of the coupling function for the CPM is

$$c_{t+1} = \frac{\sum_{\vec{x} \in \{\sigma, \sigma'\}} \delta(\sigma_{\vec{x}}, \sigma'_{\vec{x}})}{\sum \sigma_{\vec{x}}} - c_t, \quad (4.16)$$

in which the number of cell sites undergoing attachment and detachment are normalized to the total number of cell-occupied lattice sites,  $\sigma_{\vec{x}}$ . The Kronecker delta,  $\delta$ , returns 1 when  $\sigma'_{\vec{x}} \neq \sigma_{\vec{x}}$  and  $\sigma'_{\vec{x}} \neq 0$  and 0 otherwise

$$\delta = \begin{cases} 1 & \{\vec{x} \in \sigma' : \sigma'_{\vec{x}} \neq \sigma_{\vec{x}} \wedge \sigma'_{\vec{x}} \neq 0\} \\ 0 & \text{Otherwise} \end{cases}$$

The von Neumann neighborhood,  $N_{\sigma}^v$ , gives the neighboring cell-occupied lattice sites,  $\sigma'_{\vec{x}}$ , within Manhattan distance  $r = 1$  of cell  $\sigma$  (Eq. 4.17).

$$N_{x_0, y_0}^v = \{(x, y) : |x - x_0| + |y - y_0| = r\} \quad (4.17)$$

Here, the set of perimeter lattice sites  $\vec{x}_0, \vec{y}_0 \subset \sigma_{\vec{x}}$  have von Neumann neighbors  $\vec{x}, \vec{y}$  (Fig. 4.4). Then simply take the difference in the number of all attachment sites of cell  $\sigma$  for one Monte Carlo time step (scaling by 1 MCS = 4.8 minutes) and normalize to the number of cell lattice sites,  $\sigma_{\vec{x}}$  to find the concentration of bound E-cadherin dimers. This assumes a uniformly distributed E-cadherin concentration over the cell membrane.

#### 4.2.4 Mechanotransduction

The CPM previously described in Chapter 3 does not directly require cell-cell adhesion. Rather, the distribution of traction forces within a multicellular cluster yields strains that organize cell migration through mechanical cell-matrix feedback. As a result, cells tend to migrate towards the centroid of the multicellular cluster as per  $H_{durotaxis}$  (Eq. 3.5) yet are prevented from overgrowing by the cell-cell contact energy,  $J_{cc}$ .

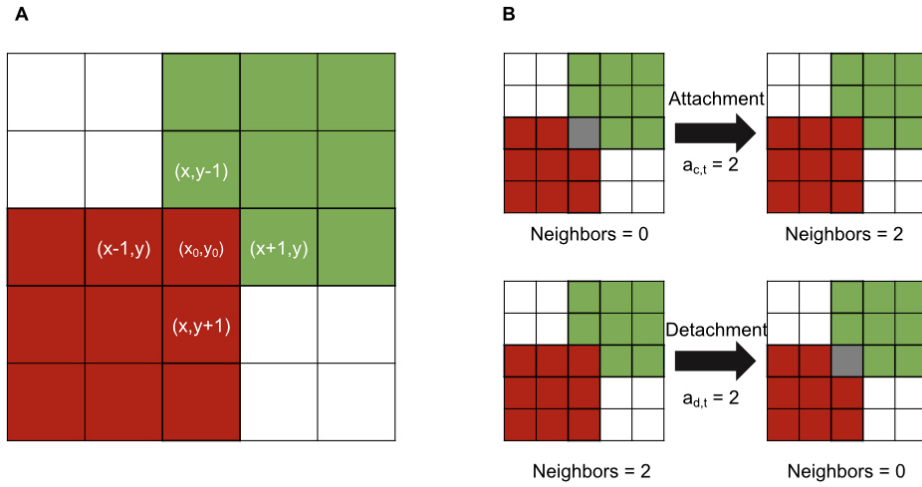


**Figure 4.4.** (A) Cell  $\sigma$  (red squares) has the perimeter lattice site  $(x_0, y_0)$  with the von Neumann contacts with cell  $\sigma'$  (green squares) at  $(x + 1, y)$  and  $(x, y - 1)$ . (B) Attachments and detachments occur when a cell extends or retracts, respectively, into a vacant lattice site (grey squares).

Cell-cell junctions, however, maintain adhesion between neighboring cells in an epithelial monolayer, and disruption requires either mechanical or chemical intervention. For To capture mechanotransduction at the cell-cell adhesion, we use the junction force predictions of the CPM as a regulator of cell attachment and detachment. Previously, Ramis-Conde and colleagues applied a similar approach to predict the mobility of cells within a monolayer (185). Given the length per contact and the adhesion energy per unit length of contact, we can determine the energy of adhesion, or the anchorage force, to maintain contact between two cells.

The anchorage force, described previously by Schaller & Meyer-Hermann (204), is related to the contact area by

$$F_{ij}^{ad} = A_{ij} f^{ad} \frac{1}{2} ([R]_i [L]_j + [R]_j [L]_i), \quad (4.18)$$

where  $A_{ij}$  is contact area between cells  $i$  and  $j$ , and  $f^{ad}$  is the adhesive coefficient in units of  $\mu\text{N} \cdot \mu\text{m}^{-1}$ . For our purposes, the receptor,  $R$ , and ligand,  $L$ , are both E-cadherin, which acts as a homodimer, and thus Eq. 4.18 reduces to

$$F_{ij}^{ad} = A_{ij} f^{ad} [E/\beta]_i [E/\beta]_j, \quad (4.19)$$

where  $[E/\beta]$  is the E-cadherin- $\beta$ -catenin complex from Eq. 4.11. The anchorage force is therefore dependent on the E-cadherin- $\beta$ -catenin complex concentration and contact area between two cells. The contact area is the sum of contacting lattice sites described in Eq. 4.16.

Ramis-Conde et al. (185) scale the adhesive coefficient  $f^{ad}$  by  $[E/\beta]$  normalized to total the E-cadherin concentration such that

$$\varrho = \frac{[E/\beta]}{E_T} \varrho_m, \quad (4.20)$$

where  $\varrho_m = 200\mu\text{N} \cdot \text{m}^{-1}$  is the maximum adhesion strength coefficient and normalized adhesion strength is on the interval  $[0 \ 1]$ . Hence, using the junction force prediction described in Chapter 3 and the anchorage force, we can determine the cell-cell bound state, which is simply the Kronecker delta function

$$\delta(J_{\sigma,\sigma'}, F_{\sigma,\sigma'}^{ad}) = \begin{cases} \text{Bound,} & \text{if } J_{\sigma,\sigma'} < F_{\sigma,\sigma'}^{ad}, \\ \text{Unbound,} & \text{Otherwise.} \end{cases} \quad (4.21)$$

### 4.2.5 Signaling network coupling

The dynamical systems of Sections 4.2.1 and 4.2.2 provide the framework for the molecular signaling pathway linking junction force to gene regulation. For molecular transduction of junction force,  $\beta$ -catenin translocates to the nucleus after sufficient accumulation in the cytoplasm, where it forms a DNA binding complex with TCF/LEF to regulate transcription of EMT genes (205). Although,  $\beta$ -catenin regulation of the EMT-associated GRN remains unclear, the Wnt/ $\beta$ -catenin signaling axis indirectly acts on EMT-TFs SNAIL1 and ZEB. Wnt signaling stabilizes both SNAIL1 and  $\beta$ -catenin through GSK3 $\beta$  inhibition (206), and TGF- $\beta$  stimulates adherens junction disruption thereby freeing  $\beta$ -catenin for nuclear translocation (207). As a result, Wnt/ $\beta$ -catenin signaling regulate EMT in a similar fashion to TGF- $\beta$ -induced EMT described by Tian et al. (181).

For simplicity, Ramis-Conde et al. (185) assumes a critical threshold for  $\beta$ -catenin activation of these transcriptional programs. Cytoplasmic  $[\beta]$  (Eq. 4.12) exceeding the threshold  $c_T = \frac{1}{2}[\beta_{\max}]$  results in nuclear translocation. In effect,  $c_T$  sets the cellular sensitivity to undergo EMT. However, we substitute the cytosolic  $\beta$ -catenin for exogenous TGF- $\beta$ ,  $[TGF_0]$ , as a perturbation to the EMT-GRN of the CBS model (Eq. 4.1 – 4.9). Hence, disruption of cell-cell adhesion by mechanical force increases  $[\beta]$  (Eq. 4.12), which in turn activates transcriptional regulation of the CBS model.

CDH1 expression (Eq. 4.8) likewise provides feedback to the  $\beta$ -catenin signaling network by adding to the cytoplasmic concentration of E-cadherin in Eq. 4.10, provided the complete translation of mRNA to E-cadherin, and Eq. 4.8 becomes

$$\frac{d[E_c]}{dt} = [E_g] - a_i(t)[E_c] + d_i(t)[E/\beta], \quad (4.22)$$

where  $[E_g]$  is the E-cadherin gene expression from Eq. 4.8. By nondimensionalization of the E-cadherin concentrations from both systems (Sections 4.2.1 and 4.2.2) to  $E_T = 100$  nM, the E-cadherin concentration bound in the membrane, available in the cytoplasm, or bound to  $\beta$ -catenin are on the interval  $[0 \ 1]$ .

## 4.2.6 Phenotype characterization

From the gene expression described in Section 4.2.1, each cell has a distinct gene expression profile from which we determine the phenotype. Using N-cadherin expression as a marker of the mesenchymal phenotype (72) and normalizing to  $[N_{\max}]$ , the phenotype-specific property for each cell is mapped on the interval  $[0 \ 1]$  in which 0 is epithelial and 1 is mesenchymal. The simulated cell characteristics are listed in Table 4.3.

## 4.2.7 Numerical simulations

The CPM is initialized as previously described (Section 3.2.6). The gene profile is initialized for each cell set to the epithelial phenotype and the corresponding phenotype-specific properties. We numerically solve for the change in gene expression after each Monte Carlo time step using the Runge-Kutta Fourth Order method with the conversion



| Parameter                 | Symbol          | Epithelial             | Mesenchymal             |
|---------------------------|-----------------|------------------------|-------------------------|
| Cell area                 | $A_0$           | $50.264 \mu\text{m}^2$ | $240.005 \mu\text{m}^2$ |
| Proliferation probability | $\rho_{divide}$ | 0.005                  | 0.0025                  |
| Cell-cell contact cost    | $J_{cc}$        | 2.5                    | 5                       |
| Cell-matrix contact cost  | $J_{cm}$        | 2.5                    | 1.25                    |

**Table 4.3.:** The parameters shown are for the phenotype-specific properties used in the CPM for Section 4.3.4

of 1 MCS  $\approx$  4.8 minutes (Section 3.3.2) and then to an in vitro timescale by  $\frac{2}{60}$  hour $^{-1}$ . The phenotype is then determined from  $\frac{[N]}{[N_{max}]}$  and cell-cell adhesion energy for each cell pair from 4.20. The anchorage force for each cell-cell pair is compared with the junction force to determine connectivity between multicellular clusters before determining the force for the following time step.

For parameter analysis, the parameter set consisted of each phenotype-specific property and phenotypes were assigned with a uniquely seeded random number on the interval [0 1], and remained fixed for the duration of the simulation. The effects of each property were qualitatively evaluated using the CPM map visualization (as shown in Ch. 3) with a jet color mapping to identify the relative phenotypes.

## 4.3 Results

### 4.3.1 Rate analysis

The phenotype for each cell is evaluated for each Monte Carlo step with a time step equivalent to a single Monte Carlo step. We considered three numerical methods for evaluating the change in expression of each gene expression profile. The built-in MATLAB ODE solver (*ode23s*, MathWorks, Natick, MA) solves stiff, low order systems of equations using an adaptive time step. We use this solution as an exact solution to the integrated  $\beta$ -catenin signaling and EMT-associated GRN for comparison with the two numerical solutions approximated by the Forward Euler and Runge-Kutta fourth-order (Fig. 4.5).

The Forward Euler (Fig. 4.5 A, B) approximates changes in gene expression with accuracy equivalent to the Runge-Kutta fourth-order (Fig. 4.5 C, D) for a time step  $h$  of 4.8 minutes. E-cadherin expression (Fig. 4.5 A, C) closely approximates the ODE solver for  $t < 9$  days for both numerical methods, and N-cadherin closely approximates for  $t < 6$  days. For later time points, the percent error increases to nearly 50% during the transition from the intermediate to mesenchymal phenotype between 8 to 14 days. Decreasing the time step to  $h = 2.4$  minutes reduces the percent error to less than 1% for both numerical solutions.

### 4.3.2 EMT-associated gene expression

To identify spatiotemporal dynamics of phenotype progression within a heterogeneous population of cells, we tracked the gene expression for each CPM cell throughout the

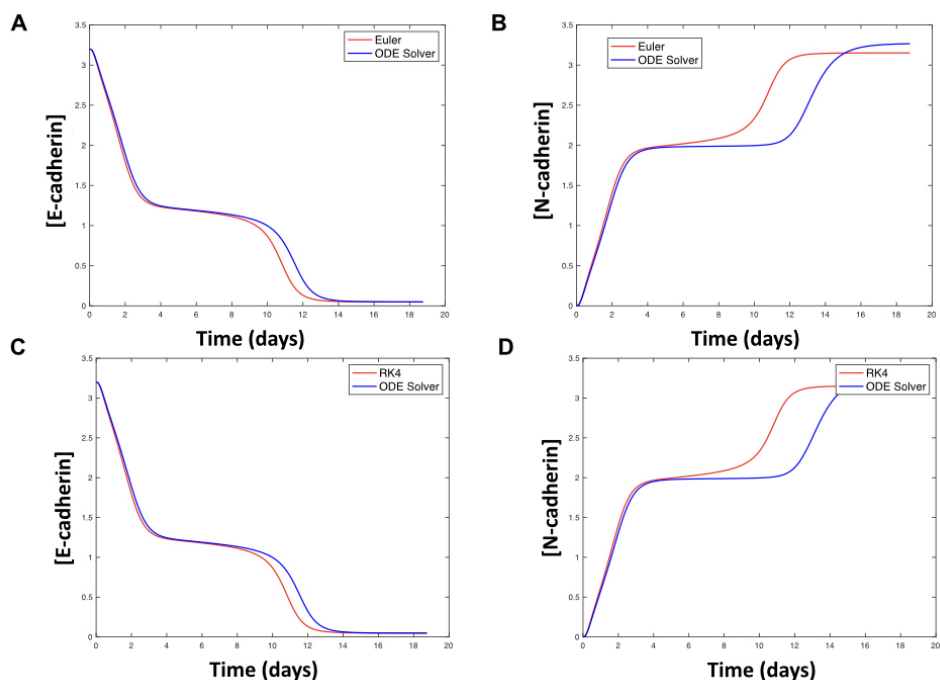


**Figure 4.5.** The numerical solution (red line) approximates the analytical solution (blue line). The numerical solution uses a time step of  $h = 4.8$  minutes and the analytical solution uses an adaptive time step set by the MATLAB ODE solver. The E-cadherin gene expression (A,C) is shown for the Forward Euler solution (top row) and the N-cadherin gene expression is shown for the Runge-Kutta fourth-order solution (bottom).

simulation. Typically, E-cadherin and N-cadherin are the respective epithelial and mesenchymal markers for delineating phenotype during EMT. Here, we used the relative expression of N-cadherin to the maximum N-cadherin expression,  $\frac{[N]}{[N_{max}]}$ , as an estimate of mesenchymal transdifferentiation and assigned the phenotype cell characteristics as discussed in 4.2.6. The gene expression of epithelial and mesenchymal markers was averaged for all CPM cells at each time point in a single simulation as shown below (Fig. 4.6).

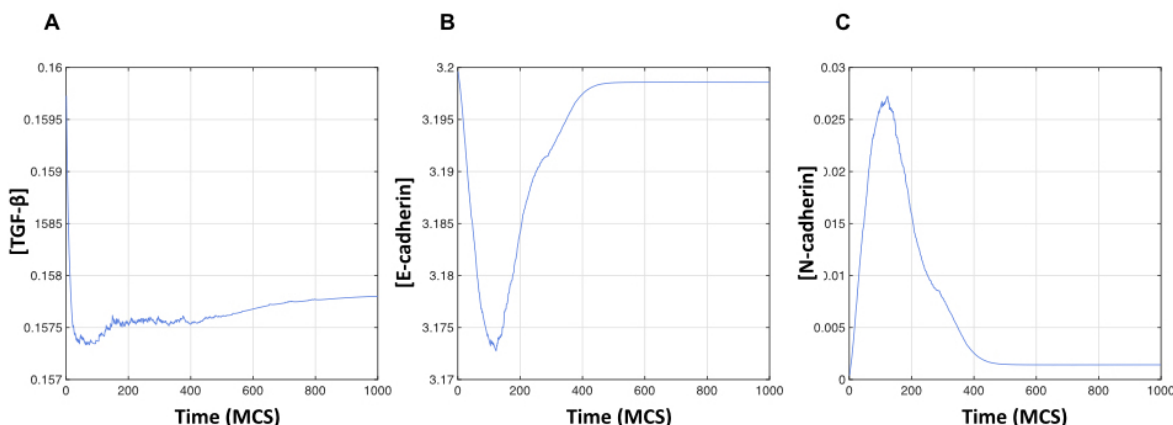
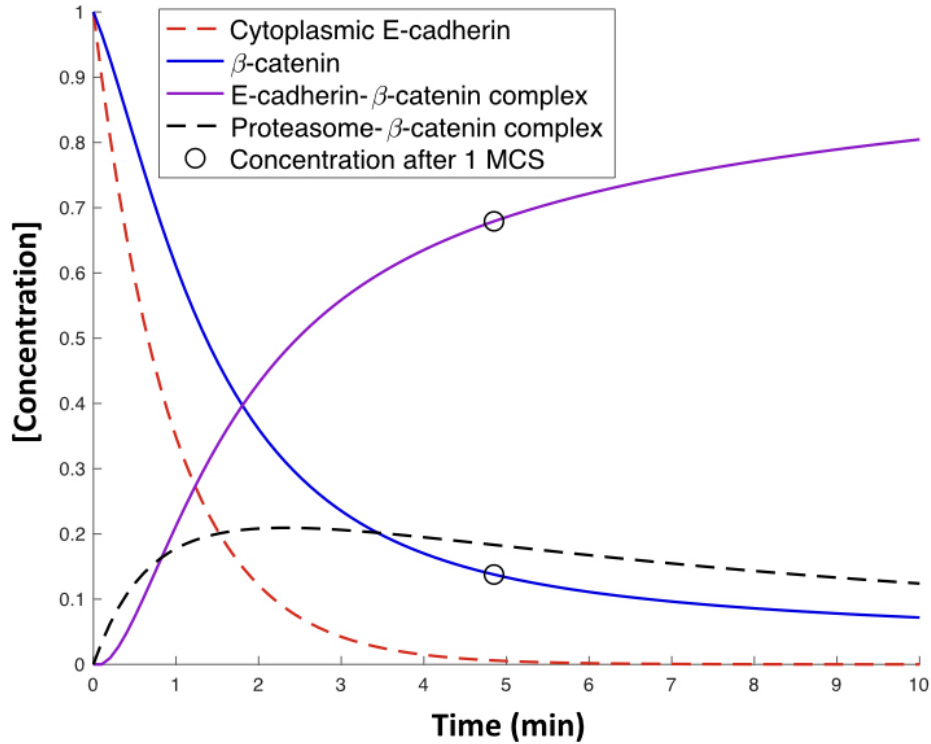


**Figure 4.6.** The temporal dynamics of gene expression of a heterogeneous cell population reflects the relative phenotypes present. Endogenous TGF- $\beta$  (A), E-cadherin (B), and N-cadherin (C) expression averaged over the cell population are shown for a single simulation. Concentrations are given in units of nM.

Prior to implementing  $\beta$ -catenin signaling dynamics, exogenous TGF- $\beta$  acts as a perturbation to the GRN. For simplicity, exogenous TGF- $\beta$  concentration is maximal ( $[TGF_0] = 3 \text{ nM}$ , Table S2) when a cell has no contacting neighbors and 0 otherwise. The endogenous TGF- $\beta$  concentration (Fig. 4.6 A) rapidly decreased to an expression just below the initial concentration (Table 4.1) and stabilized for  $t > 50 \text{ MCS}$ , suggesting that the cells were not able to undergo EMT before reaching confluence. E-cadherin expression (Fig. 4.6 B) decreased during the initial dynamic phase  $0 < t < 200 \text{ MCS}$  accompanied by a reciprocal increase in N-cadherin expression (Fig. 4.6 C), likely owing to the reduced cell-cell adhesion of the subconfluent monolayer previously observed in Fig. 3.2. The expression of TGF- $\beta$ , E-cadherin, and N-cadherin illustrate the relative progression in phenotype for the entire cell population, from which we identify the relative dynamics of EMT-associated events.

### 4.3.3 $\beta$ -catenin signaling

Previously, we substituted exogenous TGF- $\beta$  for  $\beta$ -catenin signaling as a perturbation to the EMT-associated GRN. However,  $\beta$ -catenin signaling regulates cell-cell adhesion by either mechanically coupling the adherens junction to the actin cytoskeleton or through nuclear translocation and suppression of the E-cadherin gene, CDH1. To capture the effects of mechanotransduction on EMT, we first implement the Ramis-Conde  $\beta$ -catenin signaling framework (185) with a dependence on cell-cell contact (Eq. 4.10–4.13). The MATLAB ODE solution (ode45, MathWorks, Natick, MA) to this system is shown in Fig. 4.7.



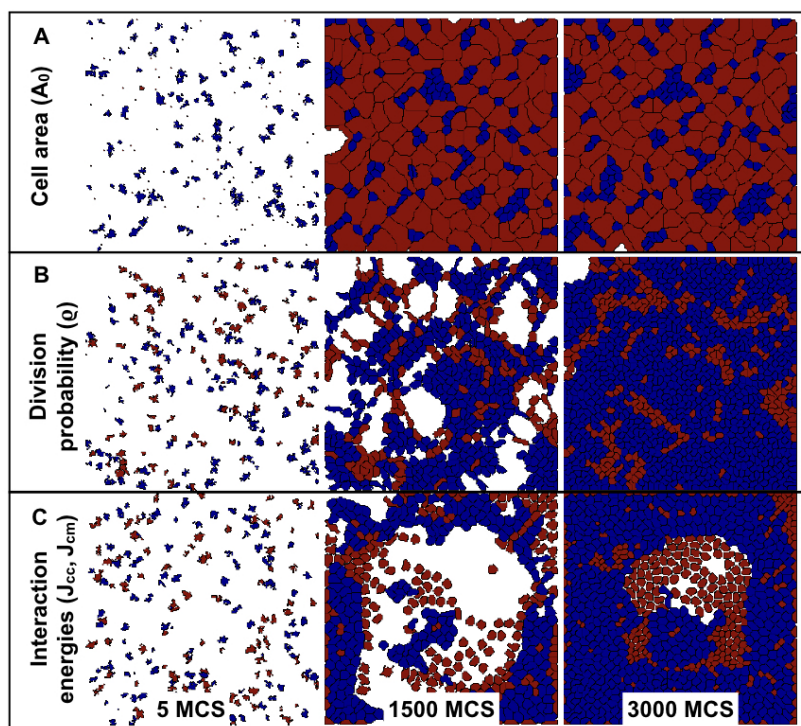
**Figure 4.7.** Cell-cell adhesion regulates  $\beta$ -catenin signaling. Free  $\beta$ -catenin (blue line) either forms a complex with cytoplasmic E-cadherin (purple line) or with a proteasome (black line). E-cadherin is either localized at the cell-cell contact as the E-cadherin- $\beta$ -catenin complex or unbound in the cytoplasm (red line). The concentration after 1 MCS is indicated at 4.8 minutes (circle). Values are normalized to  $[E]_{max} = 100$  nM.

Figure 4.7 shows the concentrations of the four state parameters after cell-cell contact at  $t = 0$  minutes. Initially,  $\beta$ -catenin and E-cadherin are unbound in the cytoplasm. The total E-cadherin concentration is conserved and either is unbound as cytoplasmic E-cadherin or bound as a E-cadherin- $\beta$ -catenin complex, which localizes at the cell-cell contact to form an adherens junction. The proteasome is also conserved and forms a complex with free  $\beta$ -catenin for polyubiquitination and degradation. E-cadherin-

$\beta$ -catenin complex formation has an initial toe region  $0 < t < 0.25$  minutes followed by a region of linear growth  $0.25 < t < 3$  minutes before stabilizing at approximately 80 nM for  $t > 6$  minutes, which is limited by the availability of cytoplasmic E-cadherin. After 1 MCS the concentration of the E-cadherin- $\beta$ -catenin complex is approximately 70% of  $[E/\beta]_{max}$ , which suggests an adherens junction bond strength of  $1.40 \times 10^{-4} \mu\text{N} \cdot \mu\text{m}^{-1}$  from Eq. 4.20.  $[E/\beta] < [E/\beta]_{max}$  and thus  $\varrho < \varrho_m$  without the production of additional E-cadherin by the EMT-associated GRN. Rather than a static threshold for  $\beta$ -catenin nuclear translocation and regulation of cell mobility, this  $\beta$ -catenin concentration substitutes for the exogenous TGF- $\beta$  perturbation to the EMT-associated GRN, which has an intrinsic resistance to perturbation due to the miR-34 and miR-200 inhibitory feedback (see Fig. 4.3).

#### 4.3.4 Phenotype properties

A key result of the GRN is the effect of phenotype on cellular properties. Here, we qualitatively show the effect of each phenotype-specific property described in Section 4.2.6 on the spatial distribution of a heterogeneous cell population (Fig. 4.8, S5 Video).



**Figure 4.8.** The phenotype-specific properties of a heterogeneous cell population with static phenotypes exhibit differential spatial patterning. Each phenotype property shown refers to the values in Table 4.3.

Each cell property was varied independently of the others for 3,000 MCS (10 days), and each cell was randomly assigned an epithelial (0, blue cells) or mesenchymal (1, red cells) phenotype, which remained unchanged throughout the simulation. The larger cell area of the mesenchymal phenotype (Fig. 4.8 A) more frequently exceeds the threshold area described in Section 3.2.5, which allows for rapid proliferation. As a result, the mixed cell population rapidly reaches confluence before the subpopulations are able to redistribute. The larger epithelial division probability (Fig. 4.8 B) forms multicellular clusters surrounding the mesenchymal subpopulation, which then begin to form embedded multicellular clusters. Similar to the effects of cell area, the division



*CHAPTER 4. EMT-GRN*

probability is restrictive to spatial redistribution of the subpopulations. Lastly, the interaction energy (Fig. 4.8 C) produced epithelial spatial distributions visually similar to that observed in Fig. 3.1 with self-organization of heterogeneous subpopulations.

# Chapter 5

## Discussion

The goal of this work was to develop a computational framework for evaluating the mechanochemical regulation of the EMT program. In Chapters 2 and 3, we describe an original, multiscale model integrating both molecular and cellular signaling with physiologically relevant EMT-associated features. Expanding on previous computational approaches, we introduced cell proliferation and collective cell dynamics to reproduce EMT-associated cellular processes observed *in vitro*. We next used these junction force predictions in regulation of cell-cell contacts, which are coupled to an intracellular signaling cascade that targets the EMT-GRN. The gene expression of epithelial and mesenchymal markers from this EMT-GRN then approximate the phenotype for each cell, which then sets the phenotype-specific properties of those cells. One of the distinct features of our computational approach is the ability to capture dynamics of EMT-associated processes from the molecular to the tissue scale. This computational approach provides a more thorough characterization of the previously unknown mechanical and

chemical sequence of events, and in so doing lends itself to the elucidation of the physiological and pathophysiological processes of the EMT program.

## Chapter 3

In Chapter 3, we extended the van Oers model to account for cell proliferation and force transduction about multicellular geometries. As a result, the CPM predicted spatial distributions of intercellular tension as the second moment of area about the multicellular cluster.

The CPM model demonstrates that traction forces scale with the size of the multicellular cluster, a consequence of the FMA in which traction force is applied at uniformly distributed cell-matrix adhesions (i.e., at all pixels in the CPM). A cell cluster or monolayer may therefore regulate traction forces by varying the density or distribution of cell-matrix adhesions, i.e. focal adhesions. The model further predicts intercellular tension, by maintaining isometric tension throughout the monolayer, which further regulates the distribution of cytoskeletal stress within a monolayer. Our simulations predict that the intercellular tension nonlinearly decays with distance from the monolayer centroid, which reflects the net distribution of cytoskeletal stress. The observed differences between simulations and experiments may owe to the lack of heterogeneity of phenotype-specific cellular properties, such as cell area and the number of cell-cell and cell-matrix attachments. The FRET analysis of mammary breast epithelium indicated junction force distribution depends on monolayer geometry and not individual cell geometry, and the trends of our extended multicellular FMA model

## CHAPTER 5. DISCUSSION

capture many key properties of monolayers undergoing EMT. Although the model poorly reproduces spatial distribution trends observed in the control epithelial colony.

When coming into contact with other epithelial cells, migrating cells arrest growth and form a cell-cell adhesion, which reduces the cell-cell contact inhibition. Disruption of epithelial junctions results in redistribution of tension from the cell-cell junctions to the cell-matrix attachments, thereby increasing mobility, growth, and spreading (194). By TGF- $\beta$ -induced EMT, cell area increases significantly in the periphery of the monolayer accompanied by a slight decrease in intercellular tension relative to the interior of the monolayer. This finding would seem to suggest a shift from cell-cell to cell-matrix adhesion in the peripheral population. This attachment shift is reflected in the CPM cell-cell and cell-matrix contact energies. By altering the cell-cell contact energy, the CPM captures the effect of contact inhibition of neighboring cells *in vitro*. However, in the CPM model, a defined target area partially constrains the simulated cell area that, in turn, limits cell-matrix adhesion. The shift from cell-cell contact to cell-matrix adhesion is indirectly restricted as a result. The spatial distribution of intercellular tension therefore predicts the spatial distribution of cell area, which would seem to indicate a shift towards cell-matrix adhesion.

Building on previous works that illustrate tensional homeostasis drives tissue morphogenesis, these findings demonstrate that a gradient of intercellular tension forms even in the absence of heterogeneous cell populations. Through transduction of the mechanical gradient to molecular signaling pathways, tension distribution provides positional information within a monolayer that regulates cellular phenomena such as growth, proliferation, migration. This is of particular interest to spatially localized

## CHAPTER 5. DISCUSSION

EMT-associated cellular processes, which corresponds with cell stress in the outer cell population of the monolayer (162).

Although the various interaction energies reflect the resultant behavior of TGF- $\beta$ -induced EMT, differences observed in experimental and computational findings suggest phenotype-specific properties are necessary to systematically reproduce spatiotemporal dynamics of EMT. In Chapter 4, we explore the mechanochemical signaling interplay to more accurately capture phenotype heterogeneity in an epithelial monolayer.

### Chapter 4

In Chapter 4, we integrate an EMT-associated GRN and  $\beta$ -catenin signaling to capture mechanical feedback at cell-cell junctions. The EMT-GRN regulates epithelial and mesenchymal genetic markers E-cadherin and N-cadherin, and is sensitive to exogenous TGF- $\beta$ . The  $\beta$ -catenin signaling system transduces the intercellular tension across cell-cell junctions to a molecular signaling pathway. To couple the two systems, we substitute the exogenous TGF- $\beta$  perturbation for the  $\beta$ -catenin concentration and, likewise, introduce the EMT-GRN E-cadherin expression to the production of cytoplasmic E-cadherin. By approximating the phenotype from N-cadherin expression, we assign the phenotype-specific properties of cell area, proliferation rate, and contact penalties for the CPM cells.

Coupling intercellular tension with downstream signaling captures a mechanically-coupled gene regulatory network, which allows for tracking of unique phenotypes and gene expression profiles for each cell in the simulation. This approach provides two distinct advantages. Firstly, the initial loss of intercellular junctions permits a

## *CHAPTER 5. DISCUSSION*

partial phenotypic state, indicative of an intermediate mesenchymal phenotype. Once a confluent monolayer of epithelial cells form, and intercellular junctions form, cells may revert back to an epithelial phenotype, which resembles rounds of EMT during embryonic development. Secondly, after an epithelial sheet has formed, we can test phenotype sensitivity of the epithelial sheet to parametric variations. We can additionally determine if latent, intermediate phenotypes form without disrupting tissue homeostasis at either subconfluence or confluence. An understanding of the interconnectivity between mechanical and molecular stimuli will reveal critical signaling dynamics as potential targets of anti-metastatic therapeutic strategies.

### **Conclusion**

These findings offer insight into the coordinated induction of the EMT program by mechanical and molecular stimuli, which are otherwise difficult to capture experimentally. The key predictions presented in this work reveal critical intracellular signaling dynamics necessary to understanding the pathophysiology of EMT-associated diseases. By combining these approaches with extracellular feedback in future work, we will be able to capture EMT events spanning molecular, cellular, and tissue scale dynamics, thereby identifying the critical distinction in EMT as a healthy and an aberrant regulator of tissue homeostasis.

## Limitations

### Cellular Potts model

The finite element substrate described in Chapter 3 is a two-dimensional lattice with cell attachments projected from the cell-occupied lattice site to its corresponding four nodes, each node representing a separate attachment. This assumes discrete, linearly spaced attachments and the cytoskeleton acts as a continuous structure. Furthermore, we similarly consider a multicellular cluster to behave as a cohesive structure by requiring the force transduction between cells to be linearly elastic. Therefore traction forces scale in proportion to the linear distance from the centroid about the multicellular geometry. In other words, traction force localizes to the cluster periphery. However, this may only hold for an epithelial population in static equilibrium due to the high degree of interconnection between neighboring cells (208).

### Phenotype characterization

For monolayers containing subpopulation of cells with a high degree of individual cell motility, the multicellular cluster transitions from static equilibrium to a dynamic tissue - a process with similarities to EMT known as unjamming (209). This subpopulation may migrate independently of the cluster despite maintaining cell-cell junctions.

One approach to address this issue is to set a phenotype-specific contractile strength ( $\mu$ , Eq. 3.12). By altering the peak traction force for a set area, partially differentiated cells create preferential localized strains which reduce the local durotaxis Hamiltonian

(Eq. 3.5) when moving away from the multicellular geometry, resulting in increased mobility relative to the multicellular cluster.

## Gene regulatory network

The deterministic EMT-GRN in Eqs. 4.1–4.9 and shown in Fig. 4.1 reproduces the gene expression of key epithelial and mesenchymal gene markers E-cadherin and N-cadherin in response to an applied perturbation by TGF- $\beta$ . However, molecular signaling networks are inherently stochastic. For the transcription factors, mRNA, miRNA, and EMT genes characterized by Michaelis-Menten kinetics, the general rate equation for a double negative feedback loop has the form



where  $[A]$  is the mRNA for transcription factor  $[C]$ , and  $[B]$  is the miRNA. The miRNA represses translation of  $[A]$  to  $[C]$ , and likewise the transcription factor represses  $[B]$ , which yields increased translation of  $[C]$ . The production of  $[C]$  has rate  $k^+$  and degradation of  $[C]$  has rate  $k^-$ .

The ODE for Eq. 5.1 is given by

$$\frac{d[C]}{dt} = k^+ \frac{[A]}{1 + \frac{[B]^n}{J}} - k^- [C], \quad (5.2)$$

where the Michaelis-Menten constant,  $J$ , is for the species production rate and the Hill coefficient,  $n$ , of species inhibition is equal for all species in the network. Applying the white noise process  $\xi(t)$  to Eq. 5.2 yields



$$\frac{d[C]}{dt} = \underbrace{k^+ \frac{[A]}{1 + \frac{[B]^n}{J}} - k^- [C]}_{a(x,t)} + \underbrace{\frac{\sigma}{\sqrt{\Delta t}} \xi(t)}_{b(x,t)}, \quad (5.3)$$

which is the stochastic differential equation (SDE) of the general ODE. The deterministic term is denoted by  $a(x,t)$  and the stochastic term is denoted by  $b(x,t)$ .

Next we apply the Euler-Maruyama method to approximate the numerical solution of the general SDE in Eq. 5.3. The time discretization of the continuous stochastic differential equation assumes

$$\frac{d[C]}{dt} \approx \frac{\Delta C}{\Delta t} \Rightarrow \frac{C_{j+1} - C_j}{\Delta t} \quad (5.4)$$

and

$$\xi(t) = \frac{\Delta B}{\Delta t} \approx \frac{N(0, 1)}{\sqrt{\Delta t}}, \quad (5.5)$$

where  $\Delta B$  is the Brownian motion process with mean 0 and variance 1. Substituting Eq. 5.4 and Eq. 5.5 into Eq. 5.3 and solving for  $[C]_{j+1}$  yields the numerical solution

$$[C]_{j+1} = [C]_j + \left( k^+ \frac{[A]_j}{1 + \frac{[B]_j^n}{J}} - k^- [C] \right) \Delta t + \sigma \sqrt{\Delta t} N(0, 1) \quad (5.6)$$

for  $[C]$  at  $t_{j+1}$ . This approach was applied to each ODE of the gene regulatory network in Eq. 4.1–4.9 and the result is shown in S3 Figure.

## Future directions

### Extracellular matrix, epithelial-mesenchymal transition, and growth factor signaling

In addition to intercellular and subcellular signaling mechanisms, an extensive extracellular signaling network also induces the same EMT-GRN discussed in Chapter 4 through mechanical and chemical stimuli. Previous computational models discussed in Section 2.5 have illustrated the importance of molecular and mechanical feedback from the extracellular matrix to drive EMT progression (176; 175; 177). The mechanism is thought to heavily depend on TGF- $\beta$ , which upregulates production of the mesenchymal marker fibronectin (59). A latent form of TGF- $\beta$  then binds to the growth factor-binding domain of assembled fibronectin, concentrating TGF- $\beta$  at the cell surface (60). Hence, TGF- $\beta$  is self-amplifying by stimulating fibronectin production and assembly.

To computationally reproduce this fibronectin and TGF- $\beta$  positive feedback loop, a similar approach taken by Daub & Merks (177) can be applied to model fibronectin and TGF- $\beta$  availability as either soluble, insoluble, or bound. The soluble form freely diffuses from the source cell. In this way, each cell producing fibronectin and TGF- $\beta$  creates a localized chemotactic gradient. The insoluble fibronectin concentration requires both cell contractility and soluble fibronectin for assembly. The bound TGF- $\beta$  concentration necessarily requires insoluble, unbound fibronectin, although soluble TGF- $\beta$  is capable of inducing EMT in the absence of fibronectin. The chemotactic gradient is then applied to the CPM as a chemotactic Hamiltonian term, which reduces the cell-matrix contact

## *CHAPTER 5. DISCUSSION*

energy for extensions lattice sites containing fibrillar fibronectin, bound TGF- $\beta$ , or soluble TGF- $\beta$ .

This approach to modeling extracellular signaling feedback addresses the lack of an ECM creation term in the Daub-Merks model. This presents two additional advantages for implementation in a model of EMT. Firstly, ECM is closely regulated by the EMT program. Secondly, ECM feedback induces phenotype-tailored cellular behavior by sequestering growth factors at the cell surface and presenting mechanically distinct loci. The assembled fibronectin and sequestered TGF- $\beta$  at lattice domains presents an original and adaptable chemotactic as well as haptotactic gradient for guiding cell migration.

# 6

## Supporting Information

### Chapter 3

**S1 Figure Connectivity of multicellular clusters.** Simplified depiction of four neighboring cells (gray) forming a multicellular cluster and the corresponding adjacency matrix,  $A$  (left). Traction forces (red arrows) are proportional to the FMA about the centroid of the cluster (green dot). Junction forces (blue arrows) balance the net force imbalance for a given cell. The linear system is constructed from the mechanical equilibrium matrix and junction symmetry matrix (right). The mechanical equilibrium matrix is constructed from the connectivity of each cell given by the adjacency matrix and by applying the force balancing principle. The junction symmetry matrix requires each junction force across a cell-cell adhesion to be equal and opposite.

## 6. SUPPORTING INFORMATION

**S2 Figure Substrate strains of the single and multicellular FMA.** Substrate strains are shown for the FMA model of traction forces using the single cell geometry (A) or multicellular geometry (B).

**T1 Cellular Potts model and Finite element model parameters.** Parameters shown are for the CPM used in Chapters 3 and 4.

**S1 Video. Single cell without proliferation.** Simulated cell organization for the single cell FMA model as shown in Figure 3.1A. Movie corresponds to simulation of 1000 Monte Carlo Steps.

**S2 Video. Multicellular without proliferation.** Simulated cell organization for the multicellular FMA model as shown in Figure 3.1B. Movie corresponds to simulation of 1000 Monte Carlo Steps.

**S3 Video. In vitro proliferation.** Spatiotemporal dynamics of MCF10A cells confined to a  $250\ \mu\text{m} \times 250\ \mu\text{m}$  PDMS square as shown in Figure 3.2A. Movie corresponds with experiments of 24 hours.

**S4 Video. Multicellular CPM with proliferation.** Spatiotemporal dynamics of simulated cells for the multicellular FMA model with cell division probability of 0.5% per time step as shown in Figure 3.2B. Movie corresponds to simulation of 1,000 Monte Carlo Steps.

## Chapter 4

### S3 Figure EMT-associated gene regulatory network with stochastic

**dynamics.** The intermediate state is largely promoted by endogenous TGF- $\beta$  expression (Eq. 4.1), which is significantly diminished at steady state in the stochastic solution (S3 Figure). As the sole inhibitor of TGF- $\beta$  translation, miR-200 (Eq. 4.6), and miRNAs and mRNAs in general, are more sensitive to intrinsic noise due to low copy numbers. This effect is also observed in *zeb*, *snail*, and miR-34 in the stochastic system. Thus, the sensitivity of miRNA and mRNA to noise in the system likely diminished the endogenous TGF- $\beta$  expression, which in turn diminished the biphasic behavior of ZEB, and thus regulation of E-cadherin and N-cadherin.

There are also significant limitations to the Euler-Maruyama method applied here that could cause a loss of important dynamics. One limitation is the uniform time step used to approximate a nonlinear Markov process. Dynamics in the toe regions of the sigmoidal curves are particularly susceptible to noise due to the rapid rate of change relative to the dynamics at other time points in the simulation. Simply reducing the time step quickly becomes computationally expensive. A second limitation is that the coupled differential equations have uncoupled noise and the copy number of mRNA and miRNA is small when compared to the transcription factors and proteins.

One approach to address the time step limitation is to implement a  $\tau$ -leap method in which the time step is a Poisson distribution of the random variable. The update procedure for Eq. 5.6 would be written as  $[C](t + \tau) = [C]t + \sum_{j \in M} v_j K_j + \sigma \sqrt{\Delta t} N(0, 1)$ , where  $K_j$  is the Poisson distribution  $P(a_j(X(t))\tau)$  with mean  $a_j(X(t))\tau$  and propensity function for the  $j_{th}$  reaction is  $a_x(X(t))$ . The Poisson  $\tau$ -leap thus updates each chemical

## 6. SUPPORTING INFORMATION

reaction on the interval  $[t, t + \tau)$  before moving to the next time step. A number from the Poisson distribution is randomly generated on each time step, which gives inherent noise to the system. The white noise term is retained to also simulate exogenous noise. This is a computationally scalable approach for large stochastic systems.

Next, to address the noise sensitivity of low molecule numbers in the stochastic approximation to a nonlinear Markov process, simply scale each molecule from concentration to its number. Then randomly update the molecule number as an integer for each reaction with the likelihood of an update dependent on the function propensity function for that reaction. This method - known as the stochastic simulation algorithm, or Gillespie algorithm - reflects the dynamics of cellular processes such that the change of molecules is not tracked as a change in concentration, but rather the total number of molecules in a cell.

Combining the Poisson  $\tau$ -leap method and the Gillespie algorithm accounts for the internal stochasticity while reducing the computational limitations of small fixed time steps. Although some genetic networks may demonstrate a reduced sensitivity to noise in a cellular process, the stochastic system, when given in the complete context of gene regulation of spatiotemporally dynamic processes such as EMT, may produce phenotypes that otherwise would be difficult to capture experimentally or in a deterministic system. This is particularly true in dealing with gene regulatory networks consisting of many pleiotropic genes.

### **T2 EMT-associated gene regulatory network parameters and rates.**

Parameters and rates are shown for the EMT-associated gene regulatory network used in Chapter 4.

## 6. SUPPORTING INFORMATION

**S5 Video. Single cell without proliferation.** Simulated cell organization for the phenotype-specific cell area as shown in Figure 4.8A. Movie corresponds to simulation of 3,000 Monte Carlo Steps.

**S6 Video. Single cell without proliferation.** Simulated cell organization for the phenotype-specific division probability as shown in Figure 4.8B. Movie corresponds to simulation of 3,000 Monte Carlo Steps.

**S7 Video. Single cell without proliferation.** Simulated cell organization for the phenotype-specific interaction energy as shown in Figure 4.8C. Movie corresponds to simulation of 3,000 Monte Carlo Steps.



# References

1. Acloque H, Thiery JP, Nieto MA. The physiology and pathology of the EMT;9(4):322–326. doi:10.1038/embor.2008.30.
2. Bryant DM, Mostov KE. From cells to organs: building polarized tissue;9(11):887–901. doi:10.1038/nrm2523.
3. Alberts B, Johnson A, Lewis J, Raff M, Roberts K, Walter P. Molecular Biology of the Cell. 4th ed. Garland Science;.
4. Manninen A. Epithelial polarity – Generating and integrating signals from the ECM with integrins;334(2):337–349. doi:10.1016/j.yexcr.2015.01.003.
5. O’Brien LE, Jou TS, Pollack AL, Zhang Q, Hansen SH, Yurchenco P, et al. Rac1 orientates epithelial apical polarity through effects on basolateral laminin assembly;3(9):831–838. doi:10.1038/ncb0901-831.
6. Rodriguez-Boulan E, Macara IG. Organization and execution of the epithelial polarity programme;15(4):225–242. doi:10.1038/nrm3775.
7. Koch AW, Bozic D, Pertz O, Engel J. Homophilic adhesion by cadherins;9(2):275–281. doi:10.1016/S0959-440X(99)80038-4.
8. Harrison OJ, Bahna F, Katsamba PS, Jin X, Brasch J, Vendome J, et al. Two-step adhesive binding by classical cadherins;17(3):348–357. doi:10.1038/nsmb.1784.
9. De Craene B, Berx G. Regulatory networks defining EMT during cancer initiation and progression;13(2):97–110. doi:10.1038/nrc3447.
10. Salvador E, Burek M, Förster CY. Tight Junctions and the Tumor Microenvironment;4:135–145. doi:10.1007/s40139-016-0106-6.
11. Moreno-Bueno G, Portillo F, Cano A. Transcriptional regulation of cell polarity in EMT and cancer;27(55):6958–6969. doi:10.1038/onc.2008.346.

## REFERENCES

12. Ozdamar B, Bose R, Barrios-Rodiles M, Wang HR, Zhang Y, Wrana JL. Regulation of the polarity protein Par6 by TGFbeta receptors controls epithelial cell plasticity;307(5715):1603–1609. doi:10.1126/science.1105718.
13. Weng M, Wieschaus E. Myosin-dependent remodeling of adherens junctions protects junctions from Snail-dependent disassembly;212(2):219–229. doi:10.1083/jcb.201508056.
14. Nieto MA, Huang RJ, Jackson R, Thiery J. EMT: 2016;166(1):21–45. doi:10.1016/j.cell.2016.06.028.
15. Broster SA, Kyprianou N. Epithelial–mesenchymal transition in prostatic disease;11(23):3197–3206. doi:10.2217/fon.15.253.
16. Heerboth S, Housman G, Leary M, Longacre M, Byler S, Lapinska K, et al. EMT and tumor metastasis;4. doi:10.1186/s40169-015-0048-3.
17. Huang L, Wu RL, Xu AM. Epithelial-mesenchymal transition in gastric cancer;7(11):2141–2158.
18. Peinado H, Olmeda D, Cano A. Snail, Zeb and bHLH factors in tumour progression: an alliance against the epithelial phenotype?;7(6):415–428. doi:10.1038/nrc2131.
19. Yeung KT, Yang J. Epithelial–mesenchymal transition in tumor metastasis;11(1):28–39. doi:10.1002/1878-0261.12017.
20. Broders-Bondon F, Nguyen Ho-Boulidoires TH, Fernandez-Sanchez ME, Farge E. Mechanotransduction in tumor progression: The dark side of the force;217(5):1571–1587. doi:10.1083/jcb.201701039.
21. Paszek MJ, Weaver VM. The Tension Mounts: Mechanics Meets Morphogenesis and Malignancy;9(4):325–342. doi:10.1007/s10911-004-1404-x.
22. Brown AC, Fiore VF, Sulchek TA, Barker TH. Physical and chemical microenvironmental cues orthogonally control the degree and duration of fibrosis-associated epithelial-to-mesenchymal transitions;229(1):25–35. doi:10.1002/path.4114.
23. Leight JL, Wozniak MA, Chen S, Lynch ML, Chen CS, Wang YL. Matrix rigidity regulates a switch between TGF- $\beta$ 1-induced apoptosis and epithelial–mesenchymal transition;23(5):781–791. doi:10.1091/mbc.e11-06-0537.
24. O’Connor JW, Riley PN, Nalluri SM, Ashar PK, Gomez EW. Matrix Rigidity Mediates TGF $\beta$ 1-induced Epithelial-Myofibroblast Transition by Controlling Cytoskeletal Organization and MRTF-A Localization;230(8):1829–1839. doi:10.1002/jcp.24895.

## REFERENCES

25. Haasters F, Prall WC, Anz D, Bourquin C, Pautke C, Endres S, et al. Morphological and immunocytochemical characteristics indicate the yield of early progenitors and represent a quality control for human mesenchymal stem cell culturing;214(5):759–767. doi:10.1111/j.1469-7580.2009.01065.x.
26. Hay ED. The mesenchymal cell, its role in the embryo, and the remarkable signaling mechanisms that create it;233(3):706–720. doi:10.1002/dvdy.20345.
27. Thiery JP, Acloque H, Huang RYJ, Nieto MA. Epithelial-Mesenchymal Transitions in Development and Disease;139(5):871–890. doi:10.1016/j.cell.2009.11.007.
28. Paluch EK, Nelson CM, Biais N, Fabry B, Moeller J, Pruitt BL, et al. Mechanotransduction: use the force(s);13. doi:10.1186/s12915-015-0150-4.
29. Kumar S, Das A, Sen S. Extracellular matrix density promotes EMT by weakening cell-cell adhesions.;10(4):838–50. doi:10.1039/c3mb70431a.
30. Katsuno Y, Lamouille S, Derynck R. TGF- $\beta$  signaling and epithelial–mesenchymal transition in cancer progression;;25(1):76–84. doi:10.1097/CCO.0b013e32835b6371.
31. Heldin CH, Landström M, Moustakas A. Mechanism of TGF- $\beta$  signaling to growth arrest, apoptosis, and epithelial–mesenchymal transition;21(2):166–176. doi:10.1016/j.ceb.2009.01.021.
32. Gjorevski N, Boghaert E, Nelson CM. Regulation of Epithelial-Mesenchymal Transition by Transmission of Mechanical Stress through Epithelial Tissues;5(1):29–38. doi:10.1007/s12307-011-0076-5.
33. Cichon MA, Nelson CM, Radisky DC. Regulation of Epithelial-Mesenchymal Transition in Breast Cancer Cells by Cell Contact and Adhesion;14s3:CIN.S18965. doi:10.4137/CIN.S18965.
34. O’Connor JW, Gomez EW. Biomechanics of TGF $\beta$ -induced epithelial-mesenchymal transition: implications for fibrosis and cancer;3:23. doi:10.1186/2001-1326-3-23.
35. Kalluri R, Weinberg RA. The basics of epithelial-mesenchymal transition;119(6):1420–1428. doi:10.1172/JCI39104.
36. Radisky DC. Epithelial-mesenchymal transition;118(19):4325–4326. doi:10.1242/jcs.02552.
37. Jolly MK, Tripathi SC, Jia D, Mooney SM, Celiktaş M, Hanash SM, et al. Stability of the hybrid epithelial/mesenchymal phenotype;7(19):27067–27084. doi:10.18632/oncotarget.8166.

## REFERENCES

38. Puisieux A, Brabletz T, Caramel J. Oncogenic roles of EMT-inducing transcription factors;16(6):488–494. doi:10.1038/ncb2976.
39. Bedi U, Mishra VK, Wasilewski D, Scheel C, Johnsen SA. Epigenetic plasticity: a central regulator of epithelial-to-mesenchymal transition in cancer;5(8):2016–2029. doi:10.18632/oncotarget.1875.
40. Skrypek N, Goossens S, Smedt ED, Vandamme N, Berx G. Epithelial-to-Mesenchymal Transition: Epigenetic Reprogramming Driving Cellular Plasticity;33(12):943–959. doi:10.1016/j.tig.2017.08.004.
41. Gonzalez DM, Medici D. Signaling mechanisms of the epithelial-mesenchymal transition;7(344):re8–re8. doi:10.1126/scisignal.2005189.
42. Zhang J, Tian XJ, Zhang H, Teng Y, Li R, Bai F, et al. TGF- $\beta$ -induced epithelial-to-mesenchymal transition proceeds through stepwise activation of multiple feedback loops;7(345):ra91–ra91. doi:10.1126/scisignal.2005304.
43. Whiteman E, Liu CJ, Fearon E, Margolis B. The transcription factor snail represses Crumbs3 expression and disrupts apico-basal polarity complexes;27(27):3875–3879. doi:10.1038/onc.2008.9.
44. Lamouille S, Xu J, Derynck R. Molecular mechanisms of epithelial–mesenchymal transition;15(3):178–196. doi:10.1038/nrm3758.
45. Spaderna S, Schmalhofer O, Wahlbuhl M, Dimmler A, Bauer K, Sultan A, et al. The Transcriptional Repressor ZEB1 Promotes Metastasis and Loss of Cell Polarity in Cancer;68(2):537–544. doi:10.1158/0008-5472.CAN-07-5682.
46. Aigner K, Dampier B, Descovich L, Mikula M, Sultan A, Schreiber M, et al. The transcription factor ZEB1 ( $\delta$ EF1) promotes tumour cell dedifferentiation by repressing master regulators of epithelial polarity;26(49):6979–6988. doi:10.1038/sj.onc.1210508.
47. Bellacosa A, Larue L. PI3K/AKT Pathway and the Epithelial-Mesenchymal Transition. In: Thomas-Tikhonenko A, editor. Cancer Genome and Tumor Microenvironment. Springer New York; p. 11–32. Available from: [http://link.springer.com/10.1007/978-1-4419-0711-0\\_2](http://link.springer.com/10.1007/978-1-4419-0711-0_2).
48. Zavadil J, Böttinger EP. TGF- $\beta$  and epithelial-to-mesenchymal transitions;24(37):5764–5774. doi:10.1038/sj.onc.1208927.
49. Xie L, Law BK, Chytil AM, Brown KA, Aakre ME, Moses HL. Activation of the Erk Pathway Is Required for TGF- $\beta$ 1-Induced EMT In Vitro;6(5):603–610.

## REFERENCES

50. Vincent T, Neve EPA, Johnson JR, Kukalev A, Rojo F, Albanell J, et al. A SNAIL1–SMAD3/4 transcriptional repressor complex promotes TGF- $\beta$  mediated epithelial–mesenchymal transition;11(8):943–950. doi:10.1038/ncb1905.
51. Igotz RA, Massagué J. Transforming growth factor-beta stimulates the expression of fibronectin and collagen and their incorporation into the extracellular matrix.;261(9):4337–4345.
52. Shang S, Hua F, Hu ZW. The regulation of  $\beta$ -catenin activity and function in cancer: therapeutic opportunities;8(20):33972–33989. doi:10.18632/oncotarget.15687.
53. Daniels DL, Weis WI. Beta-catenin directly displaces Groucho/TLE repressors from Tcf/Lef in Wnt-mediated transcription activation;12(4):364–371. doi:10.1038/nsmb912.
54. Stemmer V, de Craene B, Berx G, Behrens J. Snail promotes Wnt target gene expression and interacts with  $\beta$ -catenin;27(37):5075–5080. doi:10.1038/onc.2008.140.
55. Fodde R, Brabletz T. Wnt/beta-catenin signaling in cancer stemness and malignant behavior;19(2):150–158. doi:10.1016/j.ceb.2007.02.007.
56. Zhang S, Miao Y, Zheng X, Gong Y, Zhang J, Zou F, et al. STIM1 and STIM2 differently regulate endogenous Ca<sup>2+</sup> entry and promote TGF- $\beta$ -induced EMT in breast cancer cells;488(1):74–80. doi:10.1016/j.bbrc.2017.05.009.
57. Komiya Y, Habas R. Wnt signal transduction pathways;4(2):68–75.
58. Simi AK, Piotrowski AS, Nelson CM. Mechanotransduction, Metastasis and Genomic Instability. In: Genomic Instability and Cancer Metastasis. Cancer Metastasis - Biology and Treatment. Springer, Cham;. p. 139–158. Available from: [https://link.springer.com/chapter/10.1007/978-3-319-12136-9\\_7](https://link.springer.com/chapter/10.1007/978-3-319-12136-9_7).
59. Griggs LA, Hassan NT, Malik RS, Griffin BP, Martinez BA, Elmore LW, et al. Fibronectin fibrils regulate TGF- $\beta$ 1-induced Epithelial-Mesenchymal Transition;60-61:157–175. doi:10.1016/j.matbio.2017.01.001.
60. Park J, Schwarzbauer JE. Mammary epithelial cell interactions with fibronectin stimulate epithelial-mesenchymal transition;33(13):1649–1657. doi:10.1038/onc.2013.118.
61. Borghi N, Lowndes M, Maruthamuthu V, Gardel ML, Nelson WJ. Regulation of cell motile behavior by crosstalk between cadherin- and integrin-mediated adhesions;107(30):13324–13329. doi:10.1073/pnas.1002662107.

## REFERENCES

62. Martinez-Rico C, Pincet F, Thiery JP, Dufour S. Integrins stimulate E-cadherin-mediated intercellular adhesion by regulating Src-kinase activation and actomyosin contractility;123(5):712–722. doi:10.1242/jcs.047878.
63. Quadri SK. Cross talk between focal adhesion kinase and cadherins: Role in regulating endothelial barrier function;83(1):3–11. doi:10.1016/j.mvr.2011.08.001.
64. Zhang F, Tom CC, Kugler MC, Ching TT, Kreidberg JA, Wei Y, et al. Distinct ligand binding sites in integrin  $\alpha 3\beta 1$  regulate matrix adhesion and cell–cell contact;163(1):177–188. doi:10.1083/jcb.200304065.
65. Harrison OJ, Jin X, Hong S, Bahna F, Ahlsen G, Brasch J, et al. The extracellular architecture of adherens junctions revealed by crystal structures of type I cadherins;19(2):244–256. doi:10.1016/j.str.2010.11.016.
66. Kourtidis A, Ngok SP, Anastasiadis PZ. p120 Catenin. In: Progress in Molecular Biology and Translational Science. vol. 116. Elsevier;. p. 409–432. Available from: <http://linkinghub.elsevier.com/retrieve/pii/B9780123943118000182>.
67. Shapiro L, Weis WI. Structure and Biochemistry of Cadherins and Catenins;1(3):a003053. doi:10.1101/cshperspect.a003053.
68. Miyake Y, Inoue N, Nishimura K, Kinoshita N, Hosoya H, Yonemura S. Actomyosin tension is required for correct recruitment of adherens junction components and zonula occludens formation;312(9):1637–1650. doi:10.1016/j.yexcr.2006.01.031.
69. Kovacs EM, Ali RG, McCormack AJ, Yap AS. E-cadherin Homophilic Ligation Directly Signals through Rac and Phosphatidylinositol 3-Kinase to Regulate Adhesive Contacts;277(8):6708–6718. doi:10.1074/jbc.M109640200.
70. Gottardi CJ, Wong E, Gumbiner BM. E-Cadherin Suppresses Cellular Transformation by Inhibiting  $\beta$ -Catenin Signaling in an Adhesion-Independent Manner;153(5):1049–1060. doi:10.1083/jcb.153.5.1049.
71. Mui KL, Chen CS, Assoian RK. The mechanical regulation of integrin–cadherin crosstalk organizes cells, signaling and forces;129(6):1093–1100. doi:10.1242/jcs.183699.
72. Wheelock MJ, Shintani Y, Maeda M, Fukumoto Y, Johnson KR. Cadherin switching;121(6):727–735. doi:10.1242/jcs.000455.
73. Theveneau E, Mayor R. Cadherins in collective cell migration of mesenchymal cells;24(5):677–684. doi:10.1016/j.ceb.2012.08.002.

## REFERENCES

74. Derycke LDM, Bracke ME. N-cadherin in the spotlight of cell-cell adhesion, differentiation, embryogenesis, invasion and signalling;48(5):463–476. doi:10.1387/ijdb.041793ld.
75. Handorf AM, Zhou Y, Halanski MA, Li WJ. Tissue Stiffness Dictates Development, Homeostasis, and Disease Progression;11(1):1–15. doi:10.1080/15476278.2015.1019687.
76. Sun Z, Guo SS, Fässler R. Integrin-mediated mechanotransduction;215(4):445–456. doi:10.1083/jcb.201609037.
77. Jaalouk DE, Lammerding J. Mechanotransduction gone awry;10(1):63–73. doi:10.1038/nrm2597.
78. Wei SC, Yang J. Forcing through tumor metastasis: the interplay between tissue rigidity and epithelial-mesenchymal transition;26(2):111–120. doi:10.1016/j.tcb.2015.09.009.
79. Lampi MC, Reinhart-King CA. Targeting extracellular matrix stiffness to attenuate disease: From molecular mechanisms to clinical trials;10(422):eaao0475. doi:10.1126/scitranslmed.aao0475.
80. McKee KK, Harrison D, Capizzi S, Yurchenco PD. Role of laminin terminal globular domains in basement membrane assembly;282(29):21437–21447. doi:10.1074/jbc.M702963200.
81. Morrissey MA, Sherwood DR. An active role for basement membrane assembly and modification in tissue sculpting;128(9):1661–1668. doi:10.1242/jcs.168021.
82. Hohenester E, Yurchenco PD. Laminins in basement membrane assembly;7(1):56–63. doi:10.4161/cam.21831.
83. Li S, Edgar D, Fässler R, Wadsworth W, Yurchenco PD. The Role of Laminin in Embryonic Cell Polarization and Tissue Organization;4(5):613–624. doi:10.1016/S1534-5807(03)00128-X.
84. Ramirez NE, Zhang Z, Madamanchi A, Boyd KL, O’Rear LD, Nashabi A, et al. The  $\alpha_2\beta_1$  integrin is a metastasis suppressor in mouse models and human cancer;121(1):226–237. doi:10.1172/JCI42328.
85. Zutter MM, Santoro SA, Staatz WD, Tsung YL. Re-expression of the alpha 2 beta 1 integrin abrogates the malignant phenotype of breast carcinoma cells.;92(16):7411–7415.

## REFERENCES

86. Yurchenco PD, Patton BL. Developmental and Pathogenic Mechanisms of Basement Membrane Assembly;15(12):1277–1294.
87. Wang Z, Symons JM, Goldstein SL, McDonald A, Miner JH, Kreidberg JA. (Alpha)3(beta)1 integrin regulates epithelial cytoskeletal organization;112(17):2925–2935.
88. Borradori L, Sonnenberg A. Structure and Function of Hemidesmosomes: More Than Simple Adhesion Complexes;112(4):411–418. doi:10.1046/j.1523-1747.1999.00546.x.
89. Waterman EA, Sakai N, Nguyen NT, Horst BAJ, Veitch DP, Dey CN, et al. A laminin-collagen complex drives human epidermal carcinogenesis through phosphoinositol-3-kinase activation;67(9):4264–4270. doi:10.1158/0008-5472.CAN-06-4141.
90. Cagnet S, Faraldo MM, Kreft M, Sonnenberg A, Raymond K, Glukhova MA. Signaling events mediated by  $\alpha 3 \beta 1$  integrin are essential for mammary tumorigenesis;33(34):4286–4295. doi:10.1038/onc.2013.391.
91. Kim Y, Kugler MC, Wei Y, Kim KK, Li X, Brumwell AN, et al. Integrin  $\alpha 3 \beta 1$ -dependent  $\beta$ -catenin phosphorylation links epithelial Smad signaling to cell contacts;184(2):309–322. doi:10.1083/jcb.200806067.
92. Kim KK, Wei Y, Szekeres C, Kugler MC, Wolters PJ, Hill ML, et al. Epithelial cell  $\alpha 3 \beta 1$  integrin links  $\beta$ -catenin and Smad signaling to promote myofibroblast formation and pulmonary fibrosis;119(1):213–224. doi:10.1172/JCI36940.
93. Giannelli G, Bergamini C, Fransvea E, Sgarra C, Antonaci S. Laminin-5 With Transforming Growth Factor- $\beta 1$  Induces Epithelial to Mesenchymal Transition in Hepatocellular Carcinoma;129(5):1375–1383. doi:10.1053/j.gastro.2005.09.055.
94. Sugiura T, Berditchevski F. Function of  $\alpha 3 \beta 1$ -Tetraspanin Protein Complexes in Tumor Cell Invasion. Evidence for the Role of the Complexes in Production of Matrix Metalloproteinase 2 (Mmp-2);146(6):1375–1389.
95. Morini M, Mottolese M, Ferrari N, Ghiorzo F, Buglioni S, Mortarini R, et al. The  $\alpha 3 \beta 1$  integrin is associated with mammary carcinoma cell metastasis, invasion, and gelatinase B (mmp-9) activity;87(3):336–342. doi:10.1002/1097-0215(20000801)87:3<336::AID-IJC5>3.0.CO;2-3.
96. Li XL, Liu L, Li DD, He YP, Guo LH, Sun LP, et al. Integrin  $\beta 4$  promotes cell invasion and epithelial-mesenchymal transition through the modulation of Slug expression in hepatocellular carcinoma;7. doi:10.1038/srep40464.



## REFERENCES

97. Hynes RO. Fibronectins: multifunctional modular glycoproteins;95(2):369–377. doi:10.1083/jcb.95.2.369.
98. Mao Y, Schwarzbauer JE. Fibronectin fibrillogenesis, a cell-mediated matrix assembly process;24(6):389–399. doi:10.1016/j.matbio.2005.06.008.
99. Weinberg SH, Mair DB, Lemmon CA. Mechanotransduction Dynamics at the Cell-Matrix Interface;112(9):1962–1974. doi:10.1016/j.bpj.2017.02.027.
100. Singh P, Carraher C, Schwarzbauer JE. Assembly of Fibronectin Extracellular Matrix;26(1):397–419. doi:10.1146/annurev-cellbio-100109-104020.
101. Morgan MR, Byron A, Humphries MJ, Bass MD. GIVING OFF MIXED SIGNALS – DISTINCT FUNCTIONS OF  $\alpha 5\beta 1$  AND  $\alpha V\beta 3$  INTEGRINS IN REGULATING CELL BEHAVIOUR;61(7):731–738. doi:10.1002/iub.200.
102. Karsdal MA, Nielsen SH, Leeming DJ, Langholm LL, Nielsen MJ, Manon-Jensen T, et al. The good and the bad collagens of fibrosis – Their role in signaling and organ function;121:43–56. doi:10.1016/j.addr.2017.07.014.
103. Fang M, Yuan J, Peng C, Li Y. Collagen as a double-edged sword in tumor progression.;35(4):2871–82. doi:10.1007/s13277-013-1511-7.
104. Kaushik S, Pickup MW, Weaver VM. From transformation to metastasis: deconstructing the extracellular matrix in breast cancer;35(4):655–667. doi:10.1007/s10555-016-9650-0.
105. Wang JP, Hielscher A. Fibronectin: How Its Aberrant Expression in Tumors May Improve Therapeutic Targeting;8(4):674–682. doi:10.7150/jca.16901.
106. Shintani Y, Maeda M, Chaika N, Johnson KR, Wheelock MJ. Collagen I Promotes Epithelial-to-Mesenchymal Transition in Lung Cancer Cells via Transforming Growth Factor- $\beta$  Signaling;38(1):95–104. doi:10.1165/rcmb.2007-0071OC.
107. Gradl D, Kühl M, Wedlich D. The Wnt/Wg Signal Transducer  $\beta$ -Catenin Controls Fibronectin Expression;19(8):5576–5587. doi:10.1128/MCB.19.8.5576.
108. Kolosova I, Nethery D, Kern JA. Role of Smad2/3 and p38 MAP kinase in TGF- $\beta 1$ -induced epithelial-mesenchymal transition of pulmonary epithelial cells;226(5):1248–1254. doi:10.1002/jcp.22448.
109. Petrini I, Barachini S, Carnicelli V, Galimberti S, Modeo L, Boni R, et al. ED-B fibronectin expression is a marker of epithelial-mesenchymal transition in translational oncology;8(3):4914–4921. doi:10.18632/oncotarget.13615.

## REFERENCES

110. Onodera T, Sakai T, Hsu JCf, Matsumoto K, Chiorini JA, Yamada KM. Btbd7 Regulates Epithelial Cell Dynamics and Branching Morphogenesis;329(5991):562–565. doi:10.1126/science.1191880.
111. Imamichi Y, Menke A. Signaling Pathways Involved in Collagen-Induced Disruption of the E-Cadherin Complex during Epithelial-Mesenchymal Transition;185(1):180–190. doi:10.1159/000101319.
112. Cheng JC, Leung PCK. Type I collagen down-regulates E-cadherin expression by increasing PI3KCA in cancer cells;304(2):107–116. doi:10.1016/j.canlet.2011.02.008.
113. Menke A, Philippi C, Vogelmann R, Seidel B, Lutz MP, Adler G, et al. Down-regulation of E-cadherin gene expression by collagen type I and type III in pancreatic cancer cell lines;61(8):3508–3517.
114. Medici D, Nawshad A. Type I collagen promotes epithelial-mesenchymal transition through ILK-dependent activation of NF- $\kappa$ B and LEF-1;29(3):161–165. doi:10.1016/j.matbio.2009.12.003.
115. Shintani Y, Fukumoto Y, Chaika N, Svoboda R, Wheelock MJ, Johnson KR. Collagen I-mediated up-regulation of N-cadherin requires cooperative signals from integrins and discoidin domain receptor 1;180(6):1277–1289. doi:10.1083/jcb.200708137.
116. Rammal H, Saby C, Magnien K, Van-Gulick L, Garnotel R, Buache E, et al. Discoidin Domain Receptors: Potential Actors and Targets in Cancer;7. doi:10.3389/fphar.2016.00055.
117. Zhang K, Corsa CA, Ponik SM, Prior JL, Piwnica-Worms D, Eliceiri KW, et al. The collagen receptor discoidin domain receptor 2 stabilizes SNAIL1 to facilitate breast cancer metastasis;15(6):677–687. doi:10.1038/ncb2743.
118. Walsh LA, Nawshad A, Medici D. Discoidin domain receptor 2 is a critical regulator of epithelial-mesenchymal transition;30(4):243–247. doi:10.1016/j.matbio.2011.03.007.
119. Mak KM, Png CYM, Lee DJ. Type V Collagen in Health, Disease, and Fibrosis;299(5):613–629. doi:10.1002/ar.23330.
120. Lei GS, Kline HL, Lee CH, Wilkes DS, Zhang C. Regulation of Collagen V Expression and Epithelial-Mesenchymal Transition by miR-185 and miR-186 during Idiopathic Pulmonary Fibrosis;186(9):2310–2316. doi:10.1016/j.ajpath.2016.04.015.

## REFERENCES

121. Chekenya M, Krakstad C, Svendsen A, Netland IA, Staalesen V, Tysnes BB, et al. The progenitor cell marker NG2/MPG promotes chemoresistance by activation of integrin-dependent PI3K/Akt signaling;27(39):5182–5194. doi:10.1038/onc.2008.157.
122. Iyengar P, Espina V, Williams TW, Lin Y, Berry D, Jelicks LA, et al. Adipocyte-derived collagen VI affects early mammary tumor progression in vivo, demonstrating a critical interaction in the tumor/stroma microenvironment;115(5):1163–1176. doi:10.1172/JCI23424.
123. Vega ME, Schwarzbauer JE. Collaboration of fibronectin matrix with other extracellular signals in morphogenesis and differentiation;42:1–6. doi:10.1016/j.ceb.2016.03.014.
124. Zilberberg L, Todorovic V, Dabovic B, Horiguchi M, Couroussé T, Sakai LY, et al. Specificity of latent TGF- $\beta$  binding protein (LTBP) incorporation into matrix: Role of fibrillins and fibronectin;227(12):3828–3836. doi:10.1002/jcp.24094.
125. Robertson IB, Horiguchi M, Zilberberg L, Dabovic B, Hadjiolova K, Rifkin DB. Latent TGF- $\beta$ -binding proteins;47:44–53. doi:10.1016/j.matbio.2015.05.005.
126. Rifkin DB. Latent Transforming Growth Factor- $\beta$  (TGF- $\beta$ ) Binding Proteins: Orchestrators of TGF- $\beta$  Availability;280(9):7409–7412. doi:10.1074/jbc.R400029200.
127. Mamuya FA, Duncan MK.  $\alpha$ V integrins and TGF- $\beta$ -induced EMT: a circle of regulation;16(3):445–455. doi:10.1111/j.1582-4934.2011.01419.x.
128. Hynes RO. Extracellular matrix: not just pretty fibrils;326(5957):1216–1219. doi:10.1126/science.1176009.
129. Galliher AJ, Schiemann WP. Src phosphorylates Tyr284 in TGF-beta type II receptor and regulates TGF-beta stimulation of p38 MAPK during breast cancer cell proliferation and invasion;67(8):3752–3758. doi:10.1158/0008-5472.CAN-06-3851.
130. Brauer PR. MMPs—role in cardiovascular development and disease;11:447–478.
131. Page-McCaw A, Ewald AJ, Werb Z. Matrix metalloproteinases and the regulation of tissue remodelling;8(3):221–233. doi:10.1038/nrm2125.
132. Rodríguez D, Morrison CJ, Overall CM. Matrix metalloproteinases: What do they not do? New substrates and biological roles identified by murine models and proteomics;1803(1):39–54. doi:10.1016/j.bbamcr.2009.09.015.

## REFERENCES

133. Craig VJ, Zhang L, Hagood JS, Owen CA. Matrix metalloproteinases as therapeutic targets for idiopathic pulmonary fibrosis.;53(5):585–600. doi:10.1165/rcmb.2015-0020TR.
134. Giannandrea M, Parks WC. Diverse functions of matrix metalloproteinases during fibrosis;7(2):193–203. doi:10.1242/dmm.012062.
135. Pardo A, Cabrera S, Maldonado M, Selman M. Role of matrix metalloproteinases in the pathogenesis of idiopathic pulmonary fibrosis;17. doi:10.1186/s12931-016-0343-6.
136. Deryugina EI, Quigley JP. Tumor Angiogenesis: MMP-Mediated Induction of Intravasation- and Metastasis-Sustaining Neovasculature;44-46:94–112. doi:10.1016/j.matbio.2015.04.004.
137. Kessenbrock K, Plaks V, Werb Z. Matrix Metalloproteinases: Regulators of the Tumor Microenvironment;141(1):52–67. doi:10.1016/j.cell.2010.03.015.
138. Nabeshima K, Inoue T, Shimao Y, Sameshima T. Matrix metalloproteinases in tumor invasion: Role for cell migration;52(4):255–264. doi:10.1046/j.1440-1827.2002.01343.x.
139. Têtu B, Brisson J, Wang CS, Lapointe H, Beaudry G, Blanchette C, et al. The influence of MMP-14, TIMP-2 and MMP-2 expression on breast cancer prognosis;8(3):R28. doi:10.1186/bcr1503.
140. Sternlicht MD, Werb Z. How matrix metalloproteinases regulate cell behavior;17:463–516. doi:10.1146/annurev.cellbio.17.1.463.
141. Horejs CM. Basement membrane fragments in the context of the epithelial-to-mesenchymal transition;95(11):427–440. doi:10.1016/j.ejcb.2016.06.002.
142. Xu J, Rodriguez D, Petitclerc E, Kim JJ, Hangai M, Yuen SM, et al. Proteolytic exposure of a cryptic site within collagen type IV is required for angiogenesis and tumor growth in vivo;154(5):1069–1080. doi:10.1083/jcb.200103111.
143. Horejs CM, Serio A, Purvis A, Gormley AJ, Bertazzo S, Poliniewicz A, et al. Biologically-active laminin-111 fragment that modulates the epithelial-to-mesenchymal transition in embryonic stem cells;111(16):5908–5913. doi:10.1073/pnas.1403139111.
144. Xiao Q, Jiang Y, Liu Q, Yue J, Liu C, Zhao X, et al. Minor Type IV Collagen  $\alpha$ 5 Chain Promotes Cancer Progression through Discoidin Domain Receptor-1;11(5):e1005249. doi:10.1371/journal.pgen.1005249.

## REFERENCES

145. Buonato JM, Lazzara MJ. ERK1/2 Blockade Prevents Epithelial–Mesenchymal Transition in Lung Cancer Cells and Promotes Their Sensitivity to EGFR Inhibition;74(1):309–319. doi:10.1158/0008-5472.CAN-12-4721.
146. Mori H, Lo AT, Inman JL, Alcaraz J, Ghajar CM, Mott JD, et al. Transmembrane/cytoplasmic, rather than catalytic, domains of Mmp14 signal to MAPK activation and mammary branching morphogenesis via binding to integrin  $\beta$ 1;140(2):343–352. doi:10.1242/dev.084236.
147. Chaturvedi S, Hass R. Extracellular signals in young and aging breast epithelial cells and possible connections to age-associated breast cancer development;132(5):213–219. doi:10.1016/j.mad.2011.04.002.
148. Illman SA, Lehti K, Keski-Oja J, Lohi J. Epilysin (MMP-28) induces TGF- $\beta$  mediated epithelial to mesenchymal transition in lung carcinoma cells;119(18):3856–3865. doi:10.1242/jcs.03157.
149. Yu Q, Stamenkovic I. Cell surface-localized matrix metalloproteinase-9 proteolytically activates TGF-beta and promotes tumor invasion and angiogenesis;14(2):163–176.
150. Maeda S, Dean DD, Gomez R, Schwartz Z, Boyan BD. The First Stage of Transforming Growth Factor  $\beta$ 1 Activation is Release of the Large Latent Complex from the Extracellular Matrix of Growth Plate Chondrocytes by Matrix Vesicle Stromelysin-1 (MMP-3);70(1):54–65. doi:10.1007/s002230010032.
151. Mu D, Cambier S, Fjellbirkeland L, Baron JL, Munger JS, Kawakatsu H, et al. The integrin  $\alpha$ v $\beta$ 8 mediates epithelial homeostasis through MT1-MMP-dependent activation of TGF- $\beta$ 1;157(3):493–507. doi:10.1083/jcb.200109100.
152. Krstic J, Santibanez JF. type [;]Available from: <https://www.hindawi.com/journals/tswj/2014/521754/>.
153. Rozanov DV, Deryugina EI, Monosov EZ, Marchenko ND, Strongin AY. Aberrant, persistent inclusion into lipid rafts limits the tumorigenic function of membrane type-1 matrix metalloproteinase in malignant cells;293(1):81–95. doi:10.1016/j.yexcr.2003.10.006.
154. Yamashita CM, Dolgonos L, Zemans RL, Young SK, Robertson J, Briones N, et al. Matrix metalloproteinase 3 is a mediator of pulmonary fibrosis;179(4):1733–1745. doi:10.1016/j.ajpath.2011.06.041.
155. McGuire JK, Li Q, Parks WC. Matrilysin (Matrix Metalloproteinase-7) Mediates E-Cadherin Ectodomain Shedding in Injured Lung Epithelium;162(6):1831–1843.

## REFERENCES

156. Repetto O, De Paoli P, De Re V, Canzonieri V, Cannizzaro R. type [;]Available from: <https://www.hindawi.com/journals/bmri/2014/408047/>.
157. Noe V, Fingleton B, Jacobs K, Crawford HC, Vermeulen S, Steelant W, et al. Release of an invasion promoter E-cadherin fragment by matrilysin and stromelysin-1;114(1):111–118.
158. David JM, Rajasekaran AK. Dishonorable Discharge: The Oncogenic Roles of Cleaved E-cadherin Fragments;72(12):2917–2923. doi:10.1158/0008-5472.CAN-11-3498.
159. Radisky DC, Levy DD, Littlepage LE, Liu H, Nelson CM, Fata JE, et al. Rac1b and reactive oxygen species mediate MMP-3-induced EMT and genomic instability;436(7047):123–127. doi:10.1038/nature03688.
160. Le Bras GF, Taubenslag KJ, Andl CD. The regulation of cell-cell adhesion during epithelial-mesenchymal transition, motility and tumor progression;6(4):365–373. doi:10.4161/cam.21326.
161. Tseng Q, Duchemin-Pelletier E, Deshiere A, Balland M, Guillou H, Filhol O, et al. Spatial organization of the extracellular matrix regulates cell–cell junction positioning;109(5):1506–1511. doi:10.1073/pnas.1106377109.
162. Gomez EW, Chen QK, Gjorevski N, Nelson CM. Tissue geometry patterns epithelial-mesenchymal transition via intercellular mechanotransduction;110(1):44–51. doi:10.1002/jcb.22545.
163. Eisenberg JL, Safi A, Wei X, Espinosa HD, Budinger GS, Takawira D, et al.. Substrate stiffness regulates extracellular matrix deposition by alveolar epithelial cells;. Available from: <https://www.dovepress.com/substrate-stiffness-regulates-extracellular-matrix-deposition-by-alveo-peer-revie>
164. Scott LE, Mair DB, Narang JD, Feleke K, Lemmon CA. Fibronectin fibrillogenesis facilitates mechano-dependent cell spreading, force generation, and nuclear size in human embryonic fibroblasts;7(11):1454–1465. doi:10.1039/C5IB00217F.
165. Kubow KE, Vukmirovic R, Zhe L, Klotzsch E, Smith ML, Gourdon D, et al. Mechanical forces regulate the interactions of fibronectin and collagen I in extracellular matrix;6:8026. doi:10.1038/ncomms9026.
166. Markowski MC, Brown AC, Barker TH. Directing epithelial to mesenchymal transition through engineered microenvironments displaying orthogonal adhesive and mechanical cues;100A(8):2119–2127. doi:10.1002/jbm.a.34068.

## REFERENCES

167. Sethi A, Mao W, Wordinger RJ, Clark AF. Transforming Growth Factor- $\beta$  Induces Extracellular Matrix Protein Cross-Linking Lysyl Oxidase (LOX) Genes in Human Trabecular Meshwork Cells;52(8):5240–5250. doi:10.1167/iovs.11-7287.
168. Voloshenyuk TG, Landesman ES, Khoutorova E, Hart AD, Gardner JD. Induction of cardiac fibroblast lysyl oxidase by TGF- $\beta$ 1 requires PI3K/Akt, Smad3, and MAPK signaling;55(1):90–97. doi:10.1016/j.cyto.2011.03.024.
169. SUN B, FANG Y, LI Z, CHEN Z, XIANG J. Role of cellular cytoskeleton in epithelial-mesenchymal transition process during cancer progression;3(5):603–610. doi:10.3892/br.2015.494.
170. Collins C, Denisin AK, Pruitt BL, Nelson WJ. Changes in E-cadherin rigidity sensing regulate cell adhesion;114(29):E5835–E5844. doi:10.1073/pnas.1618676114.
171. Yonemura S, Wada Y, Watanabe T, Nagafuchi A, Shibata M. alpha-Catenin as a tension transducer that induces adherens junction development;12(6):533–542. doi:10.1038/ncb2055.
172. Graner F, Glazier JA. Simulation of biological cell sorting using a two-dimensional extended Potts model;69(13):2013–2016. doi:10.1103/PhysRevLett.69.2013.
173. Glazier JA, Balter A, Popławski NJ. Magnetization to Morphogenesis: A Brief History of the Glazier-Graner-Hogeweg Model. In: Single-Cell-Based Models in Biology and Medicine. Mathematics and Biosciences in Interaction. Birkhäuser Basel;. p. 79–106. Available from: [https://link.springer.com/chapter/10.1007/978-3-7643-8123-3\\_4](https://link.springer.com/chapter/10.1007/978-3-7643-8123-3_4).
174. Oers RFMv, Rens EG, LaValley DJ, Reinhart-King CA, Merks RMH. Mechanical Cell-Matrix Feedback Explains Pairwise and Collective Endothelial Cell Behavior In Vitro;10(8):e1003774. doi:10.1371/journal.pcbi.1003774.
175. Vargas DA, Bates O, Zaman MH. Computational Model to Probe Cellular Mechanics during Epithelial-Mesenchymal Transition;197(6):435–444. doi:10.1159/000348415.
176. Neagu A, Mironov V, Kosztin I, Barz B, Neagu M, Moreno-Rodriguez RA, et al. Computational modeling of epithelial–mesenchymal transformations;100(1):23–30. doi:10.1016/j.biosystems.2009.12.004.
177. Daub JT, Merks RMH. A Cell-Based Model of Extracellular-Matrix-Guided Endothelial Cell Migration During Angiogenesis;75(8):1377–1399. doi:10.1007/s11538-013-9826-5.

## REFERENCES

178. Peinado H, Quintanilla M, Cano A. Transforming Growth Factor  $\beta$ -1 Induces Snail Transcription Factor in Epithelial Cell Lines MECHANISMS FOR EPITHELIAL MESENCHYMAL TRANSITIONS;278(23):21113–21123. doi:10.1074/jbc.M211304200.
179. Siemens H, Jackstadt R, Hüntten S, Kaller M, Menssen A, Götz U, et al. miR-34 and SNAIL form a double-negative feedback loop to regulate epithelial-mesenchymal transitions;10(24):4256–4271. doi:10.4161/cc.10.24.18552.
180. Kim NH, Kim HS, Li XY, Lee I, Choi HS, Kang SE, et al. A p53/miRNA-34 axis regulates Snail1-dependent cancer cell epithelial–mesenchymal transition;195(3):417–433. doi:10.1083/jcb.201103097.
181. Tian XJ, Zhang H, Xing J. Coupled Reversible and Irreversible Bistable Switches Underlying TGF $\beta$ -induced Epithelial to Mesenchymal Transition;105(4):1079–1089. doi:10.1016/j.bpj.2013.07.011.
182. Steinway SN, Zañudo JGT, Michel PJ, Feith DJ, Loughran TP, Albert R. Combinatorial interventions inhibit TGF $\beta$ -driven epithelial-to-mesenchymal transition and support hybrid cellular phenotypes;1:15014. doi:10.1038/npjbsa.2015.14.
183. Caramel J, Papadogeorgakis E, Hill L, Browne G, Richard G, Wierinckx A, et al. A Switch in the Expression of Embryonic EMT-Inducers Drives the Development of Malignant Melanoma;24(4):466–480. doi:10.1016/j.ccr.2013.08.018.
184. Nieto MA. Epithelial Plasticity: A Common Theme in Embryonic and Cancer Cells;342(6159):1234850–1234850. doi:10.1126/science.1234850.
185. Ramis-Conde I, Drasdo D, Anderson ARA, Chaplain MAJ. Modeling the Influence of the E-Cadherin- $\beta$ -Catenin Pathway in Cancer Cell Invasion: A Multiscale Approach;95(1):155–165. doi:10.1529/biophysj.107.114678.
186. Lemmon CA, Romer LH. A Predictive Model of Cell Traction Forces Based on Cell Geometry;99(9):L78–L80. doi:10.1016/j.bpj.2010.09.024.
187. Mertz AF, Banerjee S, Che Y, German GK, Xu Y, Hyland C, et al. Scaling of Traction Forces with the Size of Cohesive Cell Colonies;108(19). doi:10.1103/PhysRevLett.108.198101.
188. Bazellières E, Conte V, Elosegui-Artola A, Serra-Picamal X, Bintanel-Morcillo M, Roca-Cusachs P, et al. Control of cell–cell forces and collective cell dynamics by the intercellular adhesome;17(4):409–420. doi:10.1038/ncb3135.



## REFERENCES

189. Ng MR, Besser A, Brugge JS, Danuser G. Mapping the dynamics of force transduction at cell–cell junctions of epithelial clusters;5(3). doi:10.7554/eLife.03282.
190. Arsenovic P, Ramachandran I, Bathula K, Zhu R, Narang J, Noll N, et al. Nesprin-2G, a Component of the Nuclear LINC Complex, Is Subject to Myosin-Dependent Tension;110(1):34–43. doi:10.1016/j.bpj.2015.11.014.
191. Liu Z, Tan JL, Cohen DM, Yang MT, Sniadecki NJ, Ruiz SA, et al. Mechanical tugging force regulates the size of cell–cell junctions;107(22):9944–9949. doi:10.1073/pnas.0914547107.
192. Puliafito A, Hufnagel L, Neveu P, Streichan S, Sigal A, Fygenson DK, et al. Collective and single cell behavior in epithelial contact inhibition;109(3):739–744. doi:10.1073/pnas.1007809109.
193. Mendonsa A, Na TY, Gumbiner BM. E-cadherin in Contact Inhibition and Cancer;37(35):4769–4780. doi:10.1038/s41388-018-0304-2.
194. Scarpa E, Szabó A, Bibonne A, Theveneau E, Parsons M, Mayor R. Cadherin Switch during EMT in Neural Crest Cells Leads to Contact Inhibition of Locomotion via Repolarization of Forces;34(4):421–434. doi:10.1016/j.devcel.2015.06.012.
195. Carmona-Fontaine C, Matthews HK, Kuriyama S, Moreno M, Dunn GA, Parsons M, et al. Contact Inhibition of Locomotion in vivo controls neural crest directional migration;456(7224):957–961. doi:10.1038/nature07441.
196. Mohan A, Schlue KT, Kniffin AF, Mayer CR, Duke AA, Narayanan V, et al. Spatial Proliferation of Epithelial Cells Is Regulated by E-Cadherin Force;115(5):853–864. doi:10.1016/j.bpj.2018.07.030.
197. Arsenovic PT, Mayer CR, Conway DE. SensorFRET: A Standardless Approach to Measuring Pixel-based Spectral Bleed-through and FRET Efficiency using Spectral Imaging;7(1):15609. doi:10.1038/s41598-017-15411-8.
198. Borghi N, Sorokina M, Shcherbakova OG, Weis WI, Pruitt BL, Nelson WJ, et al. E-cadherin is under constitutive actomyosin-generated tension that is increased at cell–cell contacts upon externally applied stretch;109(31):12568–12573. doi:10.1073/pnas.1204390109.
199. Gumbiner BM. Regulation of cadherin-mediated adhesion in morphogenesis;6(8):622–634. doi:10.1038/nrm1699.
200. Tian X, Liu Z, Niu B, Zhang J, Tan TK, Lee SR, et al. E-Cadherin/ $\beta$ -Catenin Complex and the Epithelial Barrier;2011. doi:10.1155/2011/567305.

## REFERENCES

201. Lemmon CA, Sniadecki NJ, Ruiz SA, Tan JL, Romer LH, Chen CS. Shear Force at the Cell-Matrix Interface: Enhanced Analysis for Microfabricated Post Array Detectors;2(1):1–16.
202. Yilmaz M, Christofori G. EMT, the cytoskeleton, and cancer cell invasion;28(1):15–33. doi:10.1007/s10555-008-9169-0.
203. MacDonald BT, Tamai K, He X. Wnt/ $\beta$ -catenin signaling: components, mechanisms, and diseases;17(1):9. doi:10.1016/j.devcel.2009.06.016.
204. Schaller G, Meyer-Hermann M. Multicellular tumor spheroid in an off-lattice Voronoi-Delaunay cell model;71(5). doi:10.1103/PhysRevE.71.051910.
205. Gattinoni L, Ji Y, Restifo NP. Wnt/ $\beta$ -Catenin Signaling in T-Cell Immunity and Cancer Immunotherapy;16(19):4695–4701. doi:10.1158/1078-0432.CCR-10-0356.
206. Yook JI, Li XY, Ota I, Fearon ER, Weiss SJ. Wnt-dependent Regulation of the E-cadherin Repressor Snail;280(12):11740–11748. doi:10.1074/jbc.M413878200.
207. Thiery JP, Sleeman JP. Complex networks orchestrate epithelial–mesenchymal transitions;7(2):131–142. doi:10.1038/nrm1835.
208. Schaumann EN, Staddon MF, Gardel ML, Banerjee S. Force localization modes in dynamic epithelial colonies;29(23):2835–2847. doi:10.1091/mbc.E18-05-0336.
209. Park JA, Atia L, Mitchel JA, Fredberg JJ, Butler JP. Collective migration and cell jamming in asthma, cancer and development;129(18):3375–3383. doi:10.1242/jcs.187922.



REFERENCES

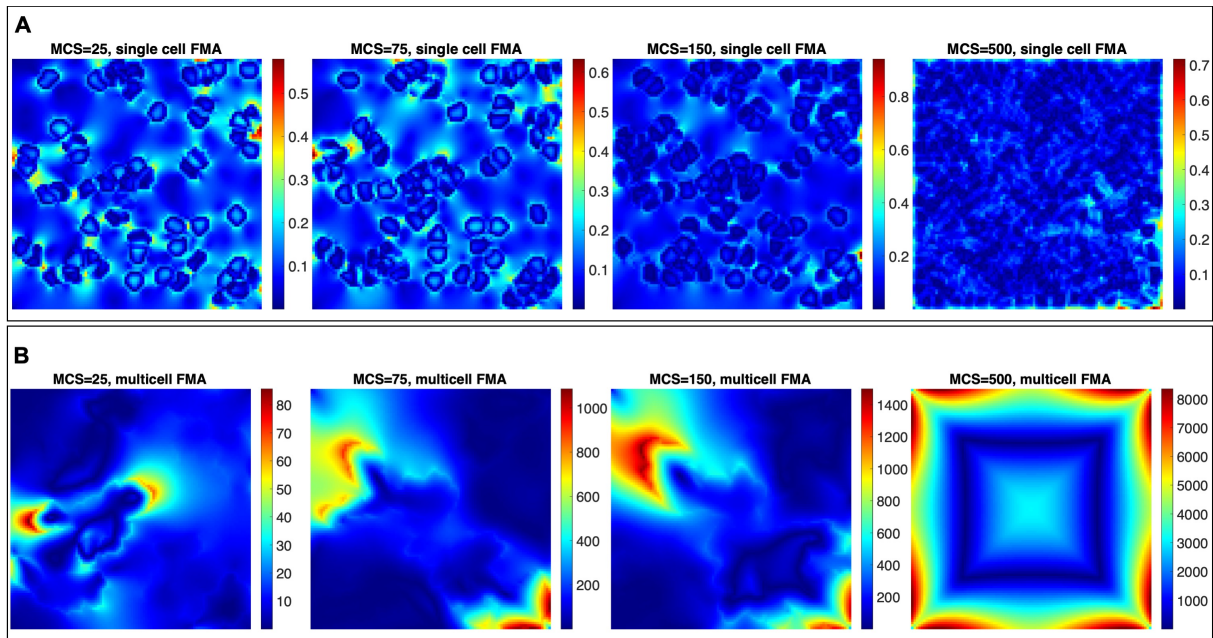
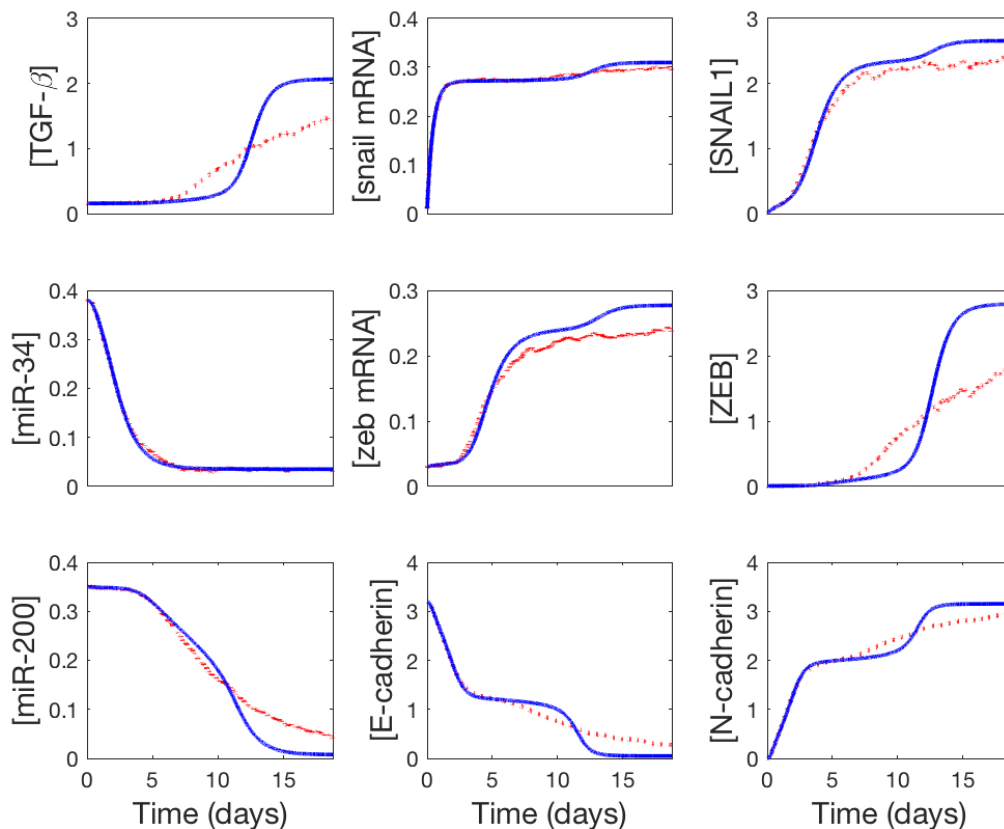


Figure S2. Substrate strains of the single and multicellular FMA.

REFERENCES



**Figure S3.** EMT-associated gene regulatory network with stochastic dynamics evaluated at 3 nM exogenous TGF- $\beta$  stimulation for 18.75 simulation days. The deterministic solution (solid blue line) indicates an intermediate steady state. The stochastic solution (red dashed line) shows a loss of the intermediate state as the result of noise of the low molecule number for mRNA and miRNA-200.

## Supporting Tables

| Parameter                  | Symbol           | Value                  |
|----------------------------|------------------|------------------------|
| Element size               | $\Delta x$       | 2.5 $\mu\text{m}$      |
| Intrinsic cell motility    | $T$              | 1                      |
| Target cell area           | $A_0$            | 314.16 $\mu\text{m}^2$ |
| Proliferation area minimum | $A_{divide}$     | 209.44 $\mu\text{m}^2$ |
| Proliferation probability  | $P_{divide}$     | 0.005                  |
| Elasticity parameter       | $\lambda_{area}$ | 500                    |
| Cell-matrix contact cost   | $J_{cm}$         | 2.5* pixels/side       |
| Cell-cell contact cost     | $J_{cc}$         | 5.0* pixels/side       |
| Young's modulus            | $E$              | 10 kPa                 |
| Poisson's ratio            | $\nu$            | 0.45                   |
| Traction force constant    | $\mu$            | 0.01 nN/ $\mu\text{m}$ |

**Table S1:.** Cellular Potts model and Finite element model parameters. \* Value used unless otherwise noted.

| Parameter  | Symbol | Value                        |
|--|--------|------------------------------|
| Exogenous TGF- $\beta$                                   | $T_0$  | 3.0 nM                       |
| Basal TGF- $\beta$ production rate                       | $k0_T$ | 0.06 $\mu\text{M hr}^{-1}$   |
| TGF- $\beta$ production rate                             | $k_T$  | 1.2 $\mu\text{M hr}^{-1}$    |
| miR200-dependent inhibition of TGF- $\beta$ expression   | $J_T$  | 0.06 $\mu\text{M}$           |
| TGF- $\beta$ degradation rate                            | $kd_T$ | 0.6 $\text{hr}^{-1}$         |
| Basal <i>snail1</i> transcription rate                   | $k0_s$ | 0.0006 $\mu\text{M hr}^{-1}$ |
| <i>snail1</i> transcription rate                         | $k_s$  | 0.003 $\mu\text{M hr}^{-1}$  |
| TGF- $\beta$ -dependent <i>snail1</i> translation rate   | $J_s$  | 1.6 $\mu\text{M}$            |
| <i>snail1</i> mRNA degradation rate                      | $kd_s$ | 0.09 $\text{hr}^{-1}$        |
| <i>snail1</i> mRNA translation rate                      | $k_S$  | 16 $\mu\text{M hr}^{-1}$     |
| miR-34-dependent inhibition of <i>snail1</i> translation | $J_S$  | 0.08 $\mu\text{M}$           |
| Degradation rate of SNAIL1                               | $kd_S$ | 1.66 $\text{hr}^{-1}$        |
| Basal <i>miR</i> – 34 production rate                    | $k0_3$ | 0.0012 $\mu\text{M hr}^{-1}$ |
| miR-34 production rate                                   | $k_3$  | 0.012 $\mu\text{M hr}^{-1}$  |
| SNAIL1-dependent inhibition of miR-34 production         | $J1_3$ | 0.15 $\mu\text{M}$           |
| ZEB-dependent inhibition of miR-34 production            | $J2_3$ | 0.36 $\mu\text{M}$           |
| miR-34 degradation rate                                  | $kd_3$ | 0.035 $\text{hr}^{-1}$       |
| Basal <i>zeb</i> transcription rate                      | $k0_Z$ | $\mu\text{M hr}^{-1}$        |
| <i>zeb</i> transcription rate                            | $k_z$  | $\mu\text{M hr}^{-1}$        |

*Continued on the next page*

6. APPENDIX

Table S2 – *continued from previous page*

|  |           |                              |
|--|-----------|------------------------------|
| SNAIL1-dependent <i>zeb</i> transcription                  | $J_z$     | $\mu\text{M}$                |
| <i>zeb</i> mRNA degradation rate                           | $kd_z$    | $\text{hr}^{-1}$             |
| <i>zeb</i> translation rate                                | $k_Z$     | $17 \mu\text{M hr}^{-1}$     |
| miR-34-dependent inhibition of <i>zeb</i> mRNA translation | $J_Z$     | $0.06 \mu\text{M hr}^{-1}$   |
| ZEB degradation rate                                       | $kd_Z$    | $1.66 \text{hr}^{-1}$        |
| Basal miR-200 production rate                              | $k_{0_2}$ | $0.0002 \mu\text{M hr}^{-1}$ |
| miR-200 production rate                                    | $k_2$     | $0.012 \mu\text{M hr}^{-1}$  |
| SNAIL1-dependent inhibition of miR-200 production          | $J_{1_2}$ | $5 \mu\text{M}$              |
| ZEB-dependent inhibition of miR-200 production             | $J_{2_2}$ | $0.2 \mu\text{M}$            |
| miR-200 degradation rate                                   | $kd_2$    | $0.035 \text{hr}^{-1}$       |
| E-cadherin production rate 1                               | $k_{e1}$  | $1 \mu\text{M hr}^{-1}$      |
| E-cadherin production rate 2                               | $k_{e2}$  | $0.6 \mu\text{M hr}^{-1}$    |
| SNAIL1-dependent inhibition of E-cadherin production       | $J_{e1}$  | $0.2 \mu\text{M}$            |
| ZEB-dependent inhibition of E-cadherin production          | $J_{e2}$  | $0.5 \mu\text{M}$            |
| E-cadherin degradation rate                                | $kd_e$    | $0.5 \text{hr}^{-1}$         |
| N-cadherin production rate 1                               | $k_{n1}$  | $1 \mu\text{M hr}^{-1}$      |
| N-cadherin production rate 2                               | $k_{n2}$  | $0.6 \mu\text{M hr}^{-1}$    |
| SNAIL1-dependent inhibition of N-cadherin production       | $J_{n1}$  | $0.2 \mu\text{M}$            |
| ZEB-dependent inhibition of N-cadherin production          | $J_{n2}$  | $0.5 \mu\text{M}$            |
| N-cadherin degradation rate                                | $kd_n$    | $0.5 \text{hr}^{-1}$         |
| TGF- $\beta$ -dependent SNAIL1 expression                  | $n_{nt}$  | 2                            |
| SNAIL1-dependent activation or inhibition                  | $n_{ns}$  | 2                            |
| ZEB-dependent inhibition                                   | $n_{nz}$  | 2                            |
| miR-200-dependent inhibition                               | $n_{nr2}$ | 2                            |
| miR-34-dependent inhibition                                | $n_{nr3}$ | 2                            |

**Table S2:.** EMT-associated gene regulatory network parameters and rates.